2014

MODELING OF TRANSFER PATH FOR DETERMINATION OF COMBUSTION AND NOISE METRICS ON DIESEL ENGINES

Libin Jia

Michigan Technological University

MODELING OF TRANSFER PATH FOR DETERMINATION OF COMBUSTION AND NOISE METRICS ON DIESEL ENGINES

By

Libin Jia

A DISSERTATION

Submitted in partial fulfillment of the requirements for the degree of

DOCTOR OF PHILOSOPHY

In Mechanical Engineering – Engineering Mechanics

MICHIGAN TECHNOLOGICAL UNIVERSITY

2014

This dissertation has been approved in partial fulfillment of the requirements for the Degree of DOCTOR OF PHILOSOPHY in Mechanical Engineering – Engineering Mechanics

Department of Mechanical Engineering – Engineering Mechanics

Dissertation Co-Advisor: *Dr. Jeffrey D. Naber*

Dissertation Co-Advisor: *Dr. Jason R. Blough*

Committee Member: *Dr. Charles D. Van Karsen*

Committee Member: *Dr. Seyed A. (Reza) Zekavat*

Department Chair: *Dr. William Predebon*

Table of Contents

List of Figures

List of Tables

Acknowledgements

I would like to express my gratitude to my advisors Dr. Naber and Dr. Blough for providing me this research opportunity to gain a wealth of knowledge and touch the goal of PhD degree. Dr. Naber, I really appreciate your consistent financial supports and the sufficient freedom you gave me to explore what I am interested in. Your expertise, passion, and diligence to your work made you a model to me for how to achieve the goal of my future career. The research experience under your guidance will be one of the most unforgettable memories of my life. Dr. Blough, I really appreciate the guidance and supports you gave to me. Your talents and humor helped me find the solution of a problem with much pleasure. Each meeting time with you is relaxed and enjoyable. I will miss it. Also, I would like to thank my committee members Dr. Seyed A. Zekavat and Dr. Charles Van Karsen, your feedbacks and supports to my research helped to make it a success. I will not complete my degree without your help.

I would like to thank MEEM department of Michigan Technological University to provide me the teaching assistance opportunities. I would also like to thank John Deere and Nostrum Energy LLC for the financial support and data acquisition support you provided.

I am also grateful to the friends I have in Michigan Tech. I thank the fellows who work in the MEEMsb013, officemates, and other colleagues for your supports. Your help made my research possible.

I thank god to have a group of friends in Houghton to build up the firm brotherhood. I cannot imagine how the life will be like without you. You are the treasure of my life.

I am extremely grateful to my family, my parents and my wife, for your consistent supports and belief in my completion of the PhD study. I love you!

Preface

Chapter 5 was published in “Journal of Engineering for Gas Turbines and Power” [i]. In this paper, Libin analyzed the data and wrote the paper. Dr. Naber and Dr. Blough reviewed and revised it. Dr. Reza gave some recommendations for data processing. Chapter 4 was submitted to “Proceedings of the Institution of Mechanical Engineers, Part C: Journal of Mechanical Engineering Science” and the current status is “Peer review in process”. Chapter 6 was submitted to “SAE International Journal of Engines” and the current status is “Peer review in process”. Chapter 2 will be published as journal article co-authored by my advisors Dr. Naber and Dr. Blough. In these papers, Libin analyzed the data and wrote the paper, Dr. Naber and Dr. Blough reviewed and revised them.

Nomenclature

AHR = apparent heat release rate

BSFC = brake specific fuel consumption

CA50 = crank angle location where 50% of cumulative heat released during one cycle

CAD = crank angle degree

DATDC = degree after top dead center

DBTCD = degree before top dead center

ECU = engine control unit

FFT = fast Fourier transform

FRF = frequency response function

IMEP = indicated mean effective pressure

MAPE = mean absolute pressure error

MGS = modified Gram-Schmidt method

MISO = multiple-input and single-output

MIMO = multiple-input and multiple-output

PAA = peak apparent heat release rate amplitude

PACL = peak apparent heat release rate crank angle location

PCA = principal component analysis method

PPCLE = peak pressure crank angle location error

PPAE = peak pressure amplitude error

PPCL = peak pressure crank angle location

PPA = peak pressure amplitude

PSO = particle swarm optimization

RBFNN = radial basis function neural network

ROM = read-only memory

SISO = single-input and single-output

SNR = signal noise ratio

SOI = start of ignition

SOC = start of combustion

SPA = sample-based pressure amplitude

TDI = turbocharged direct injection

Abstract[1]

Determination of combustion metrics for a diesel engine has the potential of providing feedback for closed-loop combustion phasing control to meet current and upcoming emission and fuel consumption regulations. This thesis focused on the estimation of combustion metrics including start of combustion (SOC), crank angle location of 50% cumulative heat release (CA50), peak pressure crank angle location (PPCL), and peak pressure amplitude (PPA), peak apparent heat release rate crank angle location (PACL), mean absolute pressure error (MAPE), and peak apparent heat release rate amplitude (PAA). In-cylinder pressure has been used in the laboratory as the primary mechanism for characterization of combustion rates and more recently in-cylinder pressure has been used in series production vehicles for feedback control. However, the intrusive measurement with the in-cylinder pressure sensor is expensive and requires special mounting process and engine structure modification. As an alternative method, this work investigated block mounted accelerometers to estimate combustion metrics in a 9L I6 diesel engine. So the transfer path between the accelerometer signal and the in-cylinder pressure signal needs to be modeled. Depending on the transfer path, the in-cylinder pressure signal and the combustion metrics can be accurately estimated - recovered from accelerometer signals. The method and applicability for determining the transfer path is critical in utilizing an accelerometer(s) for feedback.

Single-input single-output (SISO) frequency response function (FRF) is the most common transfer path model; however, it is shown here to have low robustness for varying engine operating conditions. This thesis examines mechanisms to improve the robustness of FRF for combustion metrics estimation. First, an adaptation process based on the particle swarm optimization algorithm was developed and added to the single-input single-output model. Second, a multiple-input single-output (MISO) FRF model

[1] The material contained in this section is planned for submission as part of a journal article and/or conference paper in the future.

coupled with principal component analysis and an offset compensation process was investigated and applied. Improvement of the FRF robustness was achieved based on these two approaches. Furthermore a neural network as a nonlinear model of the transfer path between the accelerometer signal and the apparent heat release rate was also investigated.

Transfer path between the acoustical emissions and the in-cylinder pressure signal was also investigated in this dissertation on a high pressure common rail (HPCR) 1.9L TDI diesel engine. The acoustical emissions are an important factor in the powertrain development process. In this part of the research a transfer path was developed between the two and then used to predict the engine noise level with the measured in-cylinder pressure as the input. Three methods for transfer path modeling were applied and the method based on the cepstral smoothing technique led to the most accurate results with averaged estimation errors of 2 dBA and a root mean square error of 1.5dBA. Finally, a linear model for engine noise level estimation was proposed with the in-cylinder pressure signal and the engine speed as components.

Chapter 1

Introduction[1]

1.1 Background

Diesel engines have a wide spread use in automobiles, medium and heavy duty trucks, locomotives, construction equipment, and power generation due to its unique combination of fuel economy, reliability, durability, and affordability [2]. A Diesel engine ignites the fuel through increasing the working gas temperature as a result of combustion. Fuel is injected to the combustion chamber late in the cycle near the top dead center. The combustion of the fuel transforms the fuel's chemical energy to sensible (thermal) energy in the working gas and generates high cylinder pressure which develops torque through the crank-slider mechanism by applying a force on the pistons to move and transmit the energy to the crankshaft. Diesel engines have the advantage of high fuel economy. In comparison to the spark ignition engines, diesel engines are 30-35% more fuel efficient than similar-size gasoline engines [3].

Diesel engine introduces significant carbon dioxide benefits, but regulations remain concerned with the nitrogen oxide (NOx) and particulate (PM) production [4]. In the 1970s, the U.S. Environmental Protection Agency (EPA) and other organizations initiated regulations with respect to the diesel emissions [5]. In both North America and

[1]The material contained in this section is planned for submission as part of a journal article and/or conference paper in the future.

Europe, the major challenges are in PM and NOx control for the legislation to be introduced in 2005 (EuroIV), 2007 (US ’07), 2008 (Euro V), and 2010 (US ’10) [6].
The future wide spread usage of diesel engine for power supply can only be realized if their exhaust emissions meet the increasingly stringent emissions legislation.

For a further reduction of engine-out emissions, closed-loop control of the combustion process has been a focus for engine research and development [7, 8, & 9]. Open-loop operation based on calibration maps which are conservatively set based upon laboratory operation can give a quick response and is relatively easy to control. However, the open loop cannot adapt to the changes caused by the condition variations such as injector aging and fuel quality [8]. In comparison, closed-loop control considers the condition changes in the control mechanism and enables operation closer to the optimum fuel consumption and emissions target. Combustion metrics detected or estimated through a sensor provides feedback information to control the combustion process. In-cylinder pressure waveform is the most commonly used signal which provides the information for engine combustion control [10-12]. Many other combustion metrics, CA50, SOC, and PPCL, which characterize the phase of combustion process, can be obtained based on the derivations of the in-cylinder pressure signal. These combustion metrics are taken as the feedback to the Engine Control Unit (ECU) to adjust the start of injection (SOI), pilot main timing and split, EGR level, boost level, fuel quantity, etc. Then the desired combustion phasing can be reached. Combustion phasing was found to affect exhaust emissions, thermal efficiency, and power output [13, 14]. One representative combustion phasing metric is the ignition delay, which is the time difference between the SOI and SOC [14,15].

Moreover, additional disadvantages of diesel engines associated with the diesel combustion process are the noise and vibration levels. Due to the compression ignition process of diesel engines, the high compression ratio and the high cylinder pressure causes higher vibration and noise than gasoline engine. The in-cylinder pressure directly acts on the cylinder chamber walls, piston, and piston head which can be transmitted

through the engine block to the block surface and the engine mount (REF). Also vibration can be introduced to the mechanical systems of the diesel engine by the piston movement which is driven by the in-cylinder pressure. This noise will radiate from the engine block due to the vibration. Therefore, the in-cylinder pressure can be considered as the main source of the engine vibration and noise radiation [16, 17, &18]. The relationship between the diesel engine noise level and the in-cylinder pressure signal was studied in this thesis. Based on the quantified relationship between the two, the engine noise level can be estimated with the in-cylinder pressure signal as the input.

1.2 Studies of interest

Two scenarios were studied in this thesis. First, the transfer path on a 9L I6 diesel engine between cylinder pressure and engine vibration signal as calculated with tri-axil block mounted accelerometers was modeled. Combustion metrics were estimated based on the transfer path with the vibration signal as the input. Second, the transfer path between the in-cylinder pressure and engine noise level as measured with microphones was studied on a 1.9L TDI diesel engine. From this, the engine noise level was estimated with the in-cylinder pressure and speed as the input.

1.2.1 Transfer path between engine vibration signal and combustion metrics

In-cylinder pressure signal has been historically used in the laboratory and more recently in series production to derive the combustion metrics and provide feedback for combustion phasing control [19-21]. However, the measurement of the in-cylinder pressure is typically obtained with intrusive sensors that require a special mounting process and engine structure modification. Also the in-cylinder pressure transducer has a high cost for mass production for diesel engines [22]. The engine vibration characteristics acquired through accelerometers mounted externally on the engine provide a path for a non-intrusive low cost sensor if they can be related to combustion characteristics [23]. In this dissertation block mounted accelerometers were used to reconstruct combustion

metrics so as provision for feedback in a closed-loop combustion phasing control scenario.

Goal and Objectives

The goal was to reconstruct the combustion metrics over varying engine conditions (SOI, speed, and load) based on the vibration signals acquired through accelerometers mounted on the engine block and engine head. Success of the reconstruction of combustion metrics depends on the development of a robust transfer path. Both the transfer path development and the combustion metrics reconstruction were performed on a medium sized diesel engine, John Deere 9L I6 280 kW. The reconstructed combustion metrics included SOC, CA50, PPA, PAA, PACL, MAPE, and PPCL. All these combustion metrics were extracted from the recovered in-cylinder pressure curve or apparent heat release rate (AHR) curve. Both frequency response function (FRF), which is based on a linear dependency assumption, and a nonlinear mapping tool, neural network, were applied to model the transfer path. The research objectives are listed as following:

- **Determine optimal accelerometer placement** – Determine the accelerometer location that has the strongest correlation with the combustion events to use in the single-input single-output (SISO) frequency response function (FRF).
- **Adapt FRF for varying engine conditions based on SISO FRF model –** Compute the SISO FRF from the optimal accelerometer channel based on one engine condition. Design an adaptation process to improve the robustness of the SISO FRF over different engine conditions with load and SOI variations.
- **Model the multiple-input single-output (MISO) transfer path with multiple accelerometer channels as the input channels –** Evaluate the MISO model and reduce the input channel number to a minimum based upon…. Compare the estimation results between the SISO and MISO models.
- **Model the transfer path with radial basis function neural network –** Construct and train a neural network to map the relation between the

accelerometer signal and the AHRR. Propose different neural network training methods and select one which has the best performance for application.

1.2.2 Transfer path between the engine noise level and the in-cylinder pressure signal

The construction of the diesel engine based on the compression ignition concept and the new combustion procedures designed to improve the fuel economy introduce more noise than the conventional gasoline engines [24]. So as to provide a quiet driving and operational environment, engine noise level is an important factor in the engine design and development process along with emissions, fuel economy, reliability, etc. [25-27]. Therefore, an evaluation procedure for the combustion noise level needs to be incorporated in the engine development process. To minimize time-consuming and expensive acoustic tests [18], engine noise level estimation based on the in-cylinder pressure signal, which can be obtained through an on-board load cell in-cylinder pressure sensor for each cylinder on a TDI engine [28], was investigated. Success of this work needs a reliable and robust transfer path developed between the in-cylinder pressure signal and the engine noise level.

Goal and Objectives

The goal for this section was to develop the transfer path between the engine noise level and the in-cylinder pressure signal on a 1.9L TDI diesel engine to reconstruct the radiated noise level with the measured in-cylinder pressure as the input. The research objectives are listed as following:

- **Perform an evaluation of the classical attenuation curve for estimation of the engine noise level –** apply the attenuation curve of a commercialized combustion noise meter to estimate the engine noise and evaluate the estimation results.
- **Compute the attenuation curve of the 1.9L diesel engine and optimize the attenuation curve –** compute the attenuation curve based on the measured in-

cylinder pressure and noise level on the 1.9L diesel engine and optimize the curve with two methods.

- **Develop an improved or new model for engine noise level estimation –** develop a linear model that results in a more accurate engine noise level estimation.

1.3 Dissertation outline

Chapter 1 presents the background for the research in this dissertation. The transfer path between combustion metrics and engine vibration signal, and the transfer path between combustion metrics and engine noise level are discussed. Two research aspects for application of the transfer paths, combustion metrics reconstruction and engine noise level estimation, are presented. Both the goals and objectives of the two research aspects are given in this chapter.

Chapter 2 reviews the literature which focuses on the combustion metrics reconstruction from reference signal and engine noise level estimations. Literatures involving reference signal selection, transfer path modeling, signal processing, etc. are also reviewed.

Chapter 3 covers the development of the models for the transfer path between the accelerometer signals and the in-cylinder pressure signal with SISO FRF on the 9L I6 diesel engine. An optimization process was applied to the SISO FRF which was obtained from one test condition to improve its robustness for additional engine conditions. The material contained in this chapter will be submitted to a journal in the future.

Chapter 4 covers the model for the transfer path between the accelerometer signals and the in-cylinder pressure signal based on the accelerometer signals acquired through multiple accelerometer channels on the 9L diesel engine. The multiple-input single-output (MISO) model was further simplified into a two-input one-output model without significant reduction in the accuracy. Comparison of the results was made between the MISO and SISO models. The material contained in this chapter was submitted to

“Proceedings of the Institution of Mechanical Engineers, Part C: Journal of Mechanical Engineering Science” and the current status is “Peer review in process”.

Chapter 5 covers the modelling for the transfer path between the accelerometer signals and the apparent heat release rate through a radial basis function neural network on the 9L diesel engine. Three training methods were applied to the neural network and results showed that the principal component analysis provided the best estimation efficiency and accuracy. The material contained in this chapter was published as a journal article [i].

Chapter 6 develops and evaluates the performance of the attenuation curve in estimating the engine noise level with the in-cylinder pressure signal as the input. Cepstrum smoothing technique was applied to pursue an optimized attenuation curve for the 1.9L diesel engine. Also, a new model for engine noise level estimation was proposed and established on this engine, and it was shown that this new model can provide a more accurate noise level estimation result than the structural attenuation curve method. The material contained in this chapter was submitted to “SAE International Journal of Engines” and the current status is “Peer review in process”.

Chapter 7 summarizes the research in this dissertation and the conclusions for the transfer path modeling between diesel engine combustion metrics and noise based upon vibration measurement on diesel engines. Finally, recommendations for future work are presented.

Chapter 2

Literature review[1]

2.1 Response signals for combustion events

2.1.1 Crank shaft speed fluctuation

Due to the variations of the in-cylinder pressure waveform during a combustion cycle, the crank shaft speed fluctuation varies in a complex way which depends on the engine parameters. How the speed fluctuation varies with the engine in-cylinder pressure changes has been explored by many researchers so as to develop a good alternative to the direct intrusive in-cylinder pressure measurement [29-37]. Based on a model that relates the crank-shaft speed and the in-cylinder pressure, the in-cylinder pressure can be estimated with the input of instantaneous speed signal measured by a crank-shaft speed sensor. The sensor can be an optical encoder or a magnetic pickup transducer which are easy to mount and low in cost.

Moro et al. [29] proposed a linear dependency between the in-cylinder pressure and the engine speed signal and experimentally verified it for 38 different engine running conditions. The equation that can represent this linear dependency is given as [29]:

$$Ar\left(p(t) - p_{misf}(t)\right) f_{crank} = J\ddot{\theta}_s(t) - \ddot{\theta}_{s\,misf}(t) = J\Delta\ddot{\theta}_s(t) \qquad (2.1)$$

[1]The material contained in this section is planned for submission as part of a journal article and/or conference paper in the future.

Where A is piston area in m^2, r is the crank radius in m, p_{misf} is the in-cylinder pressure in case of misfire (bar), $\ddot{\theta}_s$ is the synthetic engine acceleration in rad/s^2, $\ddot{\theta}_{s\,misf}$ is the synthetic engine acceleration in case of misfire rad/s^2, J is the moment of initial ($kg \cdot m^2$), and f_{crank} is the crank-slider kinematics function.

A frequency response function between the in-cylinder pressure and the engine speed can be obtained by converting equation 2.1 into frequency domain. However, this FRF is sensitive to engine running conditions and the FRF obtained based on one conditions does not lead to the estimated in-cylinder pressure with high accuracy when condition varies. So a FRF mapping was created in this paper based on 38 different steady-state engine conditions with the engine speed and the manifold pressure as the condition parameters to distinguish different test conditions. For the conditions falling into the FRF mapping, interpolation technique was used for both real and imaginary harmonic components to obtain the estimated FRF. The pressure recovery results for low speed low load, high speed low load, and low speed high load conditions were shown in this paper.

Connolly and Yaggle modeled the cylinder combustion pressure via the crank-shaft velocity from a statistical point of view [30]. The model involves three sequent components. First, by replacing the time domain independent variables with crank-angle variables, a non-linear differential model between the crank's shaft speed and the in-cylinder pressure signal can be simplified. Secondly, the in-cylinder pressure signal was parameterized by the sample modeling sequence based on a stochastic model which uses the sum of the deterministic waveform and an amplitude-modulated cosine window. Third, an estimation of the in-cylinder pressure based on the crank-shaft speed signal was achieved through a state-space deconvolution process which utilized a Kalman filter. Moreover, signal to noise ratio effects to the in-cylinder pressure estimation were also evaluated in this paper. Results showed that for low to moderate noise level conditions the reasonable deconvolution can be reached.

Shiao et al. [31] employed a sliding observer to estimate the in-cylinder pressure and combustion heat release for an SI engine. To estimate the in-cylinder pressure with high

accuracy, the error between the measured and the estimated crank-shaft speed was taken as the feedback to reduce the dynamic error of the estimated in-cylinder pressure. The unobservability problem arises for the pressure estimation around the top dead center and thus introduces significant estimation error. This problem was partly solved by adapting the parameters of the observer. Then the estimated in-cylinder pressure was used to compute the cylinder heat release. Also, detection of misfire or abnormal combustion events was achieved through the estimated heat release.

Additional investigators examining combustion metrics analysis based on the crank-shaft speed fluctuation can be found in [32-34]. In addition to estimating the in-cylinder pressure waveform and the heat release, engine crank shaft speed was also used to recover the engine torque [35-37]. For most cases, the crank shaft speed was fed into an engine model which was simplified based on assumptions to estimate the engine torque.

2.1.2 In-cylinder ion current

Ion current in the combustion chamber is measured via the spark plug. After the high-voltage discharge, the ion current across the spark plug gap is obtained by applying a DC voltage across the gap and measuring the resulting current. The ion current is affected by gas flow, geometry of flame, electric potential, ion density, and the angle between the flame and electrode [38]. The ionization of gases in the cylinder occurs in two phases. When the fuel reacts with the oxygen during combustion, the first phase ionization occurs which can be considered as chemical phase. The second phase, defined as thermal phase, occurs when the burnt gases are compressed by the increased in-cylinder pressure [39].

The most consistent dependency between the ion current and in-cylinder pressure occurs on the peaks of the two signals for both amplitude and the location perspectives. This has been verified by the researches in [38-43]. Martychenko [12] detected the breakdown voltage across the spark plug gap and modeled the relationship between the peak of the voltage and the peak the in-cylinder pressure based on second order polynomial function. The coefficients of the second order polynomial function for the conditions with varied engine speed are different. However, the coefficients can be curve fitted by a linear

function of engine speeds. Hellring [39] proposed a least squares fit method to estimate the in-cylinder pressure peak position of spark ignited engines based on the ion current signal. This method was proved to have a better robustness and accuracy than multilayer perceptron and Gaussian curve fit methods for peak in-cylinder pressure estimation.

Gazis et al [44] explored the possibility of estimating in-cylinder characteristics based on the ion current with one simple and computationally inexpensive neural network, adaptive linear type of network. Thirteen extracted characteristics of the ion current were taken as the input and four characteristics of the in-cylinder pressure (peak pressure position, peak pressure magnitude, the width of curve at half of its height, and the area of the curve between inlet valve closing (IVC) and exhaust valve opening (EVO)) as the output to train the network with the purpose of predicting the four characteristics of in-cylinder pressure. Also, based on the same neural network structure but with the whole ion current signal (time domain sampled between IVC and EVO) as the input and the whole in-cylinder pressure signal (time sync'd with ion current signal) as the output, the in-cylinder pressure curve rather than just some characteristics of the in-cylinder pressure signal can be estimated. The peak pressure location, as one of the most important in-cylinder pressure characteristics, was predicted with the mean error at 0.062 degrees and standard deviation at 2.55 degrees.

Ion current was also used to detect engine knock, misfire, or incomplete combustion [42, 45-47]. Kumar et al. [42] applied a band-pass filter on the ion current signal and the filtered output indicates the engine knock. Danne et al. [45] compared the ion current based knock detection with the conventional methods of pressure-based and accelerometer-based knock detection on a large-displacement, air-cooled, V-twin motorcycle engine. It was found that the ion current based method can detect the inaudible knock more accurately and reject the mechanical noise more effectively than the other two conventional methods. Zhu et al. [46] found that the in-cylinder ion current can detect misfire or incomplete combustion. Also, the ion current signal can be used to compute minimum spark advance for best torque (MBT) to measure the combustion

stability [46, 48]. However, the results are only limited to a fixed load over a narrow speed range.

2.1.3 Accelerometer signal

Accelerometers are mounted externally on the engine block or the engine head to detect the combustion events by measuring the vibration signals which are transmitted from the in-cylinder oscillation to the engine outer surface. However, as the accelerometer detects the vibrations from the sources in addition to the cylinder oscillation including the valve dynamics, piston slaps, etc., the signal may vary from cylinder to cylinder and over operating conditions. So the utilization of the accelerometer signal for combustion metrics detection relies on the signal processing technique which can eliminates the effects from other sources.

Naber et al. [49] evaluated the effectiveness and accuracy of accelerometer-based knock detection. The distributions of the accelerometer-based knock intensity metrics for various operation conditions including varied speeds, loads, cam timings, and knock levels were measured and fitted by a log-norm distribution. The log-norm model was verified to provide a good fit of the distributions and the distribution characteristics including skewness and peakness. In addition, a good correlation can be seen between the cylinder pressure based knock intensity metrics and the accelerometer-based knock intensity metrics. Guillemin [50] estimated the instantaneous engine knock by fitting the accelerometer signals with Gaussian function on a 2.2L HCCI engine and measure the start of combustion where the knock level is out of the user-defined threshold.

Characteristics of the accelerometer signal which are related to the characteristics of in-cylinder pressure or apparent heat release rate were investigated and extracted [51-53]. These characteristics of the in-cylinder pressure or apparent heat release including start of combustion, CA50, and PPCL are closely related to the combustion process and thus can be used as the feedback to control the combustion process. Arnone et al. [51] band-pass filtered the in-cylinder pressure signal and the accelerometer signal within 650-1000Hz and found that the accelerometer signal can locate the sudden rise of the in-cylinder

pressure signal (so as to denote the start of combustion), diffusive combustion process, and the peak of the in-cylinder pressure on a water cooled Lombardini LDW442CRS direct injection common rail diesel engine. Chiavola et al. [52] computed the cumulative heat release based on the measured in-cylinder pressure and investigated the relationship between the accelerometer signal and the cumulative heat release on a two cylinder diesel engine equipped with a common rail injection system. By superimposing the filtered accelerometer signal to the cumulative heat release, it was found that the filtered accelerometer signal can locate the start of combustion, the beginning of main combustion, and MFB50 (50% of the burnt fuel mass). Taglialatela [53] investigated the correlation between the in-cylinder pressure signal and the features derived from the accelerometer signal on a 4L single cylinder SI engine. Time-frequency spectrogram method was utilized to analyze the accelerometer signal to present more features of the accelerometer signal than the analysis in time domain. The result indicates a direct correlation between the peak pressure location and the maximum amplitude of accelerometer signal in time-frequency domain for all the engine operating conditions conducted in this paper. So the maximum amplitude location of the accelerometer signal can be used as the feedback for a closed-loop control system of spark advance.

Polonowski et al. [54] explored the potential of accelerometers to recover the in-cylinder pressure curve on a 1.9L four cylinder, turbocharged, HPCR, direct injection diesel engine. In this paper, standard signal processing techniques including Fast Fourier Transform (FFT) and coherence were employed and results showed that a strong coherence presented between the in-cylinder pressure signal and the accelerometer signal within frequency band of 0.5 kHz to 4 kHz with the coherence value over 0.9. Also, this research found that the accelerometer location did result in a varied coherence value between the in-cylinder pressure signal and the accelerometer signal. The optimal locations for the accelerometer placement were determined based on both offline and online coherence analysis. In his later work [55], frequency response function (FRF) was used to quantify the relationship between accelerometer response and AHR, and the relationship between accelerometer response and in-cylinder pressure. A technique

termed as spectrum weighting was utilized to combine FRFs from all conducted test conditions into a single FRF by weighting the FRF magnitude and phase information for each frequency by the coherent output power at that specific frequency. Equation 2.2 described coherent output power weighting matrix, and equation 2.3 explains how these FRFs were combined by means of coherence output power computed by equation 2.2.

$$w_{CP}(TN, f) = \left(\frac{\begin{bmatrix} \sum(C(f)_{TN(1)} * P(f)_{TN(1)}) \\ \sum(C(f)_{TN(2)} * P(f)_{TN(2)} \\ ..... \\ \sum(C(f)_{TN(NT)} * P(f)_{TN(N)} \end{bmatrix}}{\sum \begin{bmatrix} \sum(C(f)_{TN(1)} * P(f)_{TN(1)}) \\ \sum(C(f)_{TN(2)} * P(f)_{TN(2)} \\ ..... \\ \sum(C(f)_{TN(NT)} * P(f)_{TN(N)} \end{bmatrix}} \right)' \tag{2.2}$$

Where:

$C(f)$: Coherence as a function of frequency

$P(f)$: Autopower as a function of frequency

TN: Test number

w_{CP}: Coherent power weighting matrix

$$H(f) = \sum_{i=1}^{NT} \left(w_{CP}(TN, f) * \begin{bmatrix} H(f)_{TN(i)} \\ H(f)_{TN(2)} \\ .... \\ H(f)_{TN(i)} \end{bmatrix} \right) \tag{2.3}$$

Where:

TN: Test number

NT: Number of tests

$H(f)$: Frequency response function in frequency domain

$w_{CP}(TN, f)$: Coherent power weighting matrix

This obtained FRF was used to estimate in-cylinder pressure and AHR on a cycle-cycle basis. The maximum pressure gradient determination was shown to have a root mean square error (RMSE) accuracy of 15% of actual maximum pressure gradient. The location based metrics had the RMSE as small as 0.29° and more than 80% of the estimated peak apparent heat locations were within 1° crank-angle.

Among the fore-mentioned three signals for combustion metrics estimation or correlation, accelerometer signal was most utilized because the accelerometer has the advantage of low price and easy mounting as well as high reliability and durability. Also, utilization of multiple accelerometers which are placed at multiple locations on engine block can supply more than one input channels which have the potential of improving the combustion metrics estimation accuracy with the assistance of signal processing. The limitation of usage of crank shaft signal is that the instantaneous output torque near TDC where CI engine combustion typically starts is zero [14]. Also, the dynamics of the system limit the dynamic content of the signal. Ion signals are dependent on engine conditions including speed, load, boost, air/fuel ratio, fuel additives, and spark plug condition [48]. So the accuracy of the combustion metrics estimation will be affected by the changes of these dependent conditions. Also, as deposit accumulation on the ion probe electrodes will decrease the ion current signal, a self-cleaning mechanism must be considered in its application [48].

2.2 Signal processing techniques to correlate the combustion metrics and the response signal

2.2.1 Frequency response function (FRF)

The pressure curve recovery depends on the transfer path modeling between the acquired source signal (in-cylinder pressure signal) and the response signal (vibration signal for example). Frequency response function which represents the frequency domain

relationship between the in-cylinder pressure signal, $P(\omega)$, and the accelerometer signal, $A(\omega)$, can be presented by Equation 2.4:

$$A(\omega) = P(\omega)H(\omega) \tag{2.4}$$

$H(\omega)$ is the transfer path in frequency domain and is defined as the frequency response function (FRF). With the FRF obtained by measuring both $P(\omega)$ and $A(\omega)$ based on the representative operating conditions, the in-cylinder pressure signal of any other condition can be recovered with the measured $A(\omega)$ and the obtained $H(\omega)$ by equation 2.5:

$$P(\omega) = A(\omega)H^{-1}(\omega) \tag{2.5}$$

However, as the response signal is sensitive to not only the in-cylinder pressure oscillation but the rotating crank-slider and vibration from other mechanical parts including piston slaps and valve dynamics which varies with the engine operating conditions, the FRF with assumption of linear dependency in frequency domain between the source signal and the response signal does not have a good robustness over engine operating conditions. This conclusion has been confirmed by researchers [55-58]. Gao et al. [56] applied the FRF computed from 2400rpm full load condition to reconstruct the in-cylinder pressure with the accelerometer signal measured at 3600rpm and full load condition as the input. The significant recovery error for the in-cylinder pressure waveform indicated that the transfer path modeled by FRF cannot be considered consistent over engine operating conditions. Morello [57] attempted to overcome the drawback of FRF application for the heat release recovery based on the accelerometer signal by optimizing the time domain window applied to the accelerometer signal. Also, a Vold-Kalman order tracking filter was employed to eliminate the abnormal harmonics of the singular value decomposition results of both the accelerometer signal and in-cylinder pressure signal. However, no significant heat release estimation accuracy improvement can be seen for a start of injection (SOI) sweep test conditions. Polonowski [55] also tried to improve the FRF performance by adding a weighting function to the FRF as shown in equation 2.2. However, the robustness improvement for FRF is still limited.

Gao et al. [56] explained why the variation of the FRF results in an error of source estimation with the Laplace transform. It can be seen that the variation of FRF introduces incomplete cancellation of the poles and zeros in the dominator with the accelerometer signal as the numerator. The incomplete cancellation of non-minimum-phase zeros will make the extra poles or zeros of FRF present and make the inverse filtering unstable. As a result errors will be introduced to the estimation result.

2.2.2 Cepstrum analysis

Complex cepstral analysis is a nonlinear homomorphic signal process which is being utilized in many areas including machine diagnostics, image processing, speech, and radar signal processing. A cepstrum is reached by taking the inverse Fourier transform of the logarithm of a signal spectrum. The complex cepstrum $X_c(t)$ can be expressed as:

$$X_c(t) = F^{-1}\{\log\left(F\{x(t)\}\right)\} \tag{2.6}$$

$x(t)$ is the signal in time domain, F represents the Fourier transform algorithm, and F^{-1} denotes inverse Fourier transform.

Equation 2.7 can be obtained by applying logarithm to equation 2.4:

$$\log(A) = \log(P) + \log\left(H\right) \tag{2.7}$$

After computing the inverses Fourier transform:

$$F^{-1}(\log(A)) = F^{-1}(\log(P)) + F^{-1}(\log\left(H\right)) \tag{2.8}$$

According to equation 2.6, the cepstrum of FRF can be obtained as:

$$H_c(t) = A_c(t) - P_c(t) \tag{2.9}$$

The advantage of this method is that the convolution process is converted to an addition process in cepstrum domain. El-Ghamry et al. [59] applied the complex cepstrum analysis on the root mean square acoustic emission signal. The complex cepstrum of FRF, $H_c(t)$, was evaluated for four complete combustion cycles at 1280rpm 30Nm condition.

By inserting the $H_c(t)$ and the $A_c(t)$ into equation 2.9, the cylinder pressure signal can be identified as:

$$P_c(t) = A_c(t) - H_c(t) \tag{2.10}$$

However, this method only gave good estimation of the in-cylinder pressure signal for the same engine operating conditions based on which the $H_c(t)$ was computed.

Another important application of complex cepstral analysis is for signal smoothing. The complex cepstrum was utilized to improve the robustness of the transfer path by smoothing both the source signal and the response signal [56, 60, &61]. Smoothing the FRF actually reduces the variations of the FRF associated with different operating conditions. The schematic illustration for smoothing the FRF is shown in Figure 2.1.

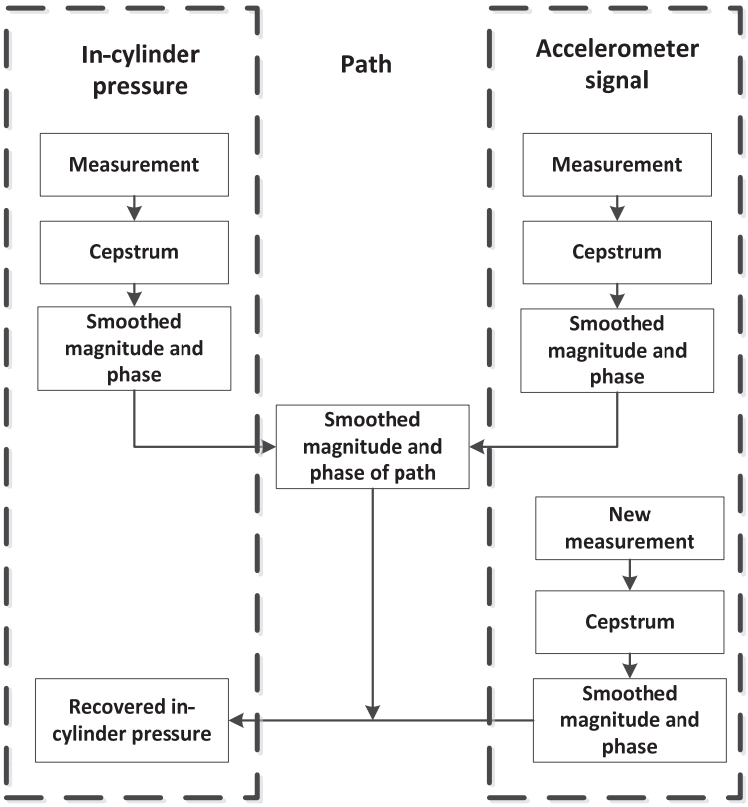

Figure 2.1: In-cylinder pressure estimation based on the cepstral smoothing technique

In the process described in Figure 2.1, the smoothing of magnitude and phase was realized by applying a low-pass filter in quefrency domain to lifter the corresponding content of complex cepstrum. In other words, the liftering process was achieved by applying a window around zero quefrency. Kim [60] also discussed the effects of the window length in the signal smoothing and results showed that the shorter the window, the smoother the log spectrum. The smoothed amplitude and phase of FRF was obtained through equation 2.9 by smoothing the phase and amplitude of both the accelerometer signal and the premeasured in-cylinder pressure under the given conditions. By inserting the smoothed FRF into equation 2.10, the in-cylinder pressure signal was recovered by inputting the smoothed accelerometer signal measured from the same conditions on another engine structure of the same type.

Gao [56] applied the complex cepstral smoothing technique to obtain a smoothed FRF for in-cylinder pressure recovery. They compared the results based on four different in-cylinder pressure recovery methods, including two inverse filtering procedures (equations 2.5 and 2.10), the cepstral smoothed FRF, and the time domain smoothed FRF. It showed that the pressure waveforms recovered from the two smoothing operations can better match the measured ones than the pressure waveforms recovered from the two inverse filtering operations.

2.2.3 System identification

FRF method assumed a linear dependency in frequency domain between the in-cylinder pressure and the vibration signal. However, the low robustness of the FRF with respect to the engine operating condition variations proved that the linear dependency needs to be adapted. System identification approach modeled the transfer path between the in-cylinder pressure and the accelerometer signal with a nonlinear hypothesis. Villarino [62] modeled the transfer path as a filter which was applied to the in-cylinder pressure signal to output the accelerometer signal. Also, it was assumed that the accelerometer signal consists of a superposition of K components with each component for one cylinder. The model was expressed as:

$$a_n = \left(1 - B(q^{-1})\right)a_n + \sum_{k=1}^{K} H_k(q^{-1}, n)p_{k,n} + \omega_n \quad (2.11)$$

a_n as the measured accelerometer signal is the sum of the in-cylinder pressure p_n filtered by a time-variant filter $H_k(q^{-1}, n)$,past accelerometer samples termed by $B(q^{-1}) = 1 + \sum_{m=1}^{M} a_m q^{-m}$, and the noise termed by ω_n. q^{-1} is the left shift operator and works as $q^{-m}a_n = a_{n-m}$.

The optimal filter coefficients $\hat{B}(\cdot)$ and $\widehat{H_k}(\cdot)$ were estimated by minimizing the error $\epsilon_n$between the estimated in-cylinder accelerometer signal $\widehat{a_n}$ and the measured one a_n:

$$\left[\hat{B}, \hat{H}_1, \ldots . \hat{H}_k\right] = argmin(\sum_{n=1}^{N} \epsilon_n^2) \quad (2.12)$$

For the ease of reconstruction of the in-cylinder pressure, in-cylinder pressure trace was decomposed into three parts which are associated with the same dependent parameters. Expectation maximization algorithm was employed to recover the dependent parameters. The results showed that the peak pressure location estimation yields a mean error of 0.04° with the standard deviation at 4.78°. However, the high estimation accuracy was limited to the same engine operating conditions. No results were reported when this method was applied to a varied engine operating condition.

Wagner [63] built a physical model which denoted the speed dependence of the transfer path between the in-cylinder pressure and the accelerometer signal. SGN algorithm was used to identify the parameters of the transfer function speed-independently. Each pressure in this paper was considered to be composed of two parts with the first one introduced by the compression due to the piston movement and the second one generated by the pressure rise due to the combustion event. As the parameters were identified speed-independently, only one set of transfer path parameters needs to be stored for the in-cylinder pressure estimation.

Other than recovering the in-cylinder pressure signal, system identification approach was also used for misfire detection [64-66]. A function was developed to interpret the ratio between the energy of the signal and the energy of the noise, termed as signal energy to

noise ratio in Villarino's work. A higher load can cause the signal energy-to-noise ratio to increase. A threshold value was determined with the function value lower than the threshold value indicating the occurrence of the misfire.

2.2.4 Neural network

The modeled transfer paths described in the previous sections only work for limited engine operating conditions. The transfer behavior between the accelerometer and the combustion metrics (with the in-cylinder pressure as the example) is a nonlinear dynamic path highly depending on the input and the engine operating condition. For this reason, another nonlinear modeling approach, neural network, was employed to investigate the relationship between the combustion metrics and the response signal, including crank speed fluctuation [30, 33], the vibration signal [67], and hybrid of crank speed fluctuation and vibration signal [68].

Gu [33] modeled the relationship between the cranks shaft speed and the in-cylinder pressure with a radial basis function (RBF) neural network on a four cylinder DI diesel engine. With network trained with the selected data and the in-cylinder pressure can be expressed as:

$$y_{kj}(\theta) = \sum_{m=1}^{M} h_{km}(\theta) w_{mj} \tag{2.13}$$

Where $h_{km}(\cdot)$ is the radial basis function and w_{mj} are the weighting vectors. The RBF is composed of a linear layer represented by equation 2.13 and a non-linear layer with radial basis functions as the components. The radial basis function is expressed as:

$$h_{km} = \exp\left(-\frac{\|x_k - c_m\|}{r_m}\right) \tag{2.14}$$

Where c_m is the hidden unit center, x_k represents the crank speed input, and r_m is the radius of the Gaussian function. $\|\cdot\|$ represents the Euclidean distance between the vectors. Results showed that the recovered pressure waveform match well the measured one for nine engine conditions with varied engine speeds and loads for all the phases: compression, peak pressure and rise and fall of the combustion. Indicated mean effective

pressure (IMEP) was also computed based on the recovered in-cylinder pressure signal and the IMEP from the recovered in-cylinder pressure can follow the respective measured values closely.

Taglialatela [22] utilized the Multi-Layer Perceptron neural network to model the relationship between the crank shaft speed and parameters extracted from the in-cylinder pressure, including peak pressure value and peak pressure angular location, instead of the pressure waveform. With the trained neural network, the peak pressure amplitude can be estimated with minimum error of 2.31bar and maximum error of 6.97bar which are 4.1% and 8.0% respectively in relative percentage scale. The peak pressure location can be estimated with minimum error of 1.38 crank-angle degrees and maximum of 5.20 crank-angle degrees.

Bizon et al [67] reconstructed the in-cylinder pressure signal on a single cylinder 0.5L diesel engine with the engine block vibration as the input signal to a trained RBF neural network. This paper focused on the RBF neural network parameters optimization with respect to the number of neurons and the spread parameter. 50 centers and spread parameter of 3.2 were finally determined and the RBF network structured with the optimized parameters were evaluated based on the peak pressure amplitude, peak pressure location, and the MBF50 which are derived from the recovered in-cylinder pressure. The peak pressure value estimation error was under 3% in relative RMSE and the peak location and MBF50 were below both 1.5 crank-angle degrees.

Johnsson [68] also employed the RBF neural network for the in-cylinder pressure recovery but with the hybrid of vibration signal and the crankshaft speed as the input on a 9-litre, 6-cylinder, and inline four-stroke diesel engine. Because the coherence analysis indicated that the crankshaft angular speed has the highest coherence with the in-cylinder pressure for the lowest frequency while the vibration signal has the highest coherence with the in-cylinder pressure for higher frequency. A recursive hybrid learning procedure was applied to train the neural network. *K-means* clustering algorithm found the *k* centers and used the regularization to determine the weights. Fourier transform of vibration

signal and the crankshaft signal are taken as the input to the RBF neural network, so both the input and output are complex values. The training data and the validation data are presented in Figure 2.2:

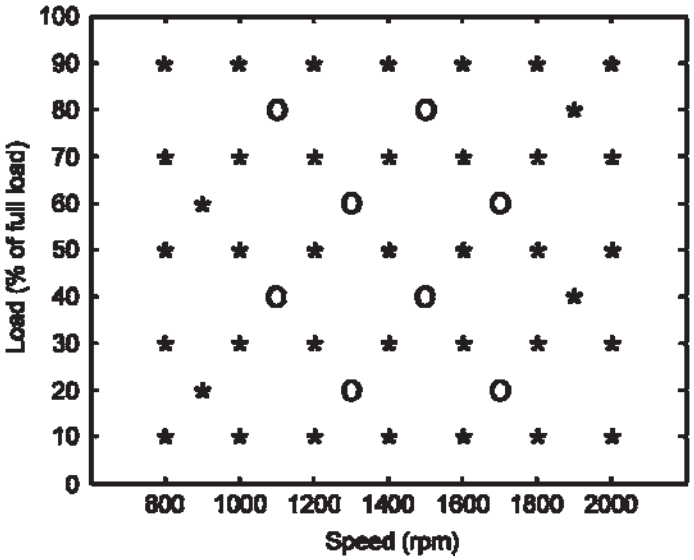

Figure 2.2: Engine operating conditions (o: validation data; *: training data) [68]

The results showed that the RMS error of maximum pressure based on the validation data was 3.5bar, the location for the maximum pressure was 1.5 degrees, RMS error for IMEP was 0.7bar.

2.2.5 Wavelet method

Although the frequency domain signal processing techniques including the Fourier transform and the FRF has the advantages in analyzing the raw signal and building the transfer path, the Fourier transform result is inefficient for non-stationary problems such as the engine vibration signal with the non-stationary effects introduced by the combustion events [69]. Also, the Fourier-transform-based technique is not capable to detect the temporal variations of the periodicities due to its pure frequency domain dependency [70]. Wavelet transform as a popular time-frequency-transform decomposes the signal into different frequency bands and allows the feature analysis associated with these frequency bands. This property makes wavelet transform a useful tool to analyze

the signals with time discontinuities and sharp spikes, such as the vibration signal or the radiated sound of an engine during combustion.

Kim and Min [71] applied the Meyer wavelet transform to the engine block vibration signal obtained on a controlled auto-ignition engine to detect the start of combustion which was defined as 2% mass fraction burned. The engine block vibration signal within 500Hz to 7 kHz was converted into wavelet scale with an interval of 100Hz. A threshold value was determined to correspond to the start of combustion and the wavelet scale which grows greater than this threshold value was used to locate the start of combustion for each frequency band. Then the averaged start of combustion for each frequency band was the final determined result. Figure 2.3 indicates the engine block vibration wavelet transform results and the start of combustion was determined at 363 crank-angle degrees (3 degrees after top-dead center).

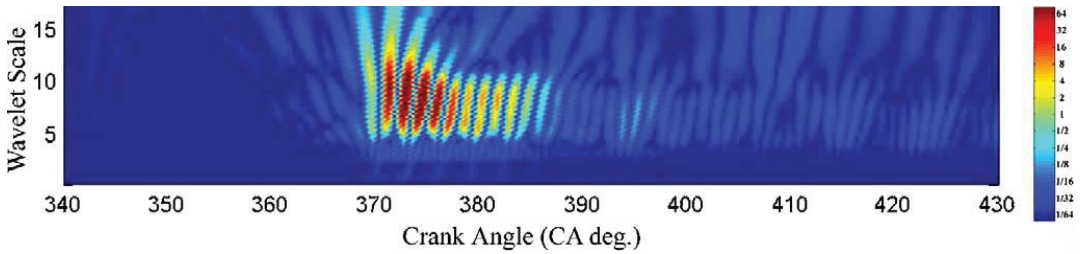

Figure 2.3: Wavelet transform result in a specific cycle for 1500rpm [71]

Hariyanto et al. [72] defined the pressure-based start of combustion based on derivatives of the pressure trace and took it as reference. The technique for the start of combustion determination based on the vibration signal wavelet analysis used the trial and error method. Results showed that the averaged difference of the start of combustion between the two determination methods is below 1 crank-angle degree. The correlation coefficient of the start of combustion derived from in-cylinder pressure and the accelerometer signal is higher than 0.95.

As the wavelet transform presents more details about the signal in time-frequency domain, features extraction can be achieved based on the wavelet transform analysis. Then the correlation between the features extracted from the vibration or sound signal

and the features extracted from the in-cylinder pressure trace was investigated. However, no transfer path based on the wavelet transform has been developed and applied for the pressure waveform recovery. More researches concerning application of wavelet transform for engine combustion or engine radiated noise can be found in [69, 70, &73].

2.3 Engine noise level estimation

In-cylinder pressure and mechanical forces are the major sources of engine noise. The pressure forces operate on the cylinder chamber wall and piston and create a downward force through the piston and connecting rod to the crankshaft and main bearings, these combined reactions cause the vibration of the engine block. Noise will radiate from the engine block due to its vibration. So the major sources of the engine noise can be characterized and connected through the in-cylinder pressure.

To explore the effects of the in-cylinder pressure on the engine noise, Austen and Priede [16] modeled the transfer path between the in-cylinder pressure and the engine noise with an “attenuation curve”. In this approach, it is assumed that the engine block is a linear system. The AVL 450 combustion noise meter was developed based on this theory. Shahlari et al. [17] has verified the engine noise computation algorithm (attenuation curve) of the AVL 450 in Matlab and applied it to three different engine structures. With the in-cylinder pressure as the input to the combustion noise meter, the error between the noise meter output and the results based on microphone measurements are as low as 0 dBA. However, the robustness of the attenuation curve for quantitative analysis is still suspect since the linear response of engine block is expected regardless of engine structure or engine working conditions.

While studying the attenuation curve depending on the raw in-cylinder pressure signal, Jung et al. [74] created a new combustion noise index based on the in-cylinder pressure, the sum of the 1-3.15 kHz range of the third octave band levels of the in-cylinder pressure. It was found that the combustion noise index has a linear dependency with the combustion noise (sum of the 1-3.15 kHz range of the third octave band levels of the

measured engine noise) for 1250rpm to 2000rpm engine conditions. However, the customers care about the total engine noise more than just the combustion noise. Tousignant et al. [75] defined the engine radiated noise as the sum of the noises due to direct combustion, indirect combustion, flow, and mechanical forces. An arithmetic weighting function was determined and applied to each source excitation. This approach has a more reasonable physical explanation about the engine noise sources. However, other excitation sources in addition to the in-cylinder pressure must be measured including rotary force, gas mass flow, etc.

2.4 Literature review summary

Current and past research for combustion measurement is interested in the indirect measurements with the sensors not exposed to the combustion chamber. Accelerometer is the representative sensor used for indirect combustion measurement with the advantage of low price and easy mounting as well as high reliability and durability. A majority of current accelerometer-based combustion measurement research focuses on identifying correlations between the block mounted accelerometer signal and the in-cylinder pressure signal and modeling the transfer path between the two signals.

Many of the methodologies used to quantify the relationship between the accelerometer signal and the in-cylinder pressure signal show promising results. However, the proposed methods used to model the transfer path, including FRF method and structural identification method, are only applicable for test conditions with limited variations of speed, load, and SOI. Also, a majority of the researches were performed on one or two cylinder engines which are relatively small in size with low power output.

The primary goal of this dissertation is to model the transfer path between the in-cylinder pressure signal (or the AHR derived from cylinder pressure) and the accelerometer signal in a robust manner on a 9L 6 cylinder diesel engine with the maximum power output at 280 kw. In-cylinder pressure estimation based on FRF theory is applied in this dissertation. Research focuses on improving the robustness of FRF by adding adaptation

process to the SISO model and exploring MISO FRF models. By adding an adaptive segment in SISO FRF model the FRF computed from one engine condition can be applied to additional conditions with varied SOI and load. Based on a MISO FRF model, the FRF computed from one engine conditions can adapt to engine conditions with varied speed, load, and SOI. Research in this dissertation greatly promotes the application of FRF model for combustion metrics estimation. In addition, neural network is explored in the dissertation to model the relationship between accelerometer signal and the AHR. More than pursuing accurate estimation results, efforts focus on improvement of the network training efficiency.

Engine noise level estimation based on structural attenuation curve (initially proposed by other investigators) with the input from in-cylinder pressure signal is examined on a 1.9L four cylinder, turbocharged, HPCR, direct injection diesel engine. Optimization of the attenuation curve is performed to further improve the estimation accuracy on this engine. Also, linear model with the engine speed and in-cylinder pressure as the components is explored to provide more accurate noise level estimation results than the attenuation curve.

The technical information regarding the engine, method, and applicability over speed, load and SOI variations is shown in Table 2.1.

Table 2. 1 Summary of studies relating to this dissertation work

Author	Engine	Method used	Objective	Applicability
Morello [58]	Diesel engine 9L 6cylinder	FRF, time-domain window optimization, Kalman filter	Recover the AHR	2200rpm, 725Nm, SOI sweep
Polonowski [55]	Diesel engine 1.9L 4 cylinder	FRF, weighting function development for FRF	Recover the in-cylinder pressure signal and AHR	Speed, load, and SOI variations
Kim [60]	Diesel engine 6 cylinder	Cepstrum analysis, parameter modification	Recover the in-cylinder pressure signal	1600rpm, 1150ft-lb, the transfer path can adapt to three different accelerometer locations
Gao et al. [56]	Diesel engine single cylinder	FRF, cepstrum smoothing of FRF	Recover the in-cylinder pressure signal	Load variations at the same speed
EI-Ghamry et al. [59]	Diesel engines four cylinder	FRF, complex cepstrum modeling,	Recover the in-cylinder pressure signal	Load variations at the same speed
Taglialatela et al. [22]	Gasoline engine Single cylinder	Multi-Layer Perceptron neural network with input from crank shaft speed	Recover combustion metrics including PPA and PPCL	Speed and load variations

Table 2. 1 Cont'd

Author	Engine	Method used	Objective	Applicability
Gu et al. [33]	DI diesel engine Four cylinder	Radial basis function with input from crank shaft speed	Recover in-cylinder pressure and IMEP	Speed and load variations
Johnsson [68]	Diesel engine 9-litre, 6-cylinder, and diesel engine	Radial basis function with input from hybrid of crank shaft speed and accelerometer signal	Recover in-cylinder pressure and estimate the combustion metrics including max pressure rising rate, IMEP.	Speed and load variations
Shahlari et al. [17]	Diesel engines 1.9L single cylinder & 1.9L four cylinder	Structural attenuation curve	Estimate the engine noise level	Speeds: 1000 to 3000rpm, Loads: 4.28 to 14.13 Bar IMEP
Tousignant et al. [75]	Two different engines (no more information provided)	Weighting function and transfer function	Estimate the engine noise level	Speed sweep conditions and load variations
Torregrosa, A. J., et al. [18]	Diesel engines 1.6 L and 2.2L four-cylinder	Structural attenuation curve, linear model development	Estimate the engine noise level	Speed and load variations

Chapter 3

FRF adaptation[1]

An accelerometer as a low-cost non-intrusive transducer for sensing the combustion events in a diesel engine was investigated via reconstruction of in-cylinder pressure by use of an adapting frequency response function (FRF). As the noise introduced into the accelerometer signal and the response to combustion vary with the operating condition, the FRF computed from a single test condition only works for the same or similar conditions. To overcome this limitation, an adaptation process for the FRF is explored to improve the FRF's robustness to other operational conditions with start of injection, start of combustion, and load variations. Frequency domain analysis shows that only the low frequency content is determinant for the in-cylinder pressure reconstruction, and the adaptation of the first and second (0Hz and 121Hz) harmonics of the FRF results in the greatest improvement for the in-cylinder pressure estimation accuracy. The 0Hz harmonic is adjusted based on the premeasured in-cylinder pressure offset and the on-line measured accelerometer signal offset. Particle swam optimization as a computational algorithm is applied to adapt the 121Hz harmonic of FRF. The results show that the adapted FRF, in comparison to the un-adapted FRF, can reduce the phase error up to 1.3 degrees and the amplitude error by up to 90 percent.

[1] The material contained in this section is planned for submission as part of a journal article and/or conference paper in the future.

3.1 Experimental setup & test conditions

Testing was conducted on an inline 9L 6-cylinder turbocharged diesel engine with high pressure common rail fuel injection. The specifications of this engine are given in Table 3.1.

Table 3.1: 9L diesel engine parameters

Engine specification		
Variable	**Value**	**Units**
Displacement	9	L
Cylinder	Inline	N/A
# of Cylinders	6	Cylinders
Peak torque@1500	1543	Nm
Peak power @2200	228	kW
Stroke	13.6	cm
Compression ratio	16:1	N/A

Tri-axial PCB model HT356A63 sensors with a measurement range of ±500 g were used to measure the engine vibration signature. The in-cylinder pressure was measured by a Kistler 6123A piezoelectric cylinder pressure transducer mounted in each cylinder head. A Hewlett-Packard VXI mainframe was used for data acquisition with sampling rate and acquisition time length set as 51.2 kHz and 40s. Figure 3.1 illustrates the placements for the accelerometers.

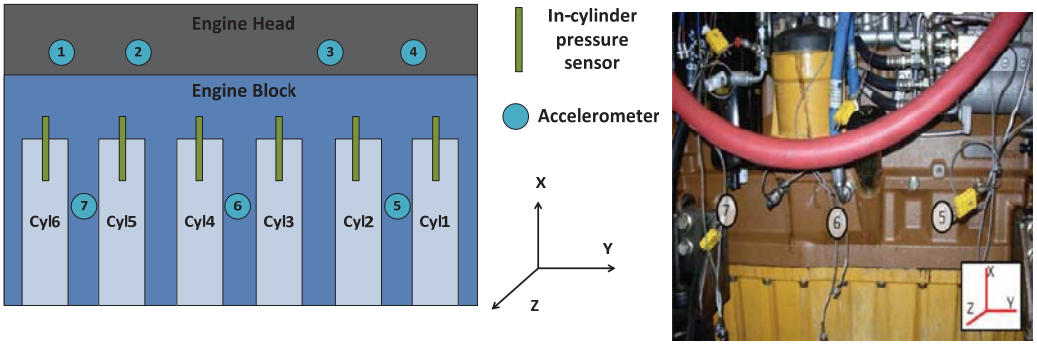

Figure 3.1: Sensor placement on 9L diesel engine

An operating condition of 2200RPM at both 725Nm and 1212Nm loads are taken as the example conditions to examine the FRF's robustness for load change. Also, SOI sweep was conducted for each load condition as the fuel efficiency and emissions are related with injection timing [76, 77]. Test condition details are shown in Table 3.2.

Table 3.2: Engine test conditions

Test condition	Engine Load (Nm)	Engine Speed (RPM)	Start of injection (DBTDC)	Injection duration (CAD)
1	725(60%)	2200	13.4	12.1
2	725(60%)	2200	13.4	12.3
3	725(60%)	2200	14.4	12.4
4	725(60%)	2200	15.4	12.0
5	1212(100%)	2200	12.0	22.1
6	1212(100%)	2200	13.5	21.7
7	1212(100%)	2200	15.4	21.1
8	1212(100%)	2200	16.9	21.4

3.2 Frequency response function

The frequency response function (FRF) quantifies the relationship between the input and the output spectrum in frequency domain by following equation 3.1 and is used to characterize the dynamic features of a system. As the objective of this work is to reconstruct the in-cylinder pressure (in cylinder 1) based on the measured accelerometer signal, the accelerometer signal is thus considered as the input and the in-cylinder pressure as the output. The FRF is then given as:

$$FRF = \frac{G_{a,p}}{G_{p,p}} \tag{3.1}$$

where the $G_{a,p}$ is the crosspower spectrum between the accelerometer signal and the in-cylinder pressure, $G_{p,p}$ represents the autopower spectrum of the in-cylinder pressure. Both $G_{a,p}$and $G_{p,p}$ are averaged through multiple cycles so as to eliminate the random noise.

To select the accelerometer location and channel which is used to compute the FRF and supply the accelerometer signal for in-cylinder pressure reconstruction, coherence analysis is employed. Coherence is a normalized measurement of linear dependence between two signals in frequency domain. With the range 0 - 1 quantifying the linear dependence, 1 represents the two signals are linear dependent and 0 indicates that the two signals are completely unrelated. When coherence falls to the scope between 0 and 1, noise is induced to the measurements of the two signals. If the coherence value is close to zero, the single-input and single-output model is deficient in modeling the system's dynamic features. Coherence is computed based on equation 3.2:

$$C_{p,a}(f) = \frac{|G_{p,a}(f)|^2}{G_{a,a}(f)G_{p,p}(f)} \tag{3.2}$$

where $C_{a,p}$ represents the coherence between the accelerometer signal and the in-cylinder pressure, and $G_{p,a}$ is the crosspower spectrum between the two signals. $G_{p,p}$ and $G_{a,a}$ are autopower spectrum of the in-cylinder pressure and the accelerometer signal respectively.

Morello [58] has shown that the frequency band of accelerometer signal that has strong linear dependency with in-cylinder pressure within the 0-2000 Hz frequency band on this engine. So for each accelerometer channel, the coherence is first averaged through 0-2000 Hz to be a single value for each test condition. Then these test condition dependent values are averaged to a new single value to ensure the coherence analysis takes into account all the test conditions. Figure 3.2 displays the coherence between the accelerometer signal acquired from each of the 21 channels and the in-cylinder pressure of cylinder 1. Channel 4x, 6z, 7x, and 7z are characterized with the coherence above 0.8 and 4x has the highest coherence at 0.85. So channel 4x is selected as the input channel of the single-input and single-output model to compute the FRF and supply the vibration signature to FRF for in-cylinder pressure reconstruction.

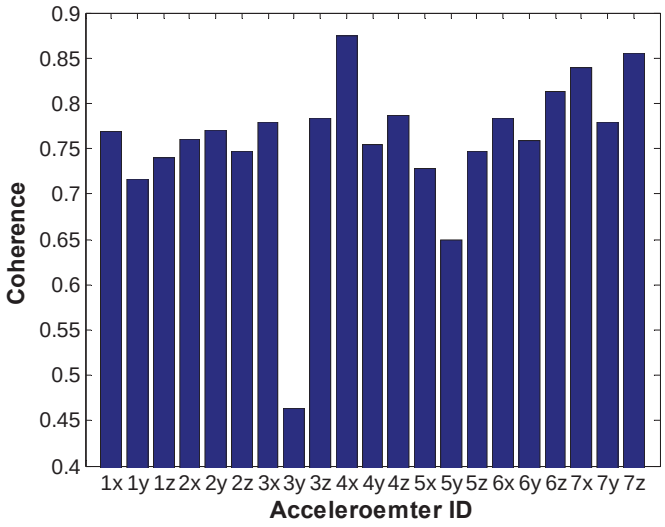

Figure 3.2: Coherence between in-cylinder pressure of cylinder 1 and accelerometer signals

Figure 3.3 illustrates the process for in-cylinder pressure reconstruction. FRF is first computed (equation 3.1) based on one test through accelerometer channel 4x. The time domain measured accelerometer signal from another test, named as objective test, is transformed to frequency domain linear spectrum by fast Fourier transform (FFT) and input to the obtained FRF. Then the estimated in-cylinder spectrum for the objective test in frequency domain is transformed back to time domain with inverse fast Fourier transform (IFFT) to achieve the time-based reconstructed in-cylinder pressure.

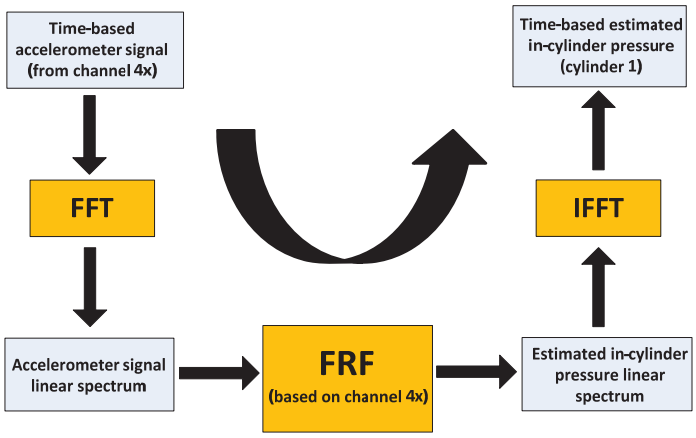

Figure 3.3: Process schematics for in-cylinder pressure reconstruction

To check the robustness of FRF acquired through channel 4x, the FRF computed based on Test 1 is applied to other test conditions (in Table 3.2) for the in-cylinder pressure reconstruction. The reconstructed in-cylinder pressure for each test condition is plotted in Figure 3.4, overlaid on the measured in-cylinder pressure. The estimated in-cylinder pressure for Test 2 has the best accuracy among all the tests. The amplitude error caused by the SOI change, which can be seen from Tests 2-4, is not as great as the error caused by the load change (Tests 5-8).

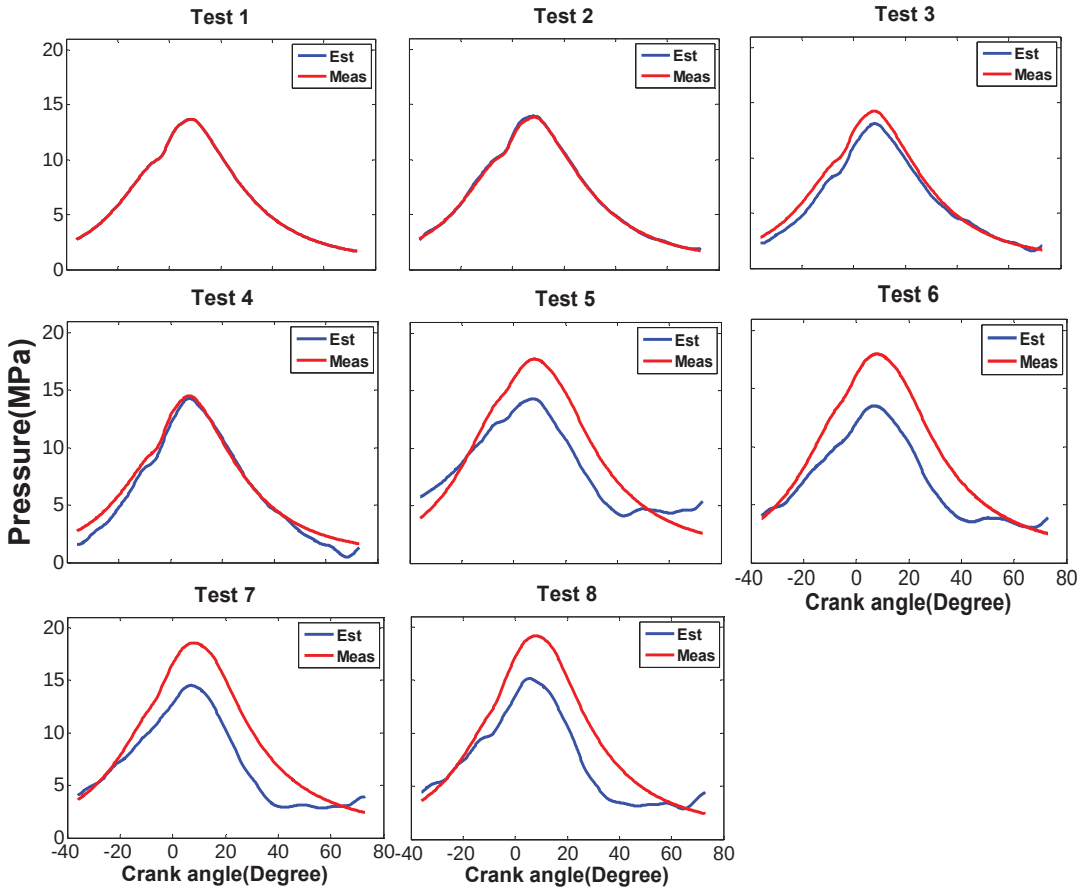

Figure 3.4: In-cylinder pressure reconstruction based on FRF from Test 1

To quantify the error between estimated and measured in-cylinder pressures, three parameters of in-cylinder pressures are used. Peak pressure crank angle location error

(PPCLE), in degree, is used to evaluate the combustion phasing accuracy. Peak pressure amplitude error (PPAE), and mean absolute pressure error (MAPE) are used to evaluate the amplitude accuracy of the reconstruction work. PPAE is normalized by the measured peak pressure amplitude (PPA) with the unit in %:

$$PPAE = \frac{|PPA_{est} - PPA_{meas}|}{PPA_{meas}} \tag{3.3}$$

MAPE, in MPa, is computed with equation 3.4, where N is the sample number of a windowed cycle from -36 degree to 72 degree, and i is the sample index.

$$MAPE = \frac{\sum_{i=1}^{N} |P_{est}^{i} - P_{meas}^{i}|}{N} \quad i = 1,2,\ldots.N \tag{3.4}$$

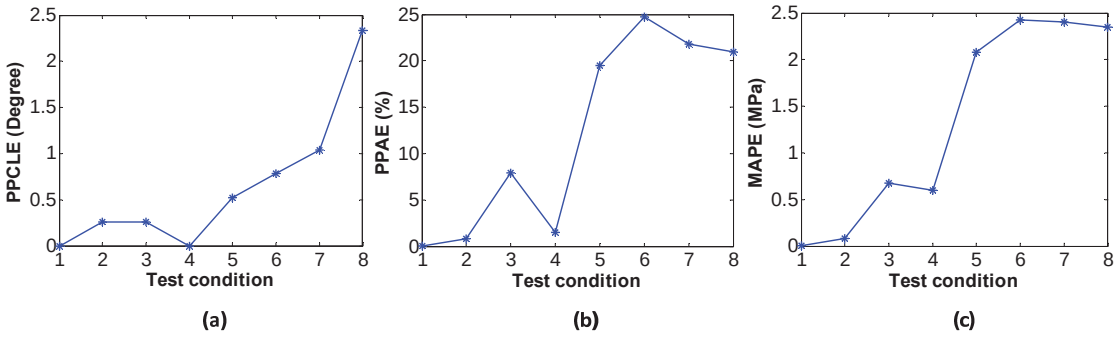

Figure 3.5: Reconstruction results evaluation based on PPCLE, PPAE, and MAPE

Figure 3.5 shows the three errors, PPCLE, PPAE, and MAPE, between the measured in-cylinder pressure and the in-cylinder pressure reconstructed with FRF obtained from Test 1. When the FRF computed based on Test 1 is applied to Test 1 itself for in-cylinder pressure reconstruction, the errors of the three pressure parameters are all zeros. As there is only 0.2 degree injection timing difference between Test 1 and Test 2 with speed, load, and SOI the same, the errors of the in-cylinder pressure reconstruction for Test 2 are: PPCLE= 0.3 degree, PPAE=0.8%, and MAPE=0.08 MPa, which are the lowest among all the test conditions. At low load SOI sweep conditions, less than 0.4 degree PPCLE is introduced due to the SOI change. Meanwhile, SOI change can lead to the PPAE change as great as 8% and MAPE change as great as 0.7MPa. When condition changes to high

load, more errors are induced. This can be seen in Figures 3.4 and 3.5 (Tests 5 to 8). PPCLE reaches the maximum, 2.3 degree, at Test 8. PPAE maintains above 20% for high load tests with 25% at Test 6 being the maximum. MAPE are all above 2MPa with the maximum close to 2.5 MPa at Test 6. So the conclusion can be drawn that the accuracy of the in-cylinder pressure reconstruction deteriorates when SOI or load changes especially when the load changes. The FRF robustness is just limited to similar test conditions.

As the FRF computed based on one test condition does not possess the capability to adapt to test conditions with SOI and load changes, further work in this study is to improve the in-cylinder pressure reconstruction accuracy by promoting the robustness of the FRF. As shown in Figure 3.6, an adaptation block, which is used to adapt the obtained FRF, is plugged into the reconstruction process before the FRF is applied for the in-cylinder reconstruction.

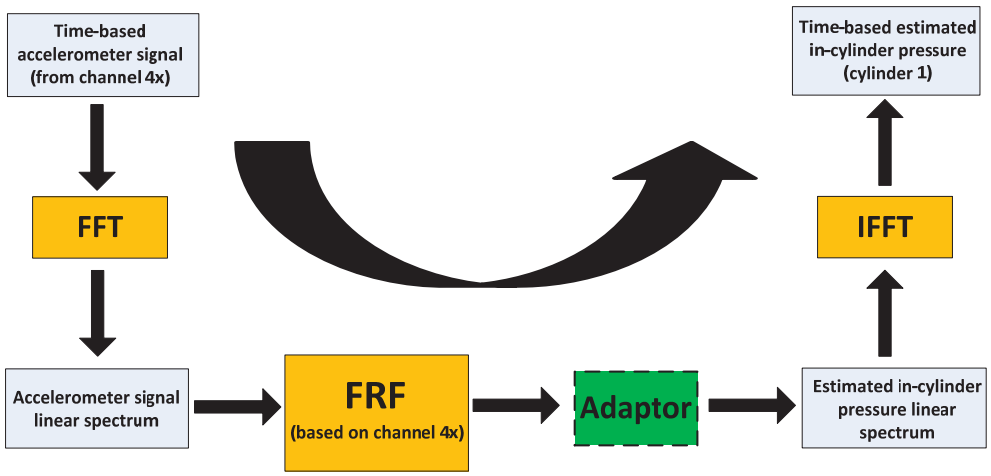

Figure 3.6: Process schematics for in-cylinder pressure reconstruction with the adaptor added

3.3 Adaptation of frequency response function

With the sample frequency at 51200Hz, the -36 to 72 degree window at 2200RPM contains 423 samples. So it seems that the adaptation process has to handle the 213 harmonics (FRF is symmetrical along the Nyquist frequency) of FRF to make it work for

other test conditions. However, further observation based on the FFT plot of in-cylinder pressure shows that the number of FRF harmonics the adaptation process needs to deal with can be reduced. Figure 3.7 shows the FRF amplitude and the in-cylinder pressure FFT content.

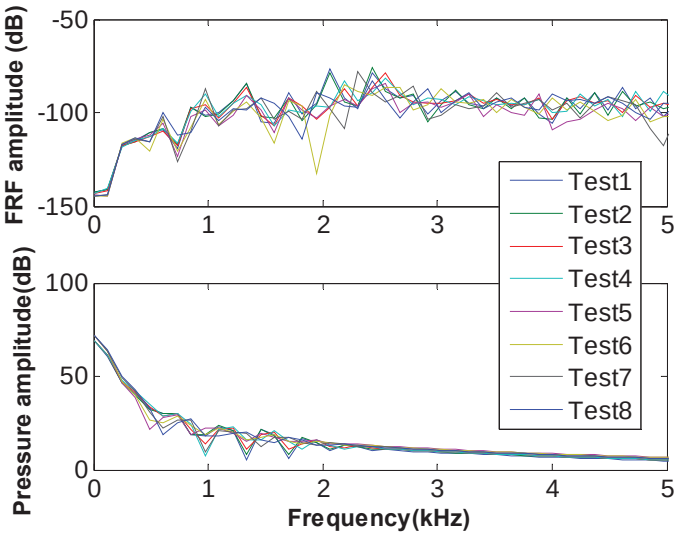

Figure 3.7: FRF amplitude (top) and FFT content of in-cylinder pressure (bottom)

The main FFT content of in-cylinder pressure concentrates at low frequency band, definitely lower than 2 kHz. So only the low frequency harmonics need to be adapted to make FRF robust. For the frequency band higher than 2 kHz, FRF is relating the noise parts of the two signals. To figure out exactly how many harmonics of FRF in the low frequency band are determinant for in-cylinder pressure reconstruction, an examination procedure is implemented. First, the FRF computed based on Test 1 is taken as the base FRF. The first to the *n*th successive harmonics of the base FRF are replaced with the corresponding harmonics of the FRF computed from another test condition, named as objective condition. Then, the new FRF is applied to reconstruct the in-cylinder pressure for this objective condition. Evaluation of the performance of new FRF relative to the number of harmonics replaced based on the three pressure parameter errors, PPCEL, PPAE, and MAPE, is given in Figure 3.8. Table 3.3 gives the frequency values for the first 10 sequential harmonics with the sampling frequency at 51.2 kHz.

Table 3.3: Frequency location for FRF harmonics

Harmonic sequence	1st	2nd	3rd	4th	5th	6th	7th	8th	9th	10th
Frequency (Hz)	0	121	242	363	484	605	726	847	968	1089

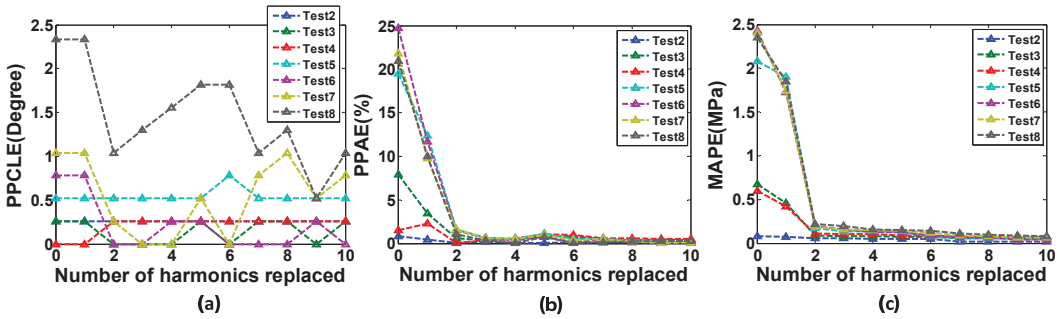

Figure 3.8: Estimation errors with FRF harmonics of Test 1 corrected

For PPCLE in Figure 3.8 (a), when the first 2 harmonics of FRF are replaced, an error drop can be seen for Test 3, Test 6, Test 7, and Test 8. No obvious drop is seen when more than 2 harmonics are replaced except for Test 8, where the error decreases when 7 and 9 harmonics are replaced. With respect to PPAE and MAPE, the most dominant decreases of the errors occur when the first two harmonics are replaced. When more than two and up to ten harmonics are replaced, PPAE maintains stable with error decrease as small as 5% of the error decrease that is due to the replacement of the first two FRF harmonics. MAPE follows the similar trend with PPAE when more than the first two harmonics are replaced. The error decrease of 0.15 MPa with the other eight more harmonics replaced is just 6% of the error decrease due to the first two harmonics replacement for Test6, Test7, and Test8.

So the first two harmonics should play the most important role in FRF adaptation process. Although more harmonics adapted will lead to a reconstruction result with higher accuracy, the increased cost of computation makes the adaptation inclined to work on the first two, 0Hz and 121Hz, harmonics.

The first harmonic of FRF which locates at 0 Hz represents the ratio between the offset of accelerometer signal and the offset of in-cylinder pressure. Figure 3.9 displays the in-cylinder pressure offsets for 40 tests. The first 20 tests are at 2200RPM/725Nm, the second 20 tests are at 2200/1212Nm. The 20 tests at each load condition are not repeated but distinguished by start of injection and injection duration. The maximum offset differences for the tests at the same load condition are: 0.21MPa at 725NM and 0.24MPa at 1212Nm. The maximum offset differences normalized by the mean offset value at corresponding load condition are 2.5% at 725NM and 3% at 1212NM respectively. So the offsets of in-cylinder pressure for 2200RPM conditions with the same load are close to one another. In this study, the in-cylinder pressure offsets of the two load conditions are taken as constants and computed by averaging the offsets of the 20 tests for each load. The offsets of in-cylinder pressure within -36 - 72DATDC for 2200RPM/725Nm and 2200RPM/1212Nm conditions are determined as 6.8MPa and 9.4MPa respectively.

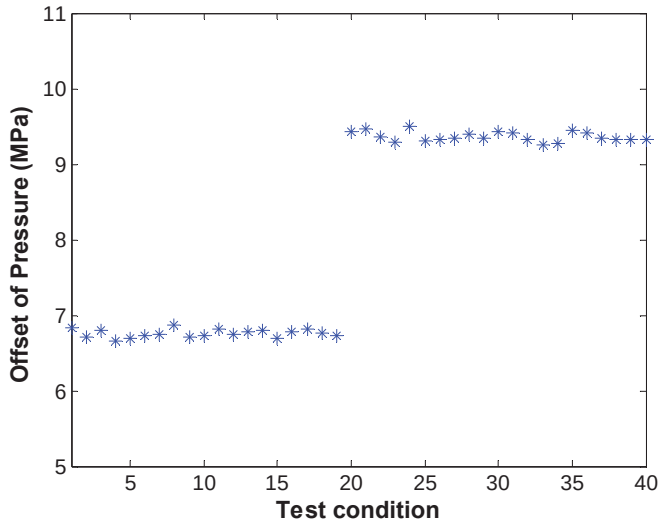

Figure 3.9: Offsets of in-cylinder pressure for tests at 2200RPM/725Nm and 2200RPM/1212Nm

With the offset of measured accelerometer signal within -36 - 72DATDC computed, the 0Hz harmonic of FRF can be estimated by equation 3.5:

$$FRF_{0Hz} = \frac{Offset_{Accel}}{Offset_{Pressure}} \tag{3.5}$$

The estimated 0Hz FRF harmonic relative to test conditions are shown in Figure 3.10. The estimated 0Hz harmonic of FRF is close to the measured one with the greatest error at 9.8e-9 from Test 7. Such an error normalized by the measured 0Hz harmonic of FRF at Test 7 is 1%.

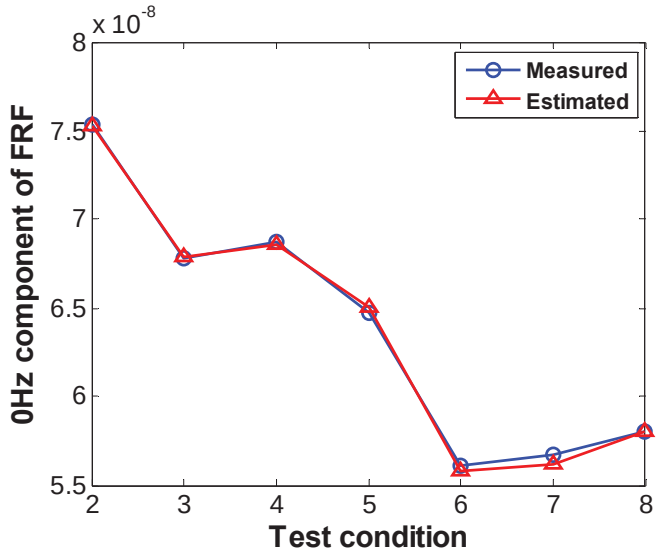

Figure 3.10: Estimated 0Hz harmonic of FRF

The 0Hz harmonic of FRF at each test can be estimated based on the on-line measured accelerometer signal offset, and the pre-measured in-cylinder pressure offset. As the test-condition-dependent in-cylinder pressure offset is considered similar between different engine structures of the same type, the pre-measurement of in-cylinder pressure offsets can be performed on one engine and these offsets can be applied to the other engines.

Next, the second harmonic of FRF which locates at 121Hz needs to be adapted. Figure 3.11 shows the 2nd harmonics of FRFs in complex plane for the 8 conditions (Table 3.2). As the FRF computed from Test 1 is taken as the base FRF, the adaptation will start from the original position marked by a triangle and end up at the distinctive positions corresponding to other test conditions marked by asterisks.

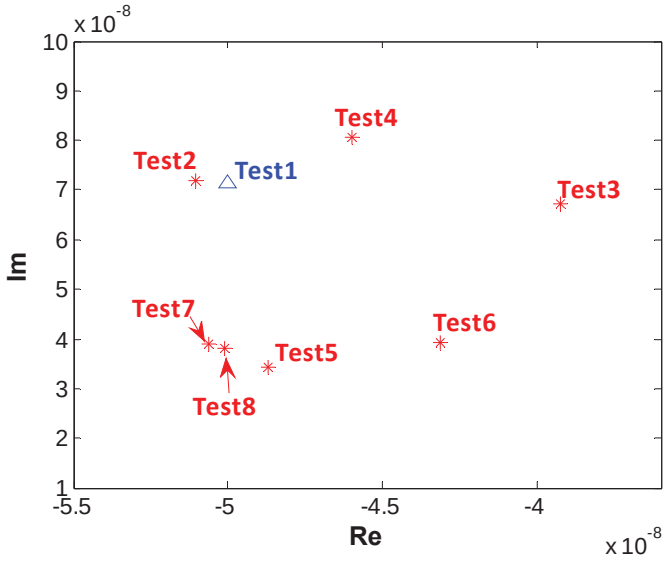

Figure 3.11: 121Hz harmonic of FRF for each test condition

To find the optimal 2nd harmonic position in the complex domain for each test condition, the population-based optimization method is utilized. The population-based optimization approach through competition and cooperation among the population can often find the optimal solution effectively and efficiently [78]. Particle swarm optimization (PSO), as one of the population-based optimization approaches, is a computational method that seeks the optimal solution of a problem with iterative improvement of candidate solutions with the goal of minimizing the objective function. Each of the candidate solutions, named as particle, moves around the M-dimension search-space and towards better solution area with the velocity adjusted according to its own moving experience and its companions' moving experience. M represents the number of variables that involved in the optimization process. The position of the *i*th particle is defined with $X_i = (x_{i1}, x_{i2}, ...x_{iM})$. The best previous position of the *i*th particle, which is locally best, is defined as $P_i = (p_{i1,}\, p_{i2}, ...p_{iM})$. The index for the globally best particle among all the particles is represented with *g*. The locally best position is updated according to personal moving experience. The globally best position is updated based on all the particles' moving experience. The velocity for *i*th particle is defined by $V_i = (v_{i1}, v_{i2}, ...v_{iM})$. The particles are organized with the following equation:

$$v_{im}^{k+1} = wv_{im}^{k} + c_1 r_1^k \left(p_{im}^k - x_{im}^k\right) + c_2 r_2^k \left(p_{gm}^k - x_{im}^k\right); \quad (3.6a)$$

$$x_{im}^{k+1} = x_{im}^k + v_{im}^{k+1} \quad (3.6b)$$

k represents the kth iteration. w is the initial weight. A greater w will promote a global search while a small w will promote a local search [78]. In his chapter, a linearly decreasing w at range [1,0.3] is utilized through the PSO run to make the initial searches more global while the searches near the end more local. c1 and c2 are two positive constants, which are fixed at 1.05. r1 and r2 are random fractions in range [0,1]. M equals 2 because both the real and imaginary parts of the 2nd harmonic of FRF need to be adapted. The search-space is confined within -10e-8 to -1e-8 for real axis and 0.5e-8 to 15e-8 for imaginary axis with the 2nd harmonic of FRF of Test 1 near the center of the search-space. The initial positions for the particle population are randomly fixed in the search-space. The initial velocity is defined depending on its projection on each axis, named as projected velocity. The projected velocity is randomly fixed between 0 and 1/4 of the length that has been confined on each axis.

To update p_{im} and p_{gm} for each iteration, an objective function is needed as a standard to figure out the locally best and globally best position. For the compression stroke and expansion stroke, the in-cylinder pressure and cylinder volume can be formulated with the following equation [14]:

$$PV^{\gamma} = constant \quad (3.7)$$

Figure 3.12 shows the LogP-LogV plot for the 8 tests. Although the condition parameters are different from one another, all of them share the identical γ, which is the ratio of specific heats, for compression stroke and expansion stroke where $\gamma_{comp} = 1.25$ and $\gamma_{expan} = 1.16$.

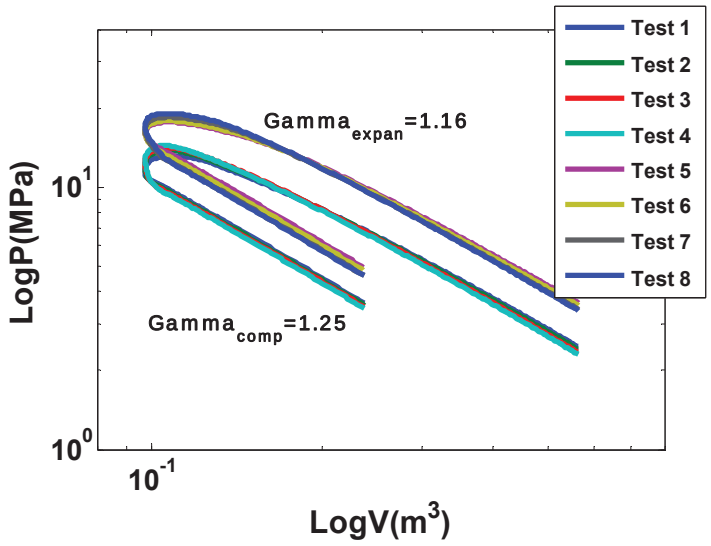

Figure 3.12: LogP-LogV plot

An objective function that incorporates both γ_{comp} and γ_{expan} is created:

$$Z = \left|0.5 * \left(\gamma_{comp}^{k} + \gamma_{expan}^{k}\right) - 1.22\right| \tag{3.8}$$

k represents the *k*th iteration. p_{im}^{k} and p_{gm}^{k} will be updated if the objective function can be further minimized at the *k*th iteration. This objective function actually linearly combines two objective functions into one [79]. The final adapted value of the 2nd harmonic of FRF for each test condition is composed in the form of $p_{g1}^{k} + p_{g2}^{k} i$.

3.4 Results

The designed adaptor, which adapts the FRF to make it work for other tests with different condition parameters, is expected to be implemented with least computation consumption. So a compromise needs to be determined between the computation cost and the performance of the adaptor. Generally, when a greater number of population and iteration is employed, the optimization result will be further improved [78, 80, &81]. However, the time for computation will increase accordingly. Table 3.4 lists the changes of the three in-cylinder pressure parameter errors relative to the population number and the iteration number. The most remarkable improvements of the three in-cylinder pressure parameters,

as shown in Table 3.4, occur when iteration number increases from 5 to 10 with the population number at 10. The reductions of the errors are: 0.5 degree PPCLE, 3% PPAE, and 0.4MPa MAPE. With the further increase of both population and iteration numbers, the three parameter errors maintain stable with PPCLE at 0.8 degree, PPAE at 1%, and MAPE at 0.2 or 0.3 MPa. Therefore, the population number and iteration number are determined as 10 and 10 respectively. In equation 3.6, $i = 1,2,3, \dots 10$ and $k = 1,2,3, \dots 10$. The primary reason why the increased computation cost does not bring about an improved estimation result is due to the cost function definition. If another cost function defined based on the three pressure parameters can be found, the errors will be definitely decreased by following the process of minimizing the cost function. On the other hand, the adaptation of only two FRF harmonics cannot result in the further reduction of the three in-cylinder pressure parameter errors which depends on the adaptation of more than two FRF harmonics.

Table 3.4: Mean errors relative to population and iteration of PSO algorithm

Population	**Iteration**	**Results**		
		PPCLE (Degree)	**PPAE** (%)	**MAPE** (MPa)
10	5	1.3	4	0.7
	10	0.8	1	0.3
	15	0.8	1	0.2
	20	0.8	1	0.2
20	5	0.8	1	0.3
	10	0.8	1	0.3
	15	0.8	1	0.3
	20	0.8	1	0.2
30	5	0.8	1	0.2
	10	0.8	1	0.2
	15	0.8	1	0.3
	20	0.8	1	0.2

Figure 3.13 compares the 2nd harmonics of the measured FRFs and the reconstructed 2nd harmonics which are obtained based on the adaptation of the 2nd harmonic of the base FRF (Test 1). The reconstructed and the measured ones don't coincide. However, if all of

them are connected following the test condition sequence, the test-to-test relative positions are similar between measured and reconstructed cases except for Test 8.

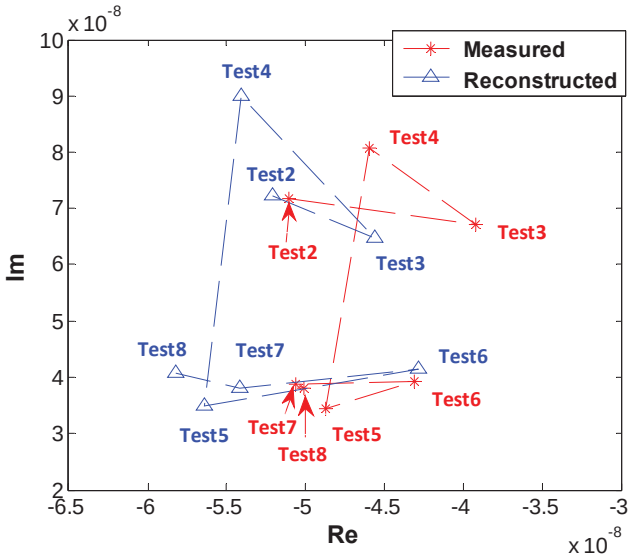

Figure 3.13: Reconstructed 121Hz-harmonics of FRF

With the adaptor worked on the 0Hz harmonics, and the 121Hz-harmonics of base FRF (computed from Test 1) by following the procedures described above, in-cylinder pressure is reconstructed by inputting the adapted FRF into equation 3.2. Figure 3.14 shows the reconstructed in-cylinder pressure overlaid upon the measured one for each test. In comparison to Figure 3.4, the reconstructed in-cylinder pressures based on the adapted FRF match the measured ones better based on visual assessment. The most obvious improvements occur for high load SOI sweep tests where the amplitude of reconstructed in-cylinder pressure is closer to the measured one. The evaluation of the performance of adapted FRF on the basis of PPCLE, PPAE, and MAPE, is given in Figure 3.15 by comparing to the errors of the base-FRF case. For PPCLE, all the errors of the 8 tests for adapted FRF are below 1 degree and the greatest PPCLE improvement of 1.3 degree occurs at Test 8. PPAE is retained lower than 3% with PPAE at high load tests improved over 90% (normalized by base-FRF PPAE). MAPE is maintained below 1.5MPa across all the tests. The most evident improvements of MAPE also occur for high load tests with the average improvement at high loads at 75% (normalized by base-FRF MAPE).

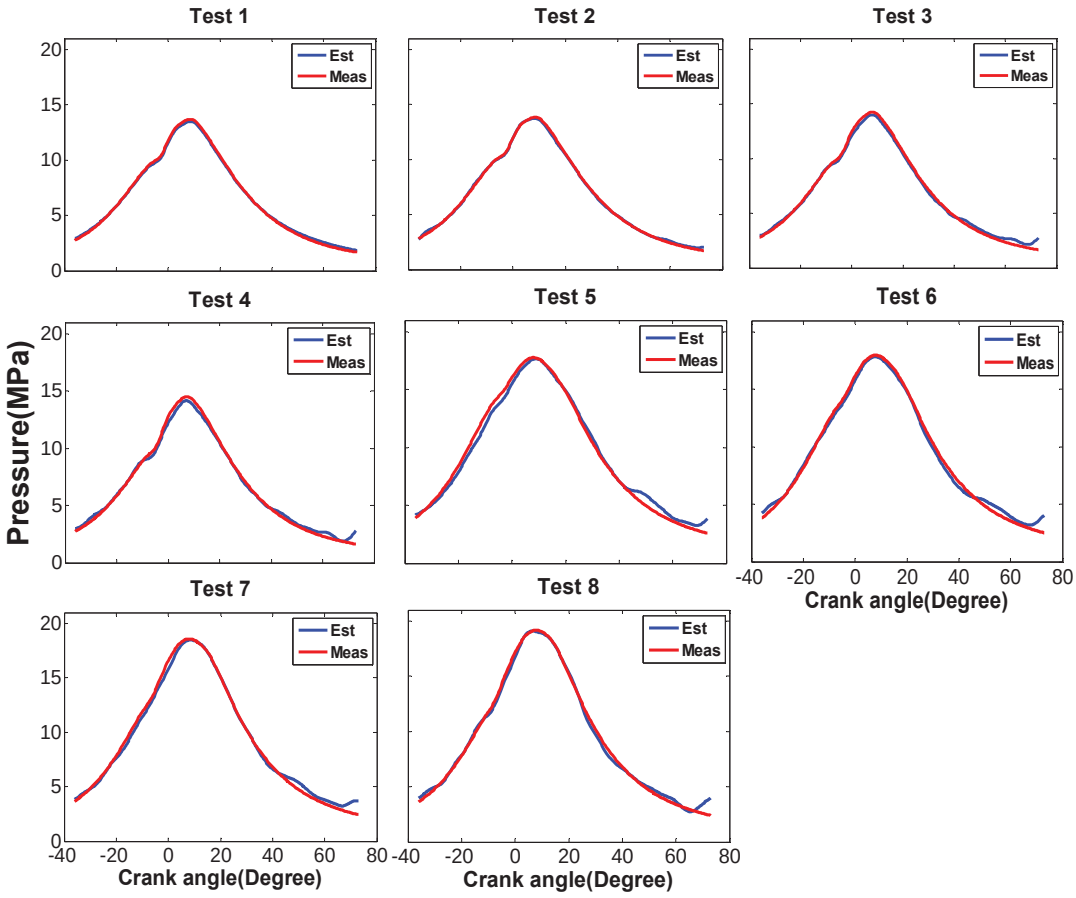

Figure 3.14: In-cylinder pressure reconstruction results based on adapted FRF

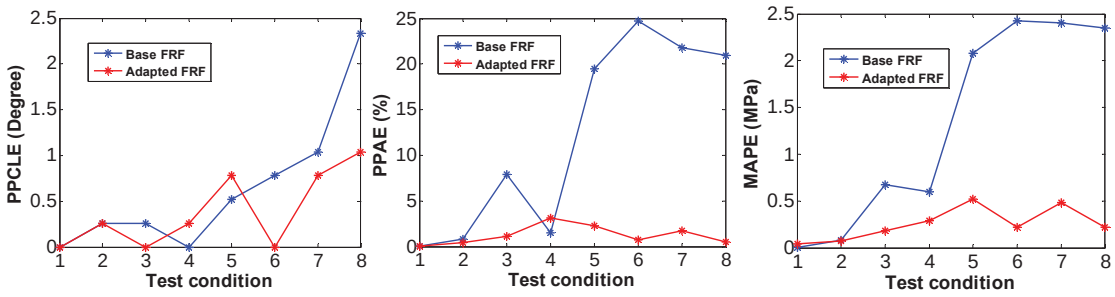

Figure 3.15: Reconstruction results evaluation based on PPCL, PPA, and MAPE

3.5 Summary and conclusion

The results of this study show that the adapted FRF, in comparison to the unadapted FRF, can result in an improvement of the in-cylinder pressure reconstruction for the tests with SOI and load variations. The results of the research in this chapter are as follows:

- The FRF that used to model the relationship between the in-cylinder pressure and accelerometer signal varies with load change and SOI change. So the FRF computed from one condition needs to be adapted so as to reconstruct the in-cylinder pressure for other test conditions with load or SOI changes.

- Results show that the adaptation of 0Hz and 121Hz harmonics of FRF leads to the greatest improvement for in-cylinder pressure reconstruction with the standard setup by PPCLE, PPAE, and MAPE. So the adaptation process in this study focuses on the first two harmonics of FRF.

- 0Hz harmonic of FRF can be predicted for each test condition with the offset of the premeasured in-cylinder pressure and offset of accelerometer signal measured on-line.

- PSO works to adapt the 121Hz harmonic of FRF with the objective function created by incorporating the ratio of specific heats of both compression and expansion strokes.

- In-cylinder pressure reconstruction performance is improved with the 0Hz and 121Hz harmonics of FRF adapted. In comparison to the results obtained based on the unadapted FRF, the PPCLE is improved as great as 1.3 degree, the improvements for PPAE are all above 90%, and the averaged MAPE improvement is 75%.

Chapter 4

Application of FRF with SISO and MISO models[5]

In this chapter, the work focused on the comparison of frequency response function applications for accelerometer-based in-cylinder pressure reconstruction between SISO and MISO models. Frequency response function was used to quantify the relationship between the input and the output for each model. The accelerometer signals were taken as the inputs and in-cylinder pressure as the output. For the SISO model, the single input was acquired through the accelerometer channel that was proved optimal for data acquisition via coherence analysis. With respect to the MISO model, the accelerometer signals from multiple channels were utilized as the inputs and the channel-based FRFs were computed. Then, the in-cylinder pressures were reconstructed from the obtained FRFs. Principal Component Analysis (PCA) was employed to extract the common features from the estimated in-cylinder pressures so as to supply an optimized pressure trace. The shape of the estimated in-cylinder pressure was improved after implementing the PCA method. However, offset of the estimated in-cylinder pressure still needs to be compensated. The reason why FRF introduces great offset error to the in-cylinder pressure reconstruction is that a low coherence between the in-cylinder pressure and the accelerometer signal resides within the lowest frequency band. The low coherence exists in the lowest frequency band has been demonstrated in Johnsson's work [68]. This

[5] The material contained in this chapter was submitted to "Proceedings of the Institution of Mechanical Engineers, Part C: Journal of Mechanical Engineering Science" and the current status is "Peer review in process".

feature, as a drawback of FRF application, introduces considerable errors to both the shape and especially the offset reconstruction of the in-cylinder pressure. The offset error was successfully compensated in this chapter based on the deviation of adiabatic equation in the compression engine stroke. However, the correct offset error compensation needs the shape of the in-cylinder pressure to be accurately estimated first. After compensating the offset of the optimized in-cylinder pressure, the final estimated in-cylinder pressure was achieved. With the concern of reducing the cost for the accelerometer usage and mounting, a procedure that seeks the minimum number of input channels which does not deteriorate the reconstruction accuracy was presented.

4.1 **SISO model**

Most researchers follow the SISO model for combustion metrics reconstruction with the vibration signature acquired from one single channel [56, 57, 49, 60, &68]. Similarly on the 9L engine, the FRF between the in-cylinder pressure from cylinder 1 and the accelerometer signal from one selected channel is first applied for in-cylinder pressure estimation. To evaluate the FRF's robustness, FRF computed based on test condition #4 is utilized to reconstruct the in-cylinder pressure for all the test conditions listed in Table 3.2.

As seven triaxial accelerometers mounted on the engine structure are acquiring the acceleration data simultaneously, a selection procedure that picks out one optimal channel to supply the input for SISO model should be considered.

Johnsson [68] and Chiavola et al. [52] have proved the frequency dependent linear dependency between accelerometer signal and in-cylinder pressure with coherence analysis on two different engine structures. Coherence is a frequency dependent normalized measurement of linear relationship between the input and the corresponding output signal. It ranges from 0 to 1 with 0 indicating no relationship and 1 indicating outstanding linear dependency between the input and output signals. The coherence computation is based on equation 4.1 where G is the power spectrum with respect to its

subscripts and *C* is the coherence. In this work, the $G_{a,p}$ represents the crosspower between the accelerometer signal and the in-cylinder pressure, $G_{p,p}$is the autopower of the in-cylinder pressure, and $G_{a,a}$is the autopower of the accelerometer signal.

$$C_{p,a}(f) = \frac{|G_{a,p}(f)|^2}{G_{p,p}(f)G_{a,a}(f)} \tag{4.1}$$

When coherence drops to the value lower than 1 but greater than 0, it indicates that the noise enters the measurement of either input or output signals, or the accelerometer signal corresponds not only to the in-cylinder pressure but some other part movement like the valve movement. The vibration signal from the optimal input channel is expected to relate to in-cylinder pressure rather than other momentum. Also, a low noise introduction to the accelerometer signal is preferred. So the coherence between the in-cylinder pressure and the accelerometer signal that is closest to 1 will be utilized as the standard to select the optimal input channel.

Figure 4.1 illustrates the frequency content of in-cylinder pressure's fast Fourier transform (FFT) result and the coherence between the in-cylinder pressure and the accelerometer signals where x and z represent the orientations of accelerometers as shown in Figure 3.1. Coherence that has been averaged through 700 cycles within the 0-2000Hz band is high and an obvious coherence amplitude drop can be seen at the frequency of 2000Hz and higher. The most dominant component of pressure FFT content locates within the 0-1000Hz band.

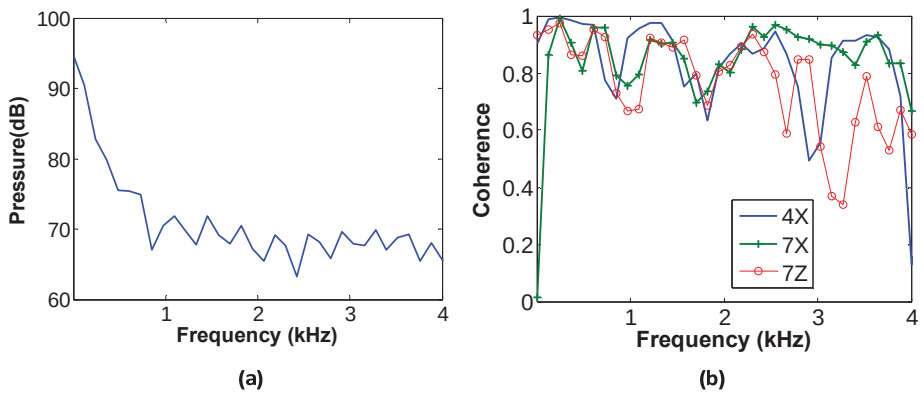

Figure 4.1: FFT content of in-cylinder pressure (a) and Coherence between in-cylinder pressure and engine structure vibration (b)

So the 0-1000Hz is initially determined to be the frequency band based on which the further work will proceed. However, as displayed by Figure 4.2, the low pass filter with cut-off frequency at 1000Hz makes the filtered pressure lose some dynamic features around 0 crank angle degree (CAD) where a sharp pressure increase can be seen on the full bandwidth (full BW) in-cylinder pressure. Also, the peak of filtered pressure just reaches the valleys of the peak magnitude oscillation of the full bandwidth in-cylinder pressure. In comparison, the low pass filter with cut-off frequency at 2000Hz leads to a better filtered result with respect to both the pressure peak and the pressure change around 0 CAD. As shown in Figure 4.1(b), the coherence drops to a much lower value for the frequency higher than 2000Hz when no low pass filter is applied. This can be demonstrated by the coherence of 0.3 at 3000Hz for channel 7Z. Therefore, the cutoff frequency is fixed at 2000Hz. The in-cylinder pressures discussed in the following sections are all filtered by the Kaiser low-pass filter with cut-off frequency at 2 kHz. Also, a window with the length of 108 degrees starting from -36 to 72 degrees is applied to both accelerometer signal and in-cylinder pressure with respect to each cycle in each cylinder. Some of the figures in this chapter have a crank angle range of -30 to 60 degrees to zoom it for observation convenience as shown in Figure 4.2.

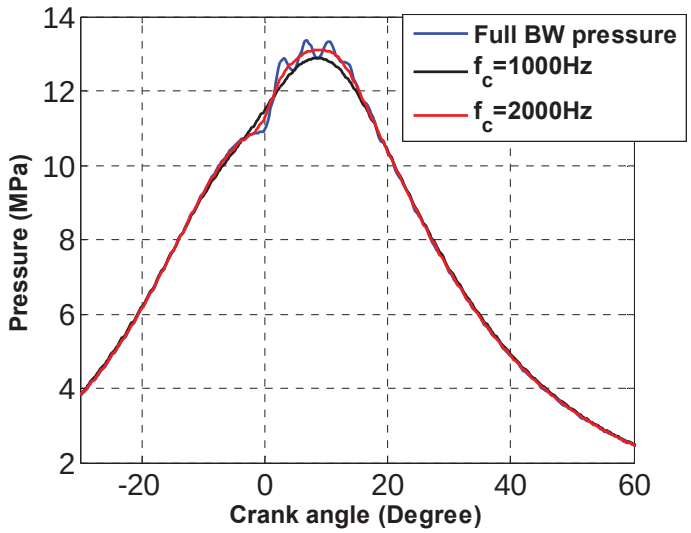

Figure 4.2: In-cylinder pressure filtered by low-pass filter

As the frequency band is narrowed to 0-2kHz from 0-25.6kHz, the coherence within 0-2kHz is averaged into one single value for each test condition to feature the linear dependency between the in-cylinder pressure and the accelerometer signal. Then, these test-condition-dependent coherence values are averaged into one single value to ensure the coherence analysis is on the basis of all the conducted test conditions. Figure 4.3 indicates the coherence between the in-cylinder pressure from each cylinder and the accelerometer signal from each accelerometer channel.

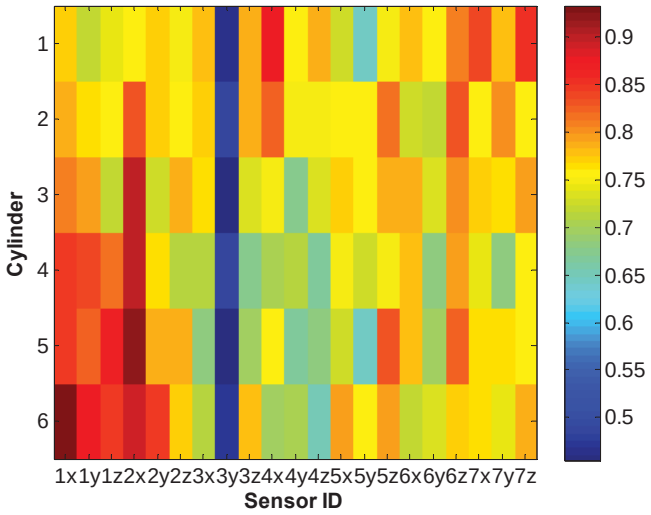

Figure 4.3: Coherence between in-cylinder pressure and accelerometer signals

In Figure 4.3, from cylinder 1 to cylinder 6, the channels characterized with the highest coherence are respectively 4x, 2x or 6z, 2x, 2x, 2x, and 1x. Channels 1x and 2x have high coherence with the pressure of cylinder 6 and cylinder 5 respectively because accelerometers 1 and 2 are placed closest to the two cylinders on the engine head. Similarly for cylinder 1 and cylinder 2, channels 4x and 3x are expected to have high coherence with the two cylinder pressure signals respectively due to the closeness of the accelerometer placement (Figure 3.1). However, the coherence is much lower than cylinder 5(2x) and cylinder 6(1x). The possible reason could be more noise not correlated with the in-cylinder pressure was introduced to the two accelerometer channels. Channel 3y has a consistently low coherence below 0.55 for all six cylinders. The reason could be the noise not correlated with in-cylinder pressure is induced to channel 3y and becomes dominant. Or channel 3y or the cable might be damaged. It is unlikely due to the accelerometer mounting process as the other two orientations x and z have coherence around 0.8 for cylinder 1.

The channel which is characterized by higher coherence with in-cylinder pressure can result in a more accurate in-cylinder pressure reconstruction. As the study in this chapter takes the reconstruction of in-cylinder pressure from cylinder 1 as the objective, channel

4x is chosen as the optimal accelerometer for the SISO model. So for SISO model, FRF is computed through channel 4x based on equation 4.2. Both $G_{a,p}$and $G_{p,p}$ are averaged through all the cycles under one test condition so that the random noise can be reduced.

$$FRF = \frac{G_{a,p}}{G_{p,p}} \tag{4.2}$$

To check the FRF's robustness, the FRF computed from Test 4 through channel 4x is applied to reconstruct the in-cylinder pressures for all the test conditions listed in Table 3.2. Figure 4.4 shows the results of in-cylinder pressure reconstruction for each test.

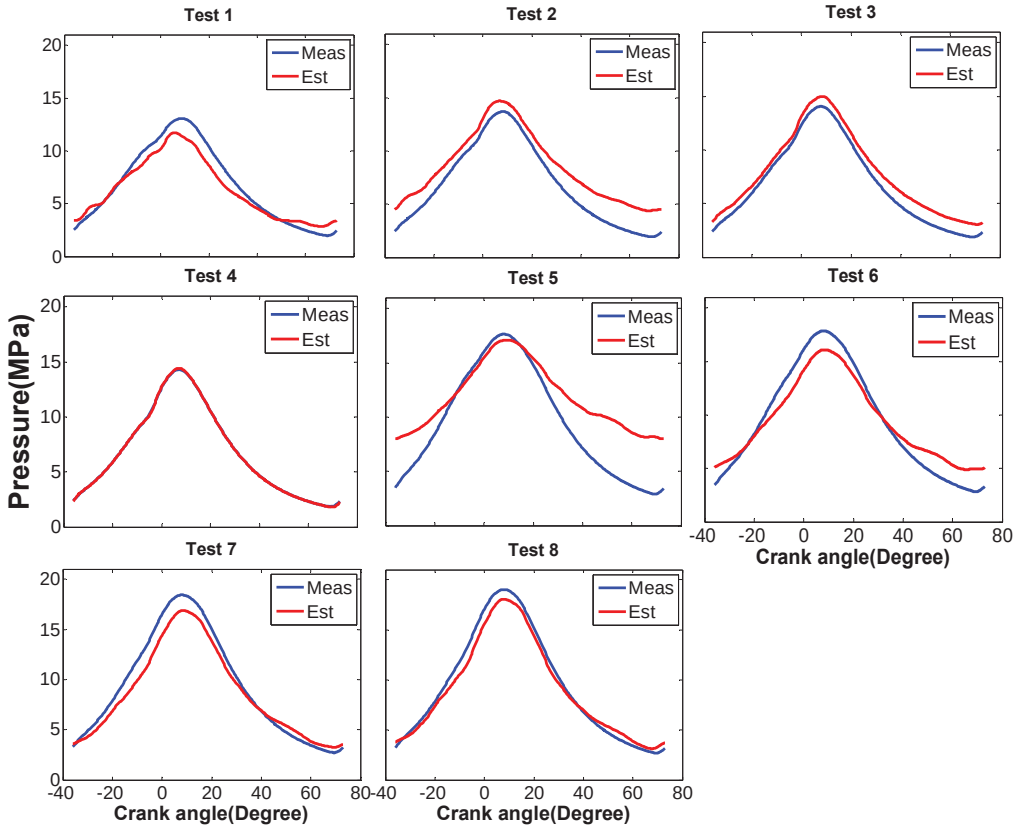

Figure 4.4: In-cylinder pressure reconstruction results for cylinder 1 with SISO model by applying the FRF from Test 4 through channel 4x

Except for Test 4, errors can be observed when the SOI or load condition changes. For low load SOI sweep conditions, offset difference is dominant for Test 2 and Test 3. For Test1, a distinct shape difference appears. For high load SOI sweep conditions, shape

difference is dominant and especially obvious for Test 5. It can be concluded that the FRF based on SISO model does not show adequate robustness in in-cylinder pressure reconstruction for test conditions with SOI and load variations. The quantified errors will be given and compared with the errors based on MISO model in the following section.

4.2 MISO model

The SISO-model-based FRF, computed based on a known test condition through the optimal input acquisition channel, is deficient in modeling the relationship between the in-cylinder pressure and the accelerometer signal when the load or SOI parameter changes. To comprehensively model the system dynamics in a structure, a multiple-input and multiple-output model (MIMO) is needed [82, 83]. The engine structure is a complex system with both combustion related energy including in-cylinder pressure and mechanical energy including valve movement and piston slaps as outputs. However, as the in-cylinder pressure can thoroughly reflect the combustion process and thus supply feedback for combustion control, the MIMO model that aims for dynamic feature identification is simplified into a MISO model with the in-cylinder pressure as the single output and the other outputs as the noise. As the objective of the study is to reconstruct the combustion metrics based on accelerometer signals, accelerometer signals are taken as the inputs. The MISO model is evaluated based on the same test conditions which have been used to evaluate the SISO model. Initially, all the 21 channels are utilized as the input channels and 21 independent FRFs are obtained to connect the in-cylinder pressure with these accelerometer signals. To evaluate the FRFs' robustness, the FRFs obtained from one test condition are applied to reconstruct the in-cylinder pressures for all the test conditions given in Table 3.2. By following equation 4.2, 21 FRFs are computed based on Test 4. When the accelerometer signals acquired from the 21 channels for any other test condition are input into the fixed FRFs, 21 estimated in-cylinder pressures will be output. Figure 4.5 displays this process and Figure 4.6 illustrates the 21 estimated in-cylinder pressures for Test 1.

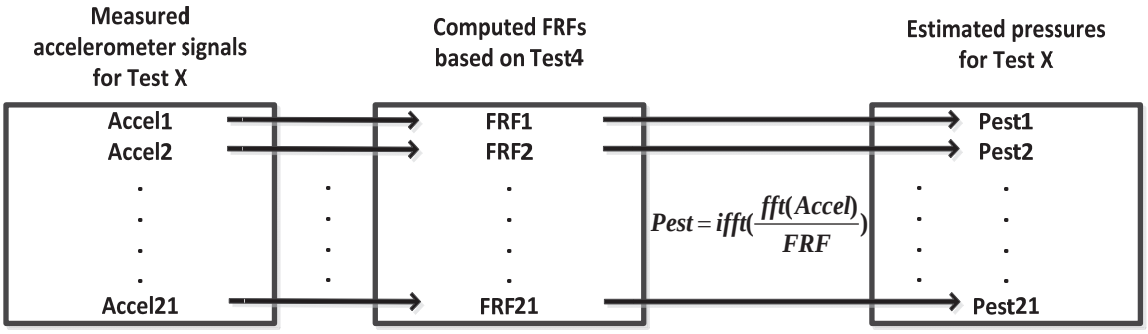

Figure 4.5: Process for in-cylinder pressure reconstruction with accelerometer signals from multiple channels

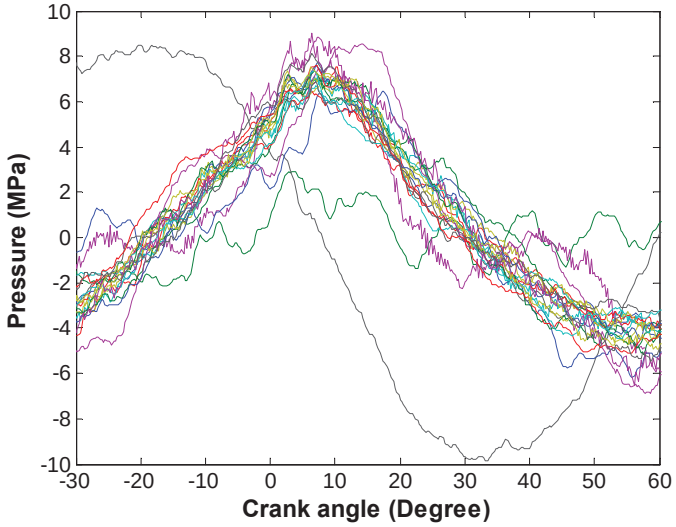

Figure 4.6: In-cylinder pressures reconstructed from 21 channels, Test1

After removing the offset (Figure 4.6), some of the 21 estimated pressure traces look noisy and the shapes of the 21 estimated pressure traces are different from one another. Although the single input channel does not possess adequate reliability for in-cylinder pressure reconstruction, the combination or interaction of the estimation results from all of or some of the input channels might lead to an improved result. Principal component analysis is employed to extract the shared and most dominant features in all the 21 reconstructed in-cylinder pressures, because it is believed that the estimated pressure

based on each accelerometer channel should be carrying some useful information the research cannot ignore.

Principal component analysis is an orthogonalization process that transforms the observed variables into linearly independent variables which are called principal components. The principal components are arrayed in such an order that the *n*th principal component has the *n*th greatest variance. By combining the 21 estimated in-cylinder pressures into one matrix P with the dimension $m \times n$, where $n = 21$, the singular value decomposition of P is:

$$P = U\Delta V^T \tag{4.3}$$

where U is the $m \times m$ matrix of left singular vectors, V is the $n \times n$ matrix of right singular vectors, and Δ is the $m \times n$ rectangular diagonal matrix with the nonnegative singular values as the diagonal elements. The principal components are obtained based on singular value decomposition with equation 4.4:

$$F = U\Delta \tag{4.4}$$

To extract the most important information from the data matrix, generally the first few principal components will be retained. However, how many principal components should be retained is still an open problem [84]. The commonly used method is to retain the components whose eigenvalues are greater than the average of eigenvalues, but this procedure may lose some important information as discussed in [85]. In this work, a threshold value for the ratio between the cumulative eigenvalue and the summation of all the eigenvalues is determined. This ratio is expressed with equation 4.5:

$$R_i = \frac{\sum_{k=1}^{i} \Delta_k^2}{\sum_{k=1}^{M} \Delta_k^2}, i = 1,2 \ldots . M \tag{4.5}$$

The threshold value for R_i is set to 0.9. The first i principal components will be kept if summation of the first i eigenvalues can occupy equally or greater than 90% of the summation of all the eigenvalues. This is a much stricter standard than setting the average of eigenvalues as threshold. This way, more key information will be extracted from the

data matrix P, and the other principal components will be considered as the representatives of the noise. Figure 4.7 shows the results computed with equation 4.5.

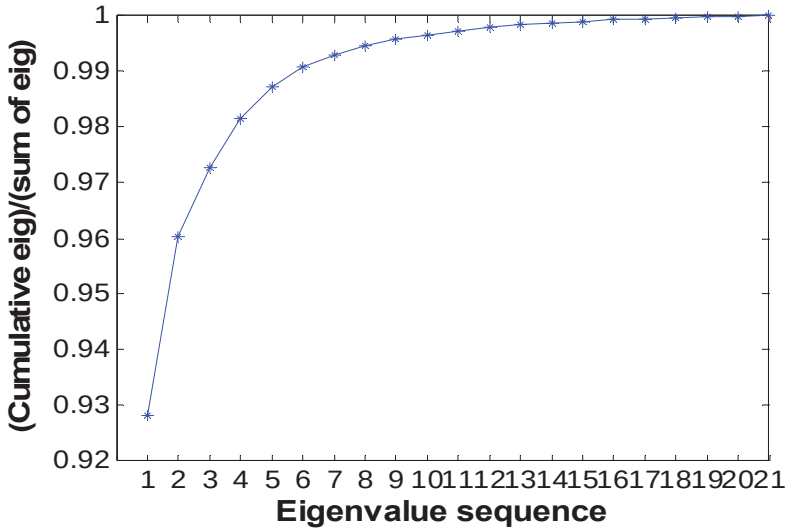

Figure 4.7: Ratio between cumulative eigenvalues and summation of eigenvalues, Test3

The first eigenvalue takes a proportion of 93% in the summation of all the eigenvalues as shown in Figure 4.7. So only the first principal component is considered as dominant and will be retained for further computation.

By replacing the $(i+1)$th to the Mth singular values (2^{nd} to 21th for Test 3) in equation 4.3 with zeros and averaging the new matrix P into one vector, the estimated pressures on the basis of 21 accelerometer channels are transformed to one pressure trace that is overlaid upon the measured pressure (Figure 4.8). Equation group (4.6) summarizes the PCA process described above and P_{est_pca} is the final estimated in-cylinder pressure based on the PCA method.

$$\begin{cases} P_{est}^{k} = ifft\left(\frac{fft(Accel_k)}{FRF_k}\right), k = 1,2,\dots M \\ P_{est} = U\Delta V^T \\ P_{est\_princ} = U\Delta V^T \; where \; \Delta_k = 0, k = i+1 \dots . M \\ P_{est\_pca} = \frac{\sum_{k=1}^{M} P_{est\_princ}^{k}}{M} \end{cases} \tag{4.6}$$

k: the column index.

$Accel_k$: Time domain accelerometer signal with the k th column acquired through the k th accelerometer channel.

FRF_k : Frequency response functions with the k th column representing the k th accelerometer channel.

fft: Fast Fourier Transform.

$ifft$: Inverse Fast Fourier Transform.

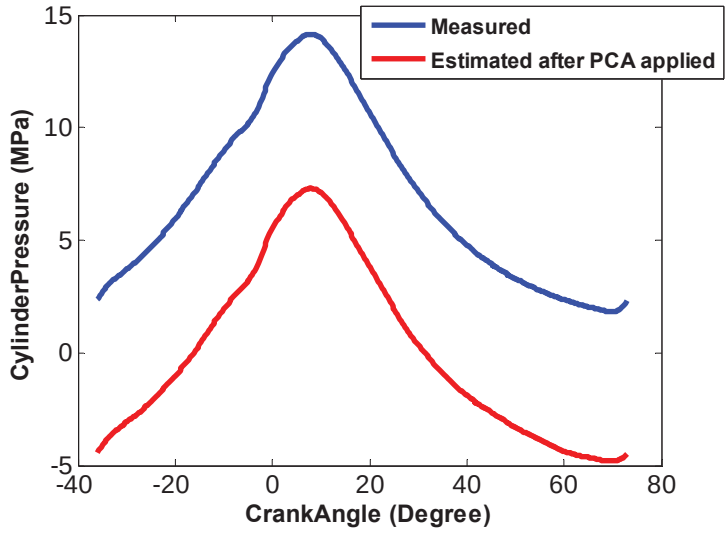

Figure 4.8: Estimated pressure after PCA procedure, Test 3

After the PCA procedure, however, great offset error between the estimated pressure and the measured in-cylinder pressure can be seen and needs to be compensated (Figure 4.8). It is known that during compression or expansion stroke, the relationship between in-cylinder pressure and volume follows equation 4.7 [14]:

$$PV^{\gamma} = constant \tag{4.7}$$

This formula relationship can be used to compensate the offset. When logarithm computation is performed on both sides of equation 4.7, γ is just the negative of the slope

of the logP-logV plot with respect to compression or expansion stroke as shown in equation 4.8:

$$Log(P) = -\gamma \cdot Log(V) + Log(contant) \tag{4.8}$$

For offset compensation purposes, compression stroke γ is utilized. Actually, either of the two strokes can help compensate the offset. Figure 4.9 displays the logP-logV plot based on measured in-cylinder pressure for all the test conditions listed in Table 3.2 and the γ values for compression stroke are given in the legend.

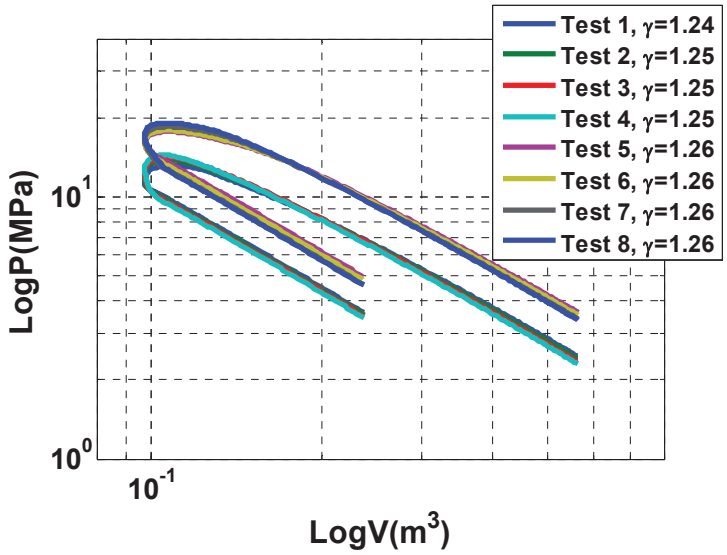

Figure 4.9: LogP-LogV plot for the eight tests

Referring to the γ values of different test conditions given in Figure 4.9, the compression ratio $\gamma = 1.25$ is utilized as the target to adjust the offset of the estimated pressure. At the beginning of offset compensation process, an initial offset compensation, $P_0 = 3.3MPa$, is added to the estimated in-cylinder pressure. With the difference between the γ of the estimated in-cylinder pressure and the goal of the compression ratio, $\gamma_{goal} = 1.25$, as the objective function, when the difference is greater than 0.001, a 0.1 MPa increment or decrement is added to the estimated in-cylinder pressure (if the difference is negative, an increment is added). This process moves on until the difference is lower than 0.001. Or if the searching iteration number for the compensation process is greater than 50, the

process will end up as well. It is considered that the shape of the estimated in-cylinder pressure is too far off from the measured in-cylinder pressure to satisfy the objective function.

The offset-compensated estimated in-cylinder pressure is plotted in Figure 4.10 by overlaying upon the measured in-cylinder pressure. It can be seen that the offset between the estimated and the measured in-cylinder pressures has been compensated successfully. However, this offset compensation method is only limited to the case that the shape of the estimated in-cylinder pressure is close to the shape of the measured one.

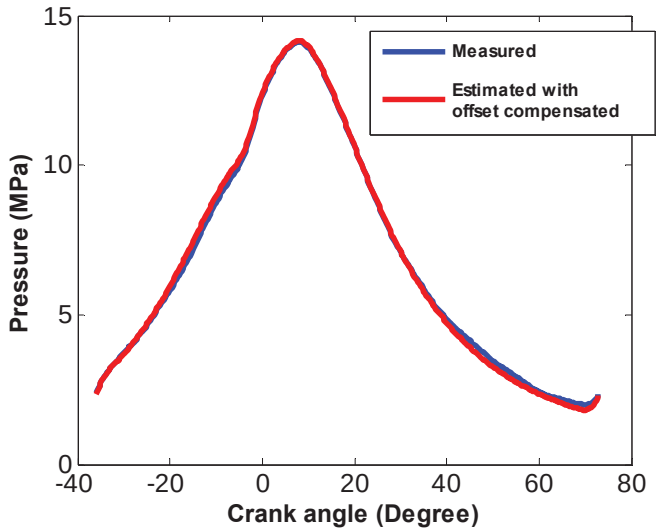

Figure 4.10: Estimated in-cylinder pressures with offset adjusted, Test 3

Figure 4.11 displays the reconstructed in-cylinder pressure for each test condition based on MISO model. It can be seen that the FRFs adapt to the SOI changes well at low load. For high load SOI sweep conditions, the errors can be observed at the expansion stroke after the pressure peak. However, the MISO model results in an improved reconstructed pressure for each test condition in comparison to the results based on the SISO model (Figure 4.4). Nevertheless, this improvement of result is at the cost of seven tri-axial accelerometers usage which is unrealistic for real-time online application. So it is meaningful to reduce the number of vibration acquisition channels without trading off the reconstruction accuracy.

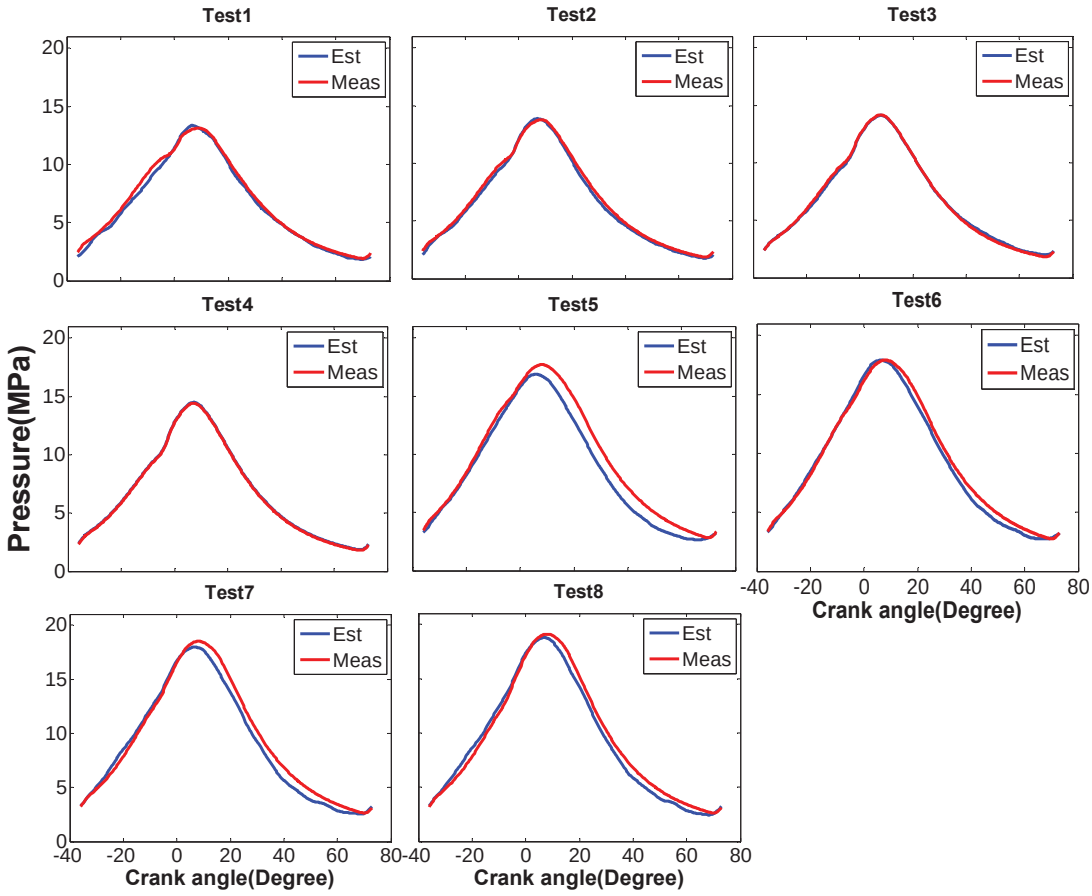

Figure 4.11: Estimated in-cylinder pressures with offset adjusted, eight tests

To quantitatively evaluate the reconstruction result, the errors of three pressure parameters between measured (low passed) and reconstructed pressures, PPA (peak pressure amplitude), PPCL (peak pressure crank angle location), and SPA (sample-based pressure amplitude) are utilized to check the reconstruction performance on both phase and amplitude perspectives. The respective errors are named as PPAE, PPCLE, and MAPE (mean absolute pressure error). For the estimated in-cylinder pressure P_{est}^{i} and the measured in-cylinder pressure P_{meas}^{i} within one windowed cycle, the MAPE is computed as:

$$MAPE = \frac{\sum_{i=1}^{N} abs(P_{est}^{i} - P_{meas}^{i})}{N} \tag{4.9}$$

where N is the sample number in one windowed cycle, i is the sample number index.

The procedure for reducing the number of vibration acquisition channels in MISO model starts from minimizing the number of the triaxial accelerometers. Then, further minimization of channel number will be performed on the candidate channels supplied by these qualified triaxial accelerometers. By averaging through all the tests, the errors of the three pressure parameters reconstructed based on 21 input channels are: PPAE=0.4Mpa, PPCLE=1.4DBTDC, and MAPE=0.5DBTDC. Accordingly, the thresholds as the standard for selecting the qualified accelerometers or channels are determined as: PPAE=0.5Mpa, PPCLE=1.6DBTDC, and MAPE=0.6DBTDC, so that the reconstruction accuracy can be guaranteed even though the input channel number is reduced. Only the accelerometers or channels based on which the errors of all the three pressure parameters are lower than the thresholds will be retained.

Table 4.1 lists the number of combinations corresponding to the number of triaxial accelerometers that are combined.

Table 4.1: Number of combinations for accelerometers

Number of triaxial accelerometers for combination	Number of combinations
1	**7**
2	**21**
3	**35**
4	**35**
5	**21**
6	**7**
7	**1**

PPAE, PPCLE, and MAPE are computed for all the possible combinations that are relative to the number of triaxial accelerometers used for combination. The mean and standard deviation of the three pressure parameters are displayed in Figure 4.12. The bars represent the mean value and the error bars describe the standard deviation.

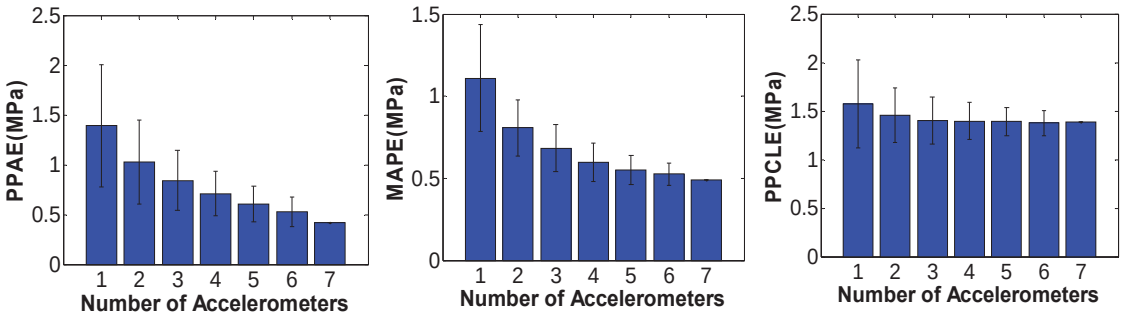

Figure 4.12: In-cylinder pressure estimation results relative to the combinations of accelerometers

With the increase in the number of accelerometers, no obvious improvement can be seen for the PPCLE result based on the interpretation of the mean value, but the decreasing standard deviation confirms that the extremely good or bad result comes closer to the average. However, the estimations of the amplitude parameters, PPA and SPA, are improved as verified by the decreasing mean and standard deviation when more accelerometers are used especially when the accelerometer number increases from one to two.

By applying the thresholds, PPAE=0.5Mpa, PPCLE=1.6DBTDC, and MAPE=0.6DBTDC, to all the combinations, the combinations that can bring the PPAE, PPCLE, and MAPE lower than the thresholds are qualified to retain. Figure 4.13 shows the ratio of the qualified combinations relative to how many accelerometers are utilized. With more accelerometers being employed, the ratio of qualified accelerometers increases.

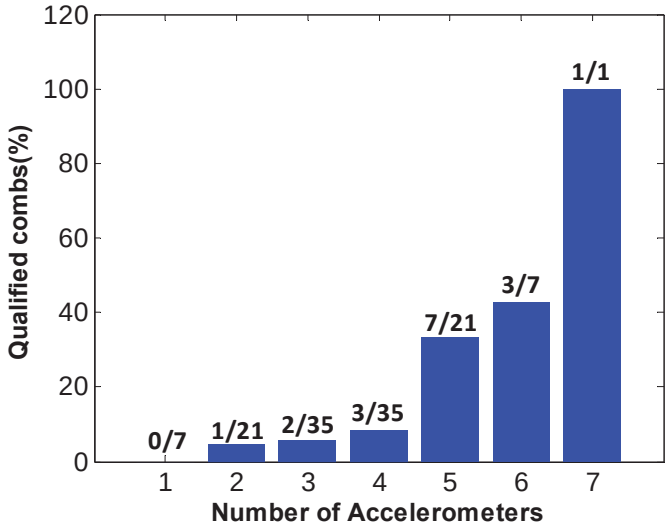

Figure 4.13: Qualified combinations relative to the number of accelerometers

With the increase in the number of accelerometers, no obvious improvement can be seen for the PPCLE result based on the interpretation of the mean value, but the decreasing standard deviation confirms that the extremely good or bad result comes closer to the average. However, the estimation of amplitude parameters, PPA and SPA, is improved as verified by the decreasing mean and standard deviation when more accelerometers are used especially when the accelerometer number increases from one to two.

By applying the thresholds, PPAE=0.5Mpa, PPCLE=1.6DBTDC, and MAPE=0.6DBTDC, to all the combinations, the combinations that can bring the PPAE, PPCLE, and MAPE lower than the thresholds are qualified to retain. Figure 4.14 shows the ratio of the qualified combinations relative to how many accelerometers are utilized. With more accelerometers being employed, the ratio of qualified accelerometers increases.

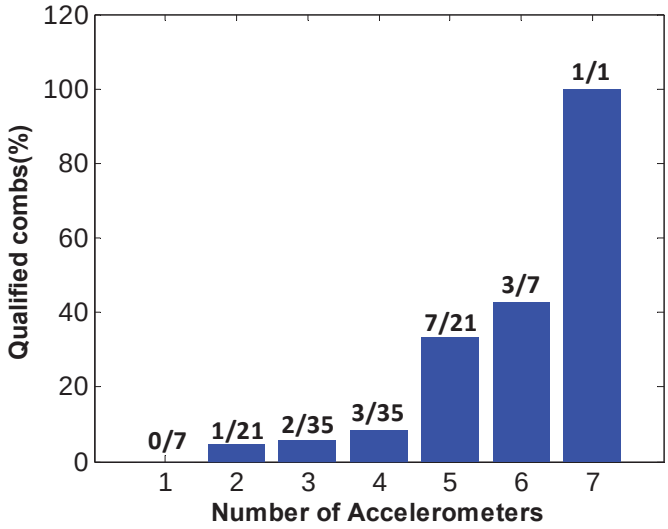

Figure 4.14: Qualified combinations relative to the number of accelerometers

As we pursue the usage of fewer accelerometers, the qualified combination in the 21 combinations of two accelerometers stands out. This combination is composed by accelerometers 5 and 7. Further work will focus on seeking the qualified combination composed of a minimum number of channels from the six channels supplied by accelerometers 5 and 7. The number of possible combinations relative to the number of channels is listed in Table 4.2.

Table 4.2: Number of combinations for accelerometer channels

Number of channels for combination	Number of combinations
1	**6**
2	**15**
3	**20**
4	**15**
5	**6**
6	**1**

Figure 4.15 shows the mean and standard deviation of PPAE, MAPE, and PPCLE depending on the number of combined channels. The channel number increase brings about significant improvement for PPA and SPA estimation as both the mean and

deviation of the error decrease. But more than two accelerometer channels do not make the PPCL estimation more accurate than the PPCL estimated from two channels. The most obvious improvement for all the three pressure parameters happens when the channel number increases from one to two.

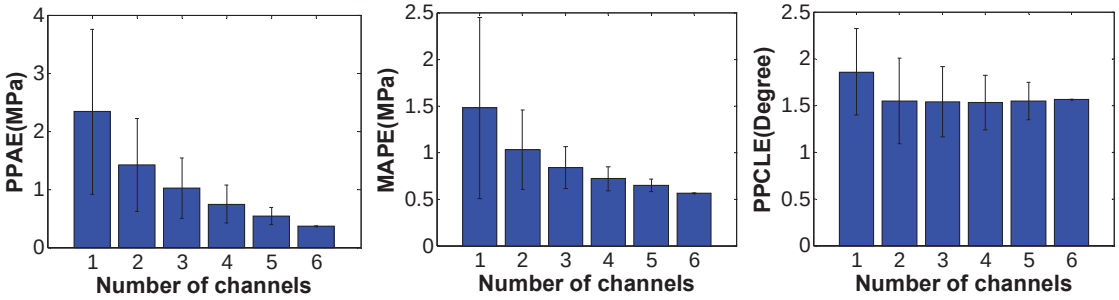

Figure 4.15: In-cylinder pressure reconstruction results relative to the number of combined channels from accelerometers 5 and 7

Similar to the procedure of selecting the accelerometers, the same thresholds are applied to the three pressure parameters. In Figure 4.16, the qualified combinations are marked with green blocks and unqualified ones marked with red blocks. Each block in Figure 4.16 is filled with the sequence numbers of the being evaluated combined channels, where the channels with ID number 5z, 5y, 5z, 7x, 7y, and 7z are represented by a new sequence 1, 2, 3, 4, 5, and 6.

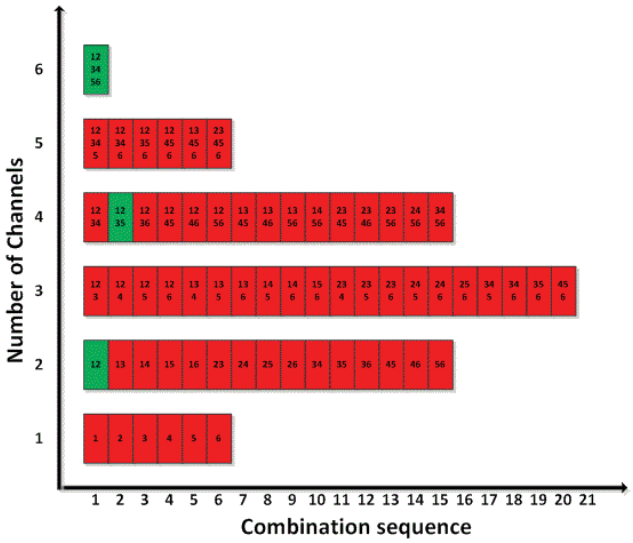

Figure 4.16: Evaluation of reconstruction results for all combinations of six channels

As we pursue the usage of fewer accelerometers, the qualified combination in the 21 combinations of two accelerometers stands out. This combination is composed by accelerometers 5 and 7. The work next will focus on seeking the qualified combination composed of a minimum number of channels from the six channels supplied by accelerometers 5 and 7.

By applying the same procedures as selecting the optimal tri-axial accelerometers, channel 5x and channel 5y are finally selected as the optimal channel combination to estimate the in-cylinder pressure. As shown in Figure 3.1, accelerometer #5 is placed close to cylinder 1 on the engine block. The reconstructed pressure overlaid upon the measured pressure is plotted in Figure 4.17 for each conducted test condition. Based on the observation on Figure 4.17, the reconstruction results for low load test conditions with SOI sweep are better than the results achieved by the SISO model. For Test 5 and Test 6 at high load conditions, the compression stoke can be estimated with high accuracy, but the errors can be seen in combustion and expansion strokes. For Test 7 and Test 8, most errors appear before pressure peak and at the end of the expansion stroke. However, the reconstruction results for high load SOI sweep test conditions are improved in comparison to the results obtained with the SISO model.

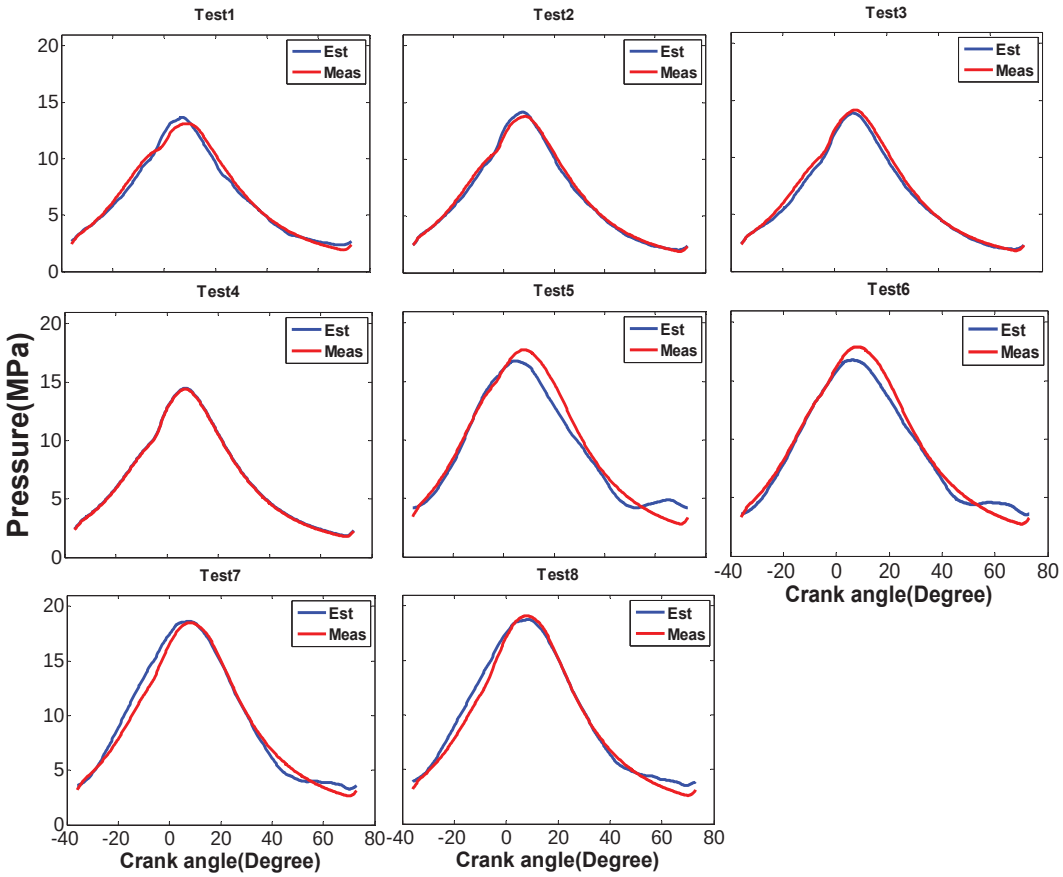

Figure 4.17: Estimated in-cylinder pressures for cylinder 1 based on vibration signatures acquired through channels 5x and 5y, FRF computed through channels 5x and 5y on Test 4

To further evaluate the robustness of the obtained two-input single-output model, this model is applied to more tests (listed in Table 4.3) with diverse speed and load conditions. The same FRFs computed through channel 5x and 5y based on Test 4 are used to recover the in-cylinder pressure for the Tests 9-16 given in Table 4.3. Both the PCA and the offset compensation processes are applied to optimize the in-cylinder pressure recovery results. Figure 4.18 shows the in-cylinder pressure recovery results based on the MISO model. Figure 4.19 shows the results based on the SISO model with the accelerometer signal acquired through channel 4x as the input and the FRF is computed through channel 4x. Both figures take the measured in-cylinder pressure as the reference to show the difference.

Table 4.3: Additional engine test conditions for robustness examination

Test condition	Engine Speed (RPM)	Engine Load (Nm)	Start of injection (DBTDC)	Injection duration (CAD)
9	1169	1646(70%)	5.6	19.3
10	1169	1646(70%)	5.5	18.4
11	1195	412(20%)	9.5	5.2
12	1195	412(20%)	4.1	5.2
13	1600	873(50%)	7.3	10.5
14	1600	873(50%)	10.2	10.3

Improvements of the in-cylinder pressure recovery can be seen based on the MISO model in comparison to the SISO model, although the estimated in-cylinder pressure curves with the MISO model do not coincide with the measured in-cylinder pressure curve with the accuracy as high as for 2200RPM conditions. The especially low estimation accuracy based on the MISO model occurs on Test11 and Test12 (low speed and low load conditions). For the conditions with 1600RPM engine speed, the best result occurs on 50% load and 10.2 degree SOI. For other 1600RPM conditions, low estimation errors can be seen for the compression engine stoke, but the errors increase for the combustion stroke. The errors of the compression stroke are low except for the 50% load 7.3 degree SOI condition. Overall, however, the robustness of FRF application for the in-cylinder pressure estimation has been greatly improved based on the presented MISO model in comparison to the SISO model. As the error of the in-cylinder pressure recovery result based on SISO model is too larger, no quantified MISO-model-based estimation improvement is shown in this chapter to present the MISO model's superiority.

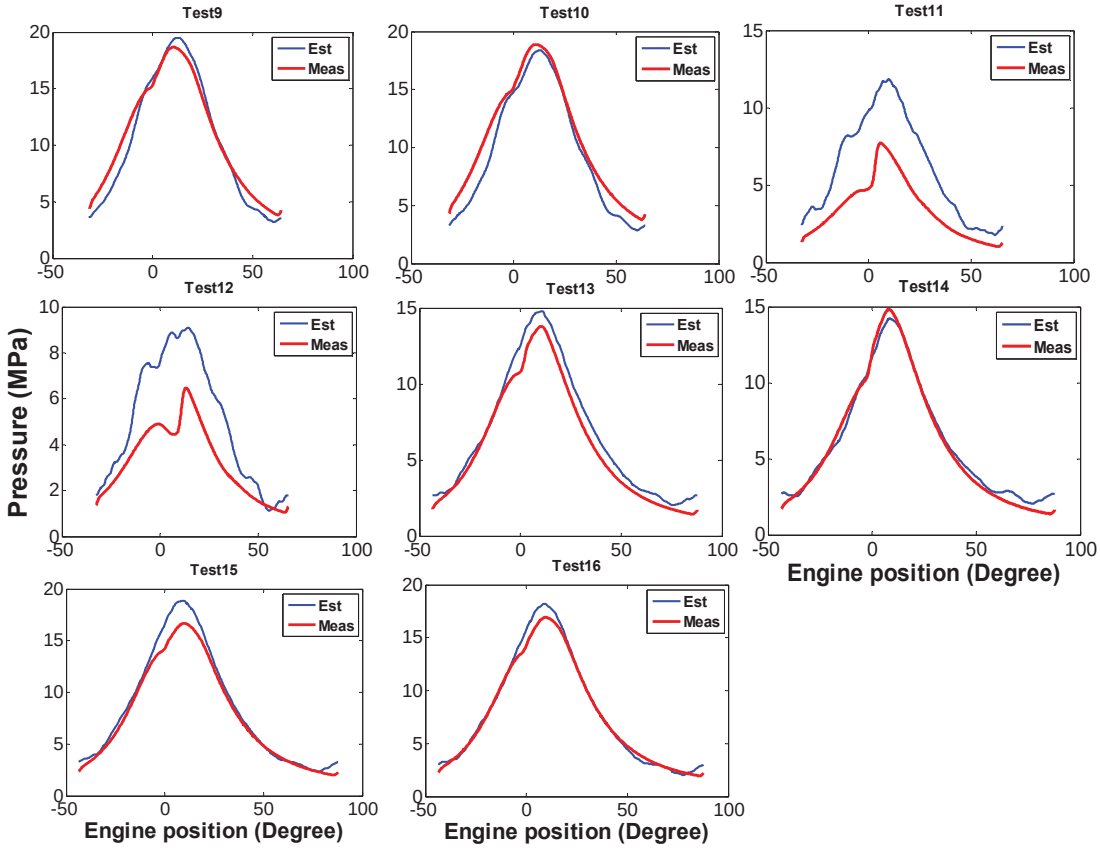

Figure 4.18: Estimated in-cylinder pressures based on vibration signatures acquired through channels 5x and 5y, FRF computed through channels 5x and 5y on Test 4

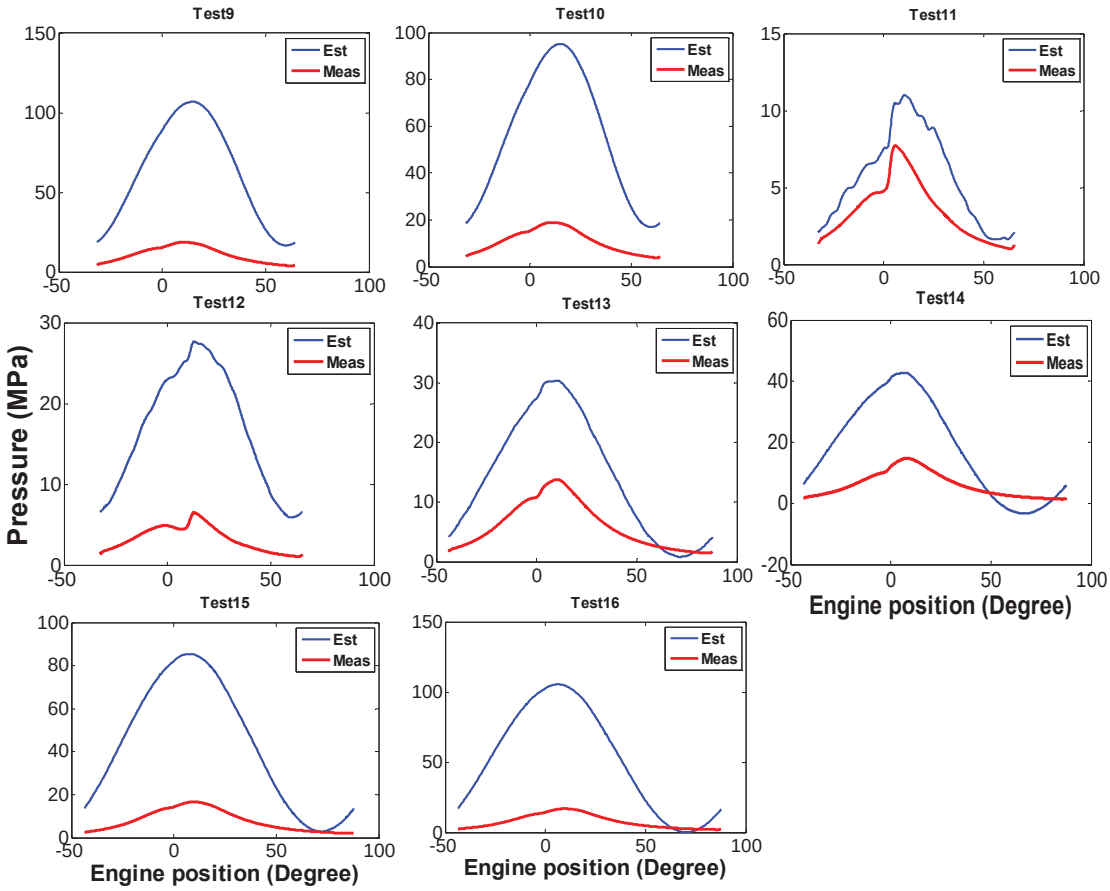

Figure 4.19: Estimated in-cylinder pressures based on vibration signatures acquired through channels 4x, FRF computed through channels 4x on Test 4

More than the result comparison based on observations, PPAE, PPCLE, and MAPE, are used to quantitatively evaluate the in-cylinder reconstruction performance of the SISO and MISO (two-input single-output) FRF models. The bars in Figure 4.20 represent how much improvement of the parameter estimation is achieved with the MISO model by comparing to the SISO model. Both the MISO model and the SISO model are computed from Test 4. The positive value indicates "real" improvement has been made by the MISO model, and negative value shows that the pressure parameter estimation based on the MISO model is worse than that based on the SISO model. Specifically, improvement of PPAE and MAPE are defined as

$$PPAE_{imp} = (PPAE_{SISO} - PPAE_{MISO})/PPAE_{SISO} \tag{4.10}$$

and

$$MAPE_{imp} = (MAPE_{SISO} - MAPE_{MISO})/MAPE_{SISO} \quad (4.11)$$

in percentage.

Improvement of PPCLE is defined as

$$PPCLE_{imp} = PPCLE_{SISO} - PPCLE_{MISO} \quad (4.12)$$

in degree.

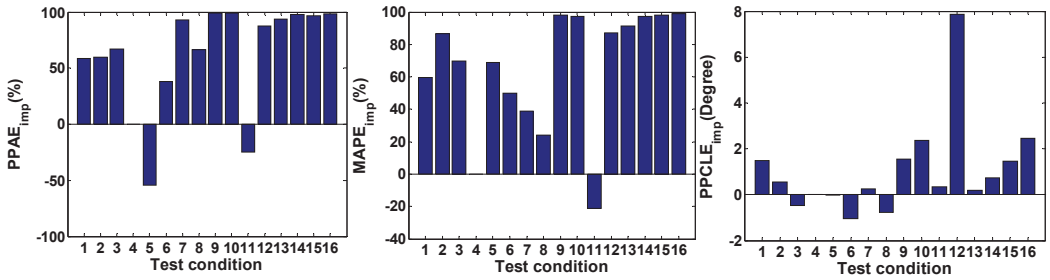

Figure 4.20: Pressure parameters estimation improvement based on the MISO (two-input single-output) FRF model in comparison to the SISO FRF model (MISO and SISO FRF models were computed from Test 4)

For the PPAE and MAPE values, the greater than 0 (within the 100% upper limit), the more improvements are introduced by the MISO model. Negative PPAE value which represents a worse estimation based on the MISO model occurs on Tests 5 and 11. For Test 5, 0.3MPa more estimation error is introduced by the MISO model ($PPAE_{SISO}$ =0.6MPa and $PPAE_{MISO}$ =0.9MPa). For Test 11, 0.8MPa more error is introduced by the MISO model ($PPAE_{SISO}$ =3.3MPa and $PPAE_{MISO}$ =4.1MPa). With respect to MAPE, negative value occurs on Test 11 and the MISO model led to 0.5MPa more estimation error ($MAPE_{SISO}$=2.2MPa and $PPAE_{MISO}$=2.7MPa).

MISO FRF model does not lead to consistent improvement for PPCL estimation. Enlarged error occurs to Tests 3, 5, 6, and 8. However, the PPCLE increases for the four tests based on the MISO model are within 1 degree, which can be considered as minor deterioration.

However, the application of the MISO FRF model leads to more accurate estimation results for majority of the tests. Improvement can be seen for 75% of the tests with the evaluation based on PPCLE, 88% of the tests with the evaluation based on PPAE, and 94% of the tests with the evaluation based on MAPE.

4.3 Summary and Conclusion

FRF was used to model the connection between the in-cylinder pressure and the vibration signatures acquired through accelerometers mounting on engine block and engine head on a 9L inline 6-cylinder diesel engine. Based on SISO and MISO models, the robustness of FRF with respect to speed, load, and SOI variations was evaluated.

The results showed that the SISO model computed based on Test 4 with the input acquisition channel selected depending on coherence analysis did not render an FRF that can fit the conditions with speed, load, and SOI variations. For the MISO model, the multiple FRFs improved the pressure reconstruction with the assistance of principal component analysis and offset-compensation processes. With the purpose of minimizing the cost for accelerometer mounting and usage, two channels, 5x and 5y, were confirmed to be the optimal choice which can meet the threshold requirements (PPAE=0.5Mpa, PPCLE=1.6DBTDC, and MAPE=0.6DBTDC) given based on engine conditions with 2200rpm engine speed. Then the performances of two-input single-output and SISO models were evaluated by the three in-cylinder pressure parameters (PPAE, MAPE, and PPCLE) based on all engine tests conducted in this paper. The two-input single-output FRF model introduced significant improvement to the estimation of the three in-cylinder pressure parameters for over 75% of the tests.

So the two-input single-output FRF model coupled with the PCA and offset compensation processes proposed in this paper can improve the robustness of FRF for the estimation of combustion metrics with the accelerometer signals as the inputs. It implies that the application of FRF for combustion metrics estimation can be extended to varied test conditions rather than only the same or similar test conditions.

Chapter 5

Radial basis function neural network[1]

In this chapter, RBFNN was used to correlate the accelerometer signal and AHR. Although AHR can be derived by the estimated in-cylinder pressure, accurate estimated AHR will not be reached if the error of the estimated in-cylinder pressure is incorporated in the AHR computation process. The research was conducted based on a 9L in-line 6-cylinder medium duty diesel engine in comparison to the light duty diesel engine used in Bizon's research. In addition in this work, two algorithms that select the weight vectors in the hidden layer were implemented and are discussed and compared to make this network more robust and efficient. The trained network was proven to be highly robust in combustion metrics reconstruction for a wide range of conditions even if artificial noise was added to the accelerometer signal.

5.1 Test conditions

In total 87 tests were conducted on this engine. The selected tests cover multiple speeds, loads, and SOI conditions whose combinations aim to mimic the infield engine operating conditions. At each speed condition (low speed: 1195 rpm, medium speed: 1600 rpm, and high speed: 2200 rpm), both low load and high load tests were conducted (Figure 5.1). Speed sweep tests were developed with 50 RPM increments from 2000 to 2200 RPM at a load of 725Nm. Pilot injection and EGR changes have not been used to differentiate the conditions in this chapter.

[1] The material contained in this chapter was published as a journal article [i].

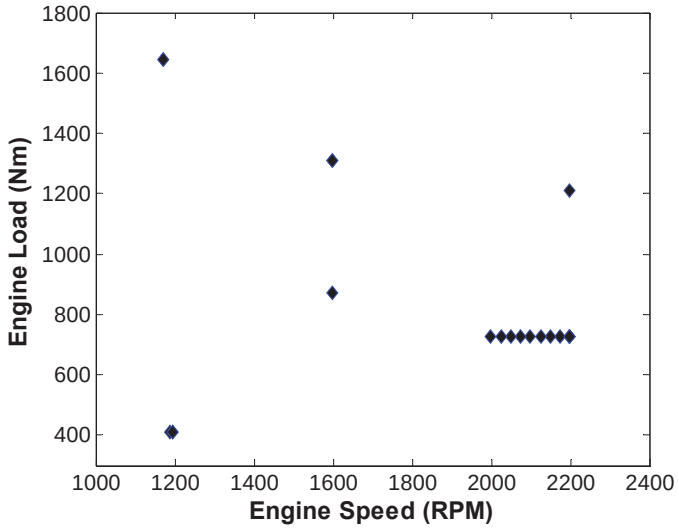

Figure 5.1: Test conditions (87 test points) comprised of load conditions

For each speed and load combination, an SOI sweep was developed. Figure 5.2 illustrates the test conditions with the main start of injection relative to the engine speed (a) and load (b).

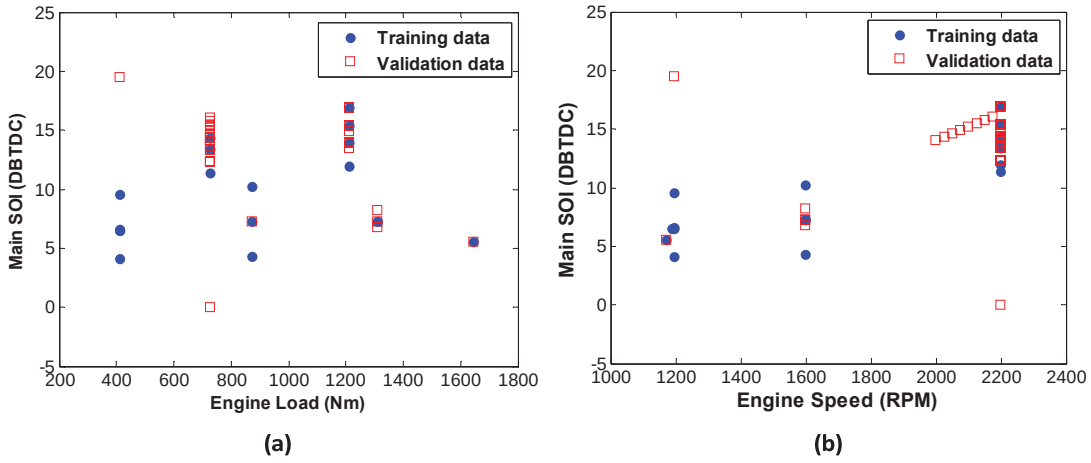

Figure 5.2: Test conditions including breakdown of training and validation data plotted as start of injection versus speed (a) and torque (b)

5.2 Combustion metrics

Apparent heat release rate (AHR) $\dot{Q}$ computed by equation 5.1 is an indicator of energy conversion rate of the combustion of fuel from chemical to sensible energy, and equals the rate at which the work is done on the piston plus the rate of change of sensible internal energy of the cylinder contents [14].

$$\dot{Q} = \frac{dQ}{dt} = \frac{\gamma}{\gamma - 1} \cdot P \cdot \frac{dV}{dt} + \frac{1}{\gamma - 1} \cdot V \cdot \frac{dP}{dt} \tag{5.1}$$

$\dot{Q}$: Apparent Heat Release rate (MW)

V: Cylinder volume (L)

P: Cylinder pressure measured from in-cylinder pressure sensor (MPa)

γ: Polytropic coefficient or ratio of specific heats c_p / c_v.

t: Time (Sec)

Depending on the AHR, a number of combustion metrics, including SOC (start of combustion with the AHR at 0.1 MW), PACL (peak AHR crank angle location), PAA (peak AHR amplitude), and CA50 (crank angle location for 50% fuel burnt), which denote the phasing and quantify combustion can be determined. Moreover, these combustion metrics can also evaluate the accuracy of AHR estimation results. The AHR relative to crank angle degrees is shown in Figure 5.3 with the combustion metrics presented above identified. Since Morello's research [58] indicated that the signal content within the 0 – 2 kHz frequency band is the most correlated to the combustion event on this engine, the AHR plotted in Figure 5.3 is low-pass filtered with the cutoff frequency at 2 kHz. A window with a length of 90 degrees was selected for each cylinder combustion event from -30 to 60 degrees. The AHR obtained with the above process will be called derived AHR in the following sections of the chapter.

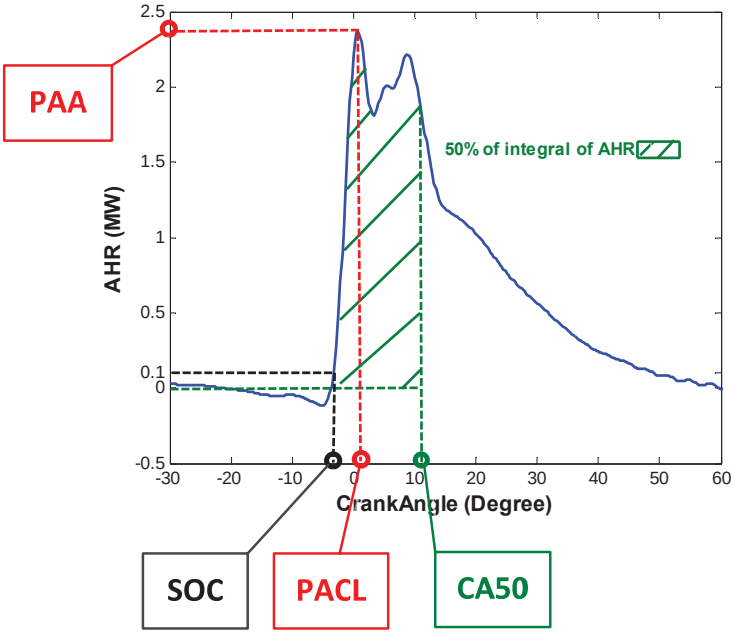

Figure 5.3: AHR trace marked with combustion metrics (engine speed = 2200 rpm, engine load = 725 Nm, SOI = -11.3 °CA)

5.3 Radial basis function neural network

It is difficult to formulate a linear model between an accelerometer signal and AHR due to their nonlinear relationship and the noise introduced into the accelerometer signal. The Radial Basis Function Neural Network (RBFNN) is therefore employed to create a nonlinear mapping between the two signals through the training process. The RBFNN is characterized by the capability of learning the association between an input and an output signal to mimic the flexibility of the transmission between them, even under low signal to noise ratio conditions. The proposed RBFNN is composed of four layers as displayed in Figure 5.4: the input layer, the radial basis layer with *M* neurons, the linear layer with *S* neurons, and the output layer [86]. Figure 5.5 shows the accelerometer signal and the derived AHR that are used to train the RBFNN by feeding the input and the output layers respectively. According to equation 5.1, the AHR as the output is derived based on the in-cylinder pressure acquired from cylinder 1. The accelerometer signal used as the input of RBFNN is from the X orientation of accelerometer #4, which is placed closest to cylinder

1 and oriented along the piston reciprocating movement. The ability of the radial basis function network to process the data that is "new" depends on both the optimized parameters (*RW*, m_1, *LW*, and m_2) and the input-output training data set.

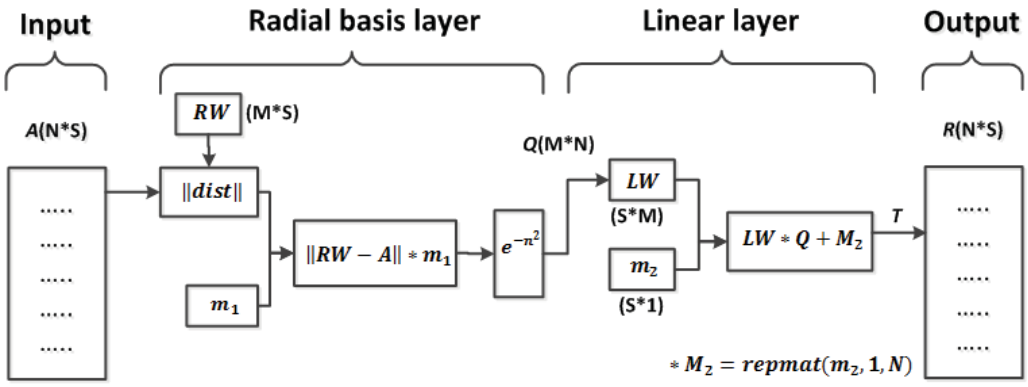

Figure 5.4: Radial basis function network structure

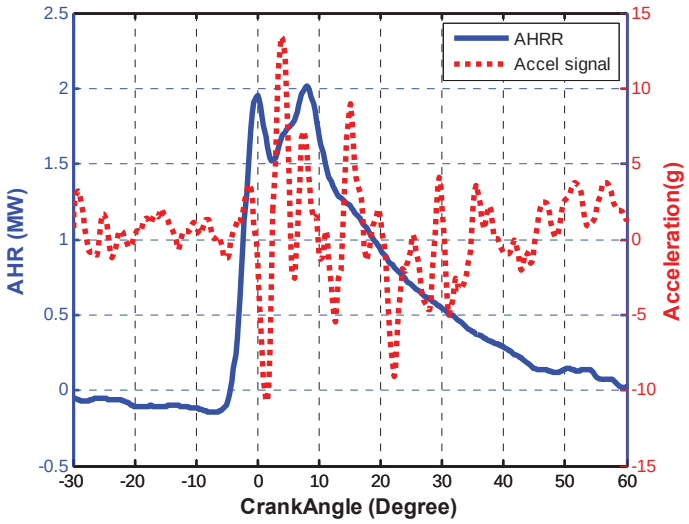

Figure 5.5: Accelerometer signal overlaid upon derived AHR trace

The radial basis function, $f(n) = e^{-n^2}$, has a maximum of 1 for an input of 0 and close to the minimum of 0 when the input moves towards either positive or negative infinity. The input to the radial basis function is the vector distance $\| RW - A \|$ between the weight vectors *RW* and the input vector *A*. When the distance between vectors *RW* and *A*

increases, the output of the radial basis function decreases. This property of the radial basis function, called localization, is preferred in neural network training, because the significant difference between the input *A* and the weight vectors *RW* results in an output close to zero and the small output of the radial basis function layer has only a minor effect on the linear layer. The variable m_1 is the bias that allows for adjusting the sensitivity of the radial layer. The same with Bizon's work [67], mean square error is used as the criteria to make a choice for m_1 and the number of weight vectors *RW*. In this work, m_1 is set as 50 and the number of weight vectors *RW* expressed by *M* is fixed at 100 with the input and the output data both with a dimension of 600×423 (*N*=600, *S*=423), where 600 is the number of vectors and 423 is the length of each vector. More details about how to work out *LW* and m_2 are given in [86]. The "*repmat"* computation within the linear layer in Figure 5.4 transfers m_2 to M_2 by repeating the column m_2 *N* times to match the size of matrix $LW * Q$.

Based on the neural network structure described above, the method for selecting 100 of the 600 vectors of *A* to compose the weight vector *RW* must be determined. Random selection would take the least effort but likely lead to the least accurate results because the resulting *RW* may not accurately represent the pattern and features of the training input data. Therefore, two algorithms are presented here to select the weight vector for the RBFNN structure so as to output the predicted AHR with high accuracy, even if the input has never been "seen" by the network.

5.4 Modified Gram-Schmidt method

Given that the linear layer of the RBFNN is a special case of a linear regression model [87],

$$R = LW \bullet Q + M_2 \tag{5.2}$$

Q is the output of the radial basis layer with a dimension *N*×*N* as all the vectors of *A* are taken as the candidates for *RW* component selection.

The orthogonalization process is applied to the output of the radial basis layer, *Q*. The orthogonalized vectors will span the same subspace as *Q*, while being linearly independent in the new subset. Thereafter, the correlation between the output *R* and each single orthogonal basis vector can be evaluated.

As the classical Gram-Schmidt procedure is sensitive to round-off errors, the more stable Modified Gram-Schmidt algorithm is employed to decompose *Q* into orthogonal basis vectors q_k. At the *k*th iteration, the Modified Gram-Schmidt operates on the (*k*+1)th to the *N*th columns of *Q* to make them orthogonal to the *k*th column and repeats this process for $k = 1,2,\ldots.100$. As suggested by Chen in [87], the criterion used to select the component of *RW* is to evaluate the contribution of each orthogonalized vector of q_k to the total energy of output of the network, *R*. By rearranging the error definition equation given in [87], equation 5.3 is obtained to compute each orthogonalized vector's contribution to *R*.

$$Ctr(i) = \frac{\langle q_k(i),R\rangle^2}{\langle q_k(i),q_k(i)\rangle\langle R,R\rangle} \tag{5.3}$$

Where $\langle \bullet,\bullet \rangle$ denotes the inner product.

The index of $q_k(i)$ which results in the maximum Ctr is used to locate the *RW* components from *A*.

5.5 Principal component analysis method

Principal component analysis (PCA) is a process that uses an orthogonal transformation to convert data composed of correlated variables into a set of linearly uncorrelated variables called principal components. These components are arranged in such an order that the first component has the largest variance and the *n*th component has the *n*th highest variance. PCA is a well-known technique in reducing the large dimensionality of data space into a smaller one by discarding the minor components which are characterized by small variances. Meanwhile, the lower dimension of the data space retains the most relevant information from the original data. As the *RW* in the radial basis layer is expected to carry the most representative characteristics of the training data and

make the network sufficiently reflect the transmission features between the input and the output with a dimension lower than *A*, the PCA method is employed for *RW* selection.

PCA method is first applied to the response of radial basis layer, *Q*. The reason why PCA is applied to *Q* is that *Q* is linearly correlated to the output *R* and the features of the output *R* are expected to be extracted and retained since the output quality is the primary concern for the network application. Moreover, components of *Q* can be used to trace the corresponding components of *A* with the same indices. A matrix, defined as $X_k (k = 1,2, \dots 100)$, is then constructed by selecting 100 vectors from *Q* under the criterion that X_k can most resemble the first 100 principal components of *Q*. The *RW* is selected from *A* with the same indices as X_k is selected from *Q*. As all the training data are taken as the candidates for *RW* component selection, *Q* is a matrix with $N \times N$ dimension. The PCA result of the output of the radial basis layer, *Q*, that preserves the same dimension with *Q* is presented in equation 5.4:

$$Y^T = Q^T W = V \sum^T W^T W = V \sum^T \tag{5.4}$$

The singular value decomposition of Q is $Q = W \sum V^T$, W is an $N \times N$ matrix of eigenvectors of the covariance matrix QQ^T, $\sum$ is an $N \times N$ diagonal matrix of eigenvalues, and V is an $N \times N$ matrix of eigenvectors of $Q^T Q$.

Figure 5.6 illustrates the process that constructs X_k through the selection of the component vectors from Q. The objective function $F(X_{ki}, Y_k)$ is a quantified criterion that compares the two input matrices, X_{ki} and Y_k. The maximum of the objective function, $F(X_{ki_k}, Y_k)$, indicates that the two input matrices, X_{ki_k} and Y_k, resemble each other the most. The creation of the objective function is based on the Procrustes analysis which involves three steps including translation, rotation, and dilation. More details about Procrustes analysis are given in [88]. Initially, all the vectors of *Q* are considered as candidates and the vector that can maximize the objective function is selected to compose X_1. Also, the selected vector is emptied from *Q* so that the future selection for component of X_k will not consider this selected vector again. At the kth iteration, $k =$

2,3, ... 100, only the vector in the slimmed Q that can maximize the objective function will be selected to compose X_k.

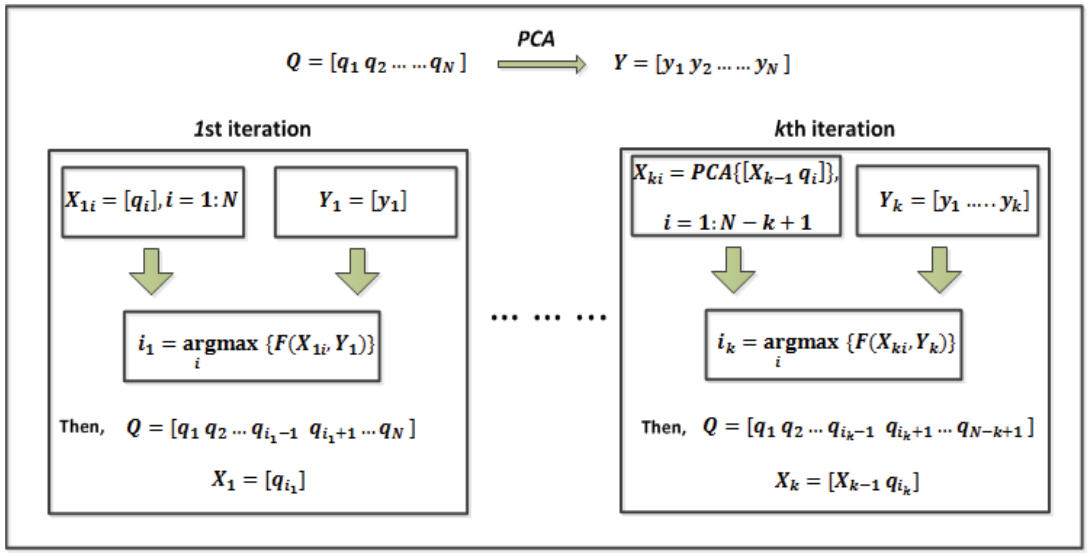

Figure 5.6: Schematic illustration for selection of $\boldsymbol{X_k}$ from Q

5.6 Results

Twenty one of the 87 tests were used to train the RBFNN to determine the optimal parameters (RW, m_1, LW, and m_2). This fixed network is then applied to estimate the combustion metrics for the other 66 tests. As shown in Figure 5.2(b), the tests marked with circles were employed for network training and the tests marked with squares were used for network validation. Table 5.1 indicates the estimation errors of the combustion metrics including SOC, PACL, PAA, and CA50. The PAA error is divided by the PAA of derived AHR. The mean and root-mean-square error (RMSE) in Table 5.1 represent the mean error and errors' standard deviation across the 66 tests. A low RMSE of any specific error indicates the errors across the 66 tests maintain close to the mean value of these errors. The mean and RMS errors are averaged and computed respectively with respect to all the test conditions and all the measured cycles.

As shown in Table 5.1, both the error and the RMSE of SOC estimation are controlled within 1 degree for the three RW selecting approaches. The randomly selected RW results

in the SOC being estimated with a higher error at 0.7 degrees and the RMSE at 1.0 degree in comparison to the other two methods. The mean estimated errors in CA50 are all similar at 1.7 to 1.8 degrees and similar RMSE's of 1.8 to 1.9 degrees.

Accuracy with respect to PACL estimation is lower than SOC because there are two peaks in the AHR curve with amplitudes close to each other under the high speed low load conditions (e.g., 2200 rpm and 725 Nm) as shown in Figure 5.7. The estimator of PACL can shift from one peak to another when the two amplitudes are close to the same in magnitude and closely spaced as in Figure 5.7. In this case, a 10 degree shift of the PACL is induced between the derived and estimated results depending upon only small changes in the combustion condition or estimator.

Table 5.1: Combustion parameter estimation results with comparison for errors between accelerometer based RBFNN estimated and cylinder pressure derived AHR combustion parameters

Combustion Parameter	***RW* selected based on MGS**		***RW* selected based on PCA**		***RW* selected randomly**	
	mean	**RMSE**	**mean**	**RMSE**	**mean**	**RMSE**
SOC (°CA)	0.5	0.8	0.4	0.6	0.7	1.0
CA50 (°CA)	1.7	1.9	1.8	1.8	1.8	1.7
PACL (°CA)	3.7	4.0	4.5	4.5	4.7	3.2
PAA (%)	9.5	7.0	9.9	6.3	13.2	6.6

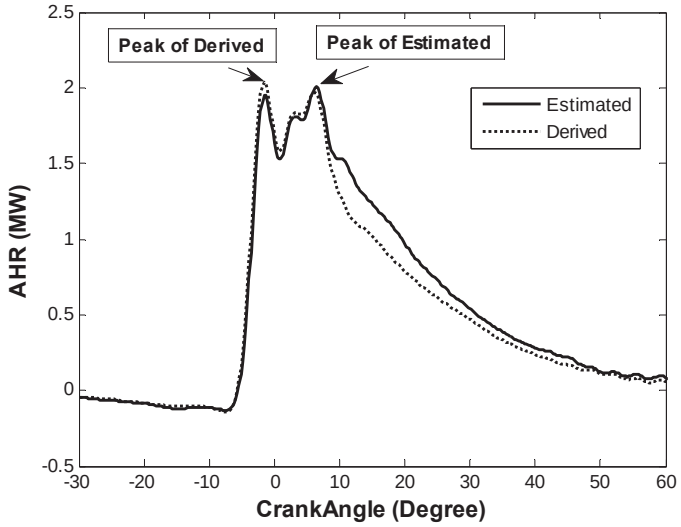

Figure 5.7: AHR signatures indicating PACL differences between estimated and derived for engine speed = 2200 rpm and engine load = 725 Nm

Based on the evaluation from the four combustion metrics, there is no significant estimation accuracy difference between the two network structures with *RW* selected by either the PCA or the MGS methods. However the two *RW* selection methods show quantitatively improved SOC and PAA combustion parameters in comparison to the randomly selected *RW* method.

In addition to the accurate estimation of combustion metrics, the success of combustion sensing based on accelerometers depends on how well the estimated AHR trace matches the derived AHR trace. CA50 may reflect the crank angle based amplitude difference between estimated and derived AHR since it depends on the computation of the summation of AHR. However, the amplitude difference details cannot be indicated. To compare the AHR reconstruction results on a more comprehensive basis, the estimated AHR traces are overlaid upon the derived AHR trace, as shown in Figure 5.8. The test conditions in Figure 5.8 reflect the various combinations of low and high engine speeds, low and high loads, and SOI changes in the non-training dataset. Based on the comparison of the estimation results among the three weight vector selection methods, it can be seen that the PCA and MGS method result in the estimated AHRs with shapes and amplitudes closer to the derived ones. Again there is no significant performance

difference observed between these two. Significant differences in the AHR shape are observed for the random selection method results in the AHRs estimated. See for example Figure 5.8(e) where the derived AHR shows only a minimal first peak, but the estimated AHR via RBFNN with the randomly selected weight vectors for *RW* has a distinct first peak. For the validation test conditions shown here, the random case has higher error. Furthermore, the estimation results based on the random method may be worse if other weight vectors were randomly selected.

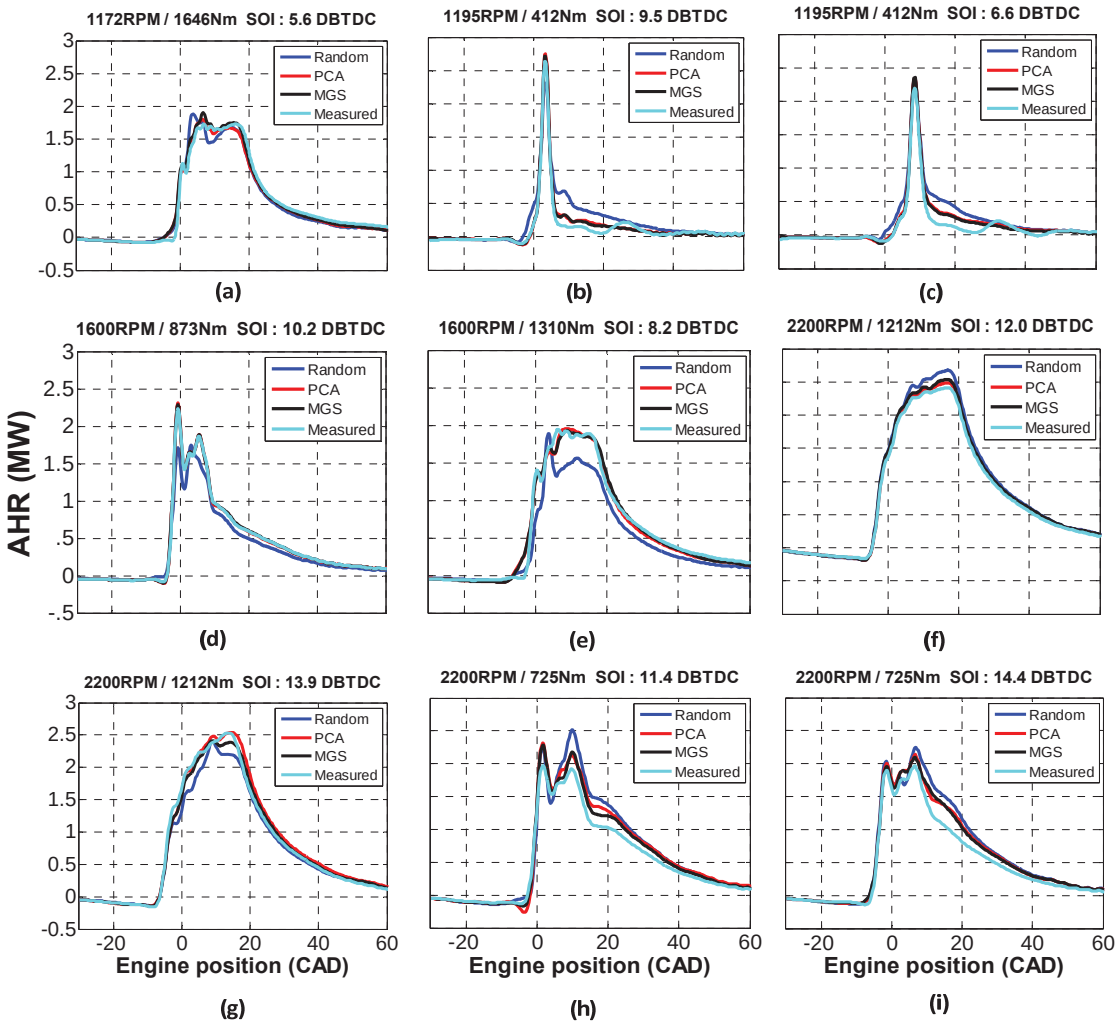

Figure 5.8: Comparison of AHR estimation results based on three *RW* selection methods

To further evaluate the performance of the RBFNN, its capability to tolerate additive noise was also examined. AHR is estimated based on the fixed networks determined from

the above training methods, then the input for the non-training data has additive noise included. To simulate the noise that an accelerometer sensor may encounter when the test condition changes, the frequency content of the noise was designed to be broadband. Figure 5.9 indicates the frequency spectrum of the accelerometer signal (top) and artificial noise (bottom). The peak amplitude of the artificial noise is set at approximately 7g with the peak amplitude of the measured accelerometer signal at 10 to 15 g. The signal to noise ratio in the 0-2000Hz frequency band is 17.5dB as computed by equation 5.5.

$$SNR(f) = 10 \cdot log_{10}(\frac{Gxx_{accel}(f)}{Gxx_{nosie}(f)}) \tag{5.5}$$

In equation 5.5, $Gxx_{accel}(f)$ and $Gxx_{noise}(f)$ are autopower spectrums for the accelerometer signal and the noise signal respectively.

Also, the location for intense noise content in the time domain was randomly selected to mimic possible noise formations. Figure 5.10 indicates three time domain noise signals that were added to the accelerometer signals of three different test conditions. Similarly, the noise signals that were added to other test conditions were distinctive from one another.

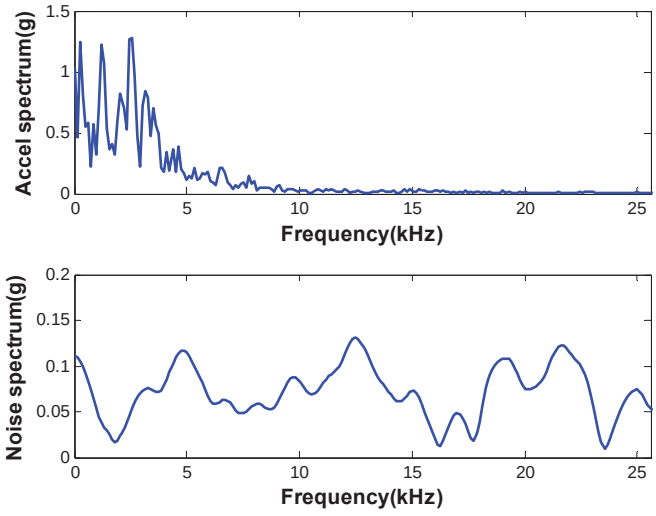

Figure 5.9: Frequency content for accelerometer signal and artificial noise

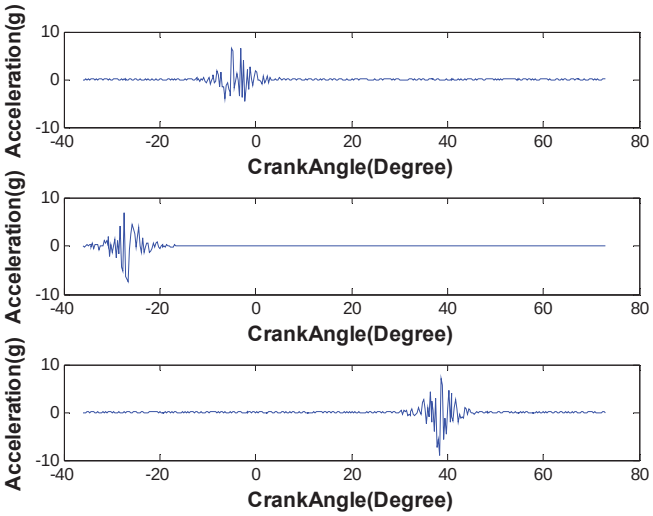

Figure 5.10: Artificial noise in time domain

The reconstruction results for combustion metrics with the noise added to the accelerometer signals are shown in Table 5.2. By comparing them with the results shown in Table 5.1, where no artificial noise was added to the accelerometer signals, the most obvious change occurs to PAA (the upward arrow in Table 5.2 indicates an increase in comparison to Table 5.1, the downward arrow indicates a decrease). So the amplitude metrics estimation is more sensitive to the additive noise. None of the combustion metrics estimation results deteriorate significantly when the accelerometer signal is contaminated by noise with a SNR at 17.5dB.

Table 5.2: Combustion metrics estimation results based on noise-added accelerometer signal

Combustion Parameter	***RW* selected based on MGS**		***RW* selected based on PCA**		***RW* selected randomly**	
	mean	**RMSE**	**mean**	**RMSE**	**mean**	**RMSE**
SOC (°CA)	0.5	0.9 (0.1↑)	0.4	0.6	0.7	1.0
CA50 (°CA)	1.6(0.1↑)	1.9	1.7(0.1↓)	1.8	1.6(0.2↓)	1.5(0.2↓)
PACL (°CA)	4.1(0.4↑)	4.0	4.3(0.2↓)	4.4(0.1↓)	4.3(0.4↓)	3.1(0.1↓)
PAA (%)	7.5(2↓)	6.7(0.3↓)	7.8(2.1↓)	6.1(0.2↓)	10.1(3.1↓)	8.2(1.6↑)

Figure 5.11 shows the comparison of computation time for weight vector selection between the PCA and MGS methods. The time used to select 100 weight vectors based on PCA method is 18 hours, while the time used to select 100 weight vectors based on the MGS method is just 5 seconds. The reason why PCA method requires so much more computation effort is that the PCA computation needs to run 600-k times to select the kth ($k > 1$) component of RW at the kth iteration. For 100 weight vectors selection, PCA computation runs 5000 times. Since the MGS and PCA methods show similar estimation accuracy, the MGS method is recommended for its lower computational requirements.

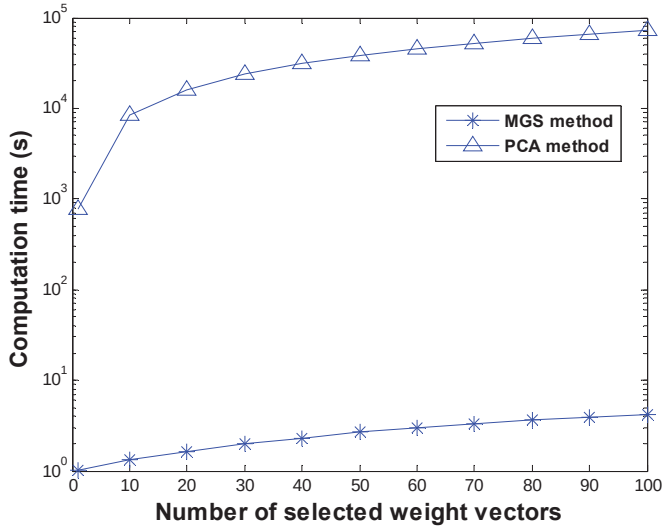

Figure 5.11: Computation time comparison between PCA and MGS methods

5.7 **Applicability**

By inputting the measured accelerometer signal to the trained RBFNN, the combustion metrics including SOC, PACL, PAA, and CA50 can be estimated as discussed and shown above. For the following, weight vectors in radial basis layer were selected via MGS method as it has been demonstrated to be superior to the other two methods in terms of accuracy and computational effort. Three of the four combustion metrics, SOC, PACL and CA50, are all correlated with combustion phasing and thus can be used as the feedback in a closed loop to control the start of injection. If CA50 is used as the combusting phasing feedback, a target (set point) CA50 meeting the NOx / BSFC target can be determined from a dynamometer calibration dependent upon the engine speed and load condition and stored in the engine control unit memory. The simplest strategy is then to adjust the start of injection (SOI) with the feedback error between the actual CA50 and target CA50 into a closed-loop controller.

The closed-loop control architecture is illustrated in Figure 5.12. RBFNN parameters (RW, m_1, LW, and m_2) and target CA50s are stored in the flash memory of the ECU. The computation of the CA50 based on the RBFNN and the on-line accelerometer signal is

implemented by the microcontroller. The desired SOI values related to fuel injection quantity and engine speed are stored as a map in the flash memory of the ECU as well. ΔCA50, the difference between the computed CA50 and the goal CA50, is used to correct the SOI. A driver stage that can activate the start-of-injection controlling mechanism in the actuators is triggered by the microcontroller [89]. By modifying the SOI value, the actual CA50 will be maintained close to the target CA50.

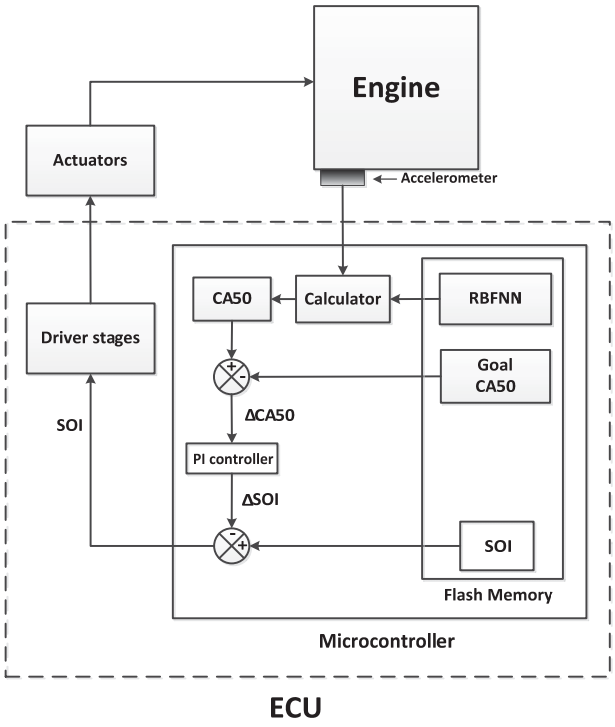

Figure 5.12: Start of injection closed-loop control with CA50 as the feedback

The storage of the four parameters of RBFNN, $RW(100 \times 423)$, $m_1(1 \times 1)$, $LW(423 \times 100)$, and $m_2(423 \times 1)$, will take 0.32MB memory space. If the Freescale MPC5676R microcontroller with a 6MB flash memory is employed, the storage for RBFNN parameters takes approximately 5% of the total memory. SPE (signal processing engine) in this microcontroller will implement the computation process to supply the corrected SOI. To evaluate the feasibility of the application of RBFNN for a real-time cycle-based combustion control, a comparison is made between the time used to implement a second

order IIR filter and the time used to implement the RBFNN. The reason why a second order IIR filter is taken as a reference is that most detection hardware chips are using the IIR filters. Based on the same computation environment on a PC, the time used for implementation of the RBFNN is 48 times the time used for implementation of a second order IIR filter. Wu, et al. [90] has examined the computation time of a second order IIR filter based on a Freescale MPC 5554 microcontroller (maximum operation frequency at 132MHz) and found it to be 3.12μs per data point. So for a windowed combustion cycle composed of 423 data points, the computation time is 0.0013s. By assuming that the RBFNN implementation time is 48 times the time used for implementation of a second order IIR filter on a microcontroller, the implementation of RBNFF based on a Frescale MPC 5554 will take 0.062s, which equals the time duration of one combustion cycle when engine speed is 1900RPM. If a more advanced microcontroller (Freescale MPC5676R with the maximum operating frequency at 360MHz) is employed, the computation time will be shortened. Although the exact computation time cannot be determined without the testing on the microcontroller, the rough estimation of the computation time indicates that the application of a RBFNN for a real-time cycle-based combustion control is promising.

5.8 **Summary**

The Radial Basis Function Neural Network introduces a non-linear mapping between the accelerometer signal and the Apparent Heat Release Rate for combustion metrics reconstruction. With the comparison of the estimation results from the three weight vector selection methods, it was shown that the weight vector selection based on Modified Gram-Schmidt and Principal Component Analysis lead to a higher accuracy of combustion metrics estimation than the random weight vector selection method. No significant difference was observed for the two methods based on the estimation results comparison. Moreover, the RBFNN was shown to have tolerance to additive noise with the signal noise ratio as high as 17.5dB with respect to the three weight vector selection methods discussed in this chapter. However, as the time cost for the 100 weight vectors

selection based on PCA method is 18 hours, computationally orders of magnitude higher than the MGC method, MGC method was selected for determination of the weight vectors. After being trained by twenty one test conditions, the fixed network with the weight vector selected based on the Modified Gram-Schmidt method can estimate the combustion phasing metrics, including SOC and CA50, across the sixty-six validation test conditions with the phasing error under 2 crank-angle degrees. The peak amplitude error is within 10%.

An online real-time application of the trained RBFNN has been proposed to supply the feedback for a closed-loop combustion phasing control. Future work will focus on the RBFNN training for a larger variety of test conditions, including low temperature combustion with pilot injection at high EGR rates, combustion with closely spaced pilot injections, etc., and applying the fixed network to different engine structures of the same type with the help of an adaptive filter design and feature extraction technique.

Chapter 6

Engine noise level estimation[1]

Diesel engines with the reduced exhaust and CO_2 emissions can better fulfill the restrictive emissions regulations. However, one drawback of the application of the diesel engine is the noise radiation due to the diesel combustion process. With the competitive nature of the automotive industry, the engine design needs to be perceived as both environmentally friendly and highly satisfactory to the customer. The acoustic comfort is an important consideration when the customer makes their purchasing decision and deserves significant attentions from the engine manufacturers.

In this chapter, the structural attenuation curves were evaluated. The algorithm built in a commercial noise meter was examined on the 1.9L TDI engine. An optimized attenuation curve that can better fit this engine was then pursued by applying both the averaging and cepstrum smoothing techniques. To further improve the engine noise estimation accuracy, a linear model was developed with the two components derived based on the engine speed and the in-cylinder pressure measurement respectively.

6.1 Experimental equipment

In this study, the tests were conducted on a 1.9L diesel engine equipped with a variable geometry turbocharger and a common rail direct injection system. Table 6.1 summarizes the specifications of the engine. The engine was directly connected to a dynamometer.

[1] The material contained in this chapter was submitted to "SAE International Journal of Engines" and the current status is "Peer review in process".

Table 6.1: The engine specifications

Specification	Value	unit
Cylinders	4	#
Displacement	1915	cc
Clearance Volume	30	cc
Bore	79.9	mm
Stroke	95.5	mm
Cylinder arrangement	4 inline	NA
Compression ratio	16.95	NA
Max Power	67 @ 3700 rpm	kW
Max Torque	210 @1900 rpm	Nm

PCB378B02 microphones were used to acquire the engine noise signal. The engine noise was computed by averaging the noise level from three microphones which were placed 1 meter away from the top, front, and left of the engine, the dynamometer was coupled to the right side of the engine. The in-cylinder pressure signal in cylinder 1 was acquired with a Kistler 6123A sensor. Data acquisition was performed with an advanced combustion acquisition and processing (ACAP) system with data processing and analysis being completed in Matlab. The experimental setup was laid out based on the guidance from the SAE J1074 standard.

6.2 Optimized structural attenuation curve

Based on the assumption that the engine structure response to the in-cylinder pressure excitation is linear, Austen and Priede [16] introduced the structural attenuation curve to estimate the engine noise level for any engine working condition. The structural attenuation is computed as the transfer path between the engine noise and the in-cylinder pressure one third octave band spectra. There are several structural attenuation curves, all with a similar shape [18, 17]. In this paper, the attenuation curve which is implemented in

the AVL combustion noise meter [91] is evaluated with its application on the 1.9L diesel test engine. With the in-cylinder pressure signal as the input, the structural attenuation function followed by the A weighting filter are applied to obtain the engine noise in dBA as output. Details about how to implement this algorithm are given in [17]. Figure 6.1 shows the estimated engine noise compared to the measured engine noise.

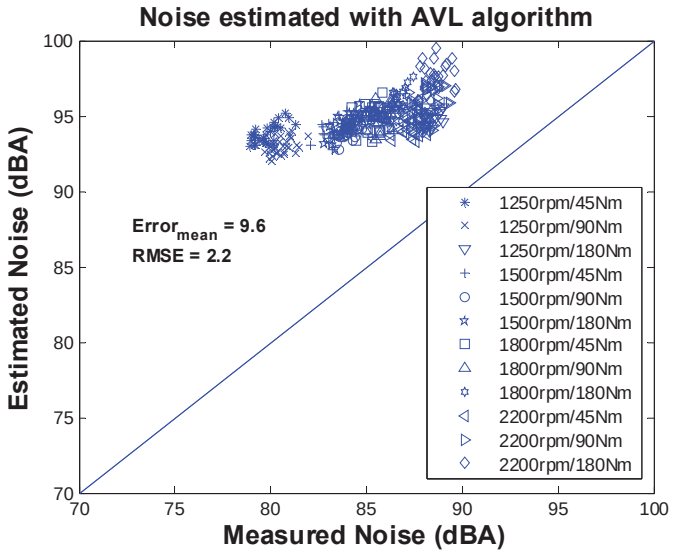

Figure 6.1: Engine noise level estimation with the attenuation curve in the AVL combustion noise meter

In Figure 6.1, with the increase of the measured engine noise, a similar trend can be seen on the estimated engine noise. However, the mean error between the estimated and measured cases is 9.6 dBA with the root mean error (RMSE) at 2.2 dBA. The significant disagreement between the measured and the estimated engine noise indicates that the standard structural attenuation curve cannot characterize the transfer path between the in-cylinder pressure excitation and the engine noise on the 1.9L TDI engine accurately. This implies that the standard structural attenuation curve implemented in the noise meter cannot be taken as a universal approach to estimate the noise radiated by any type of diesel engine.

To determine the optimized structural attenuation curve for the 1.9L diesel engine, an attempt is made by averaging the attenuation curves computed from multiple engine conditions. According to [92], Russell suggested to compute the attenuation curves based

on different speeds and load conditions (at least 20 cycles for each condition). The average of the attenuation curves is expected to provide a more accurate estimation of the engine noise. To examine the effects of this averaged attenuation curve, tests (Table 6.2) were conducted on the 1.9L diesel engine to supply the conditions at different speeds and loads. All the tests in Table 6.2 have the same main start of injection at 11DBTDC and the same pilot start of injection at 24 DBTCD. The rail pressure was consistently 750 Bar.

Table 6.2: Conducted test conditions

Test	1	2	3	4	5	6	7	8	9	10	11	12
Speed(rpm)	1250	1250	1250	1500	1500	1500	1800	1800	1800	2200	2200	2200
Torque(Nm)	45	90	180	45	90	180	45	90	180	45	90	180
Injection duration (ms)	0.44	0.61	0.74	0.37	0.53	0.72	0.45	0.60	0.76	0.42	0.59	0.75

Figure 6.2 shows an example of the attenuation curve determined from Test 11. Both cylinder pressure and engine noise are averaged through 85 cycles. As only the in-cylinder pressure in cylinder 1 is measured in this paper, both the microphone signal and the in-cylinder pressure signal are windowed around the combustion event in cylinder 1 so that the engine noise due to the combustion events in other cylinders will be minimized in the analysis. For the reason that the data acquisition is time based not crank angle based, the window length is selected to be from 266 samples left of the top dead center (TDC) of cylinder 1 to 532 samples right of the TDC. The sample based window also provides convenience for the averaging computation of the attenuation curves from different engine conditions because the crank angle based window will introduce inconsistent data block size for different engine speed conditions. For each condition, as shown in Figure 6.2, the attenuation curve is computed by subtracting the engine noise spectrum from the cylinder pressure spectrum. At the frequency around 7 kHz, an amplitude peak of the in-cylinder pressure spectrum can be seen. This peak is caused by

the abrupt rise of the in-cylinder pressure at the beginning of the combustion, which incurs the high frequency resonant oscillation of the gas in the combustion chamber [74].

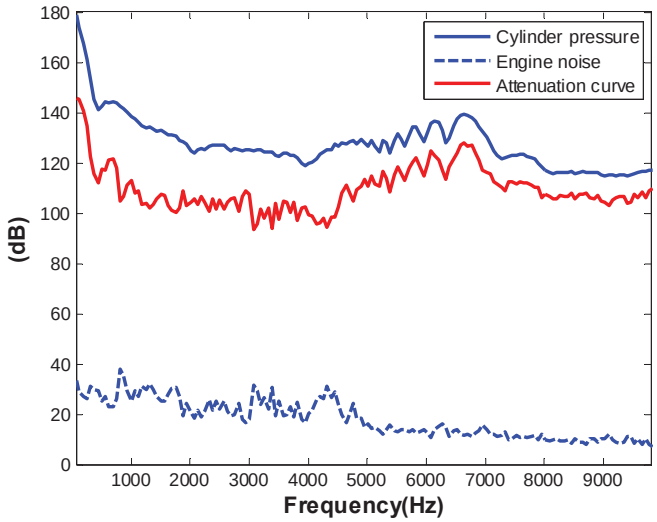

Figure 6.2: Structural attenuation curve computation example (Test11)

The attenuation curves for the other conditions (Table 6.2) are computed with the same procedure as for Test 11 in Figure 6.2. They are averaged to achieve one attenuation curve which is expected to be robust enough to work for all the test conditions. For any operating condition, the estimated engine noise can be reached by subtracting the averaged attenuation curve from the in-cylinder pressure spectrum. Figure 6.3 shows the engine noise estimation results based on the averaged attenuation curve.

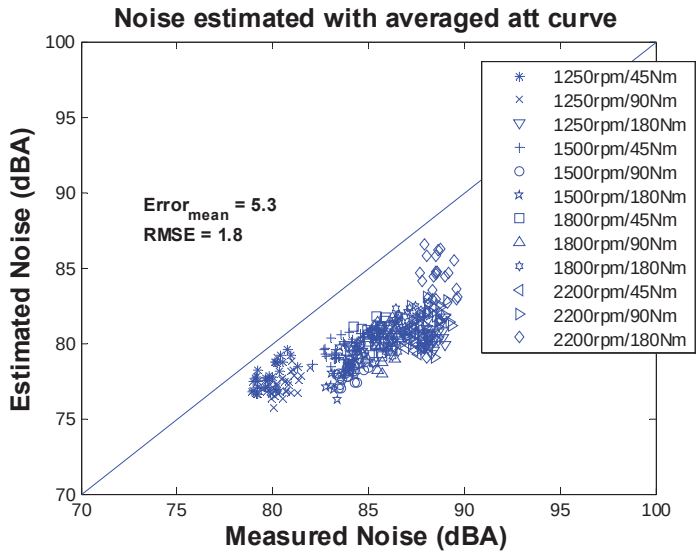

Figure 6.3: Engine noise level estimation based on the averaged attenuation curve

In comparison to the results in Figure 6.1, the estimation error of the engine noise based on the averaged attenuation curve decreases. However, the estimated engine noise is lower than the measured one with a mean error of 5.3dBA and the RMSE of 1.8dBA. Although the averaging algorithm minimizes the variation of the attenuation curves of different conditions, it does not always lead to a good result because the averaging is performed in the complex domain. For example, assuming that the value for one attenuation curve is $5 + i$ and and a value of $-5 - i$ for another attenuation curve at 500Hz, the average of the two values at 500Hz will be 0 and the log scale value will be infinity. This will result in a significant error for the engine noise estimation. Even if the real situation may not be as extreme as the scenario described above, the averaging process is not a reliable approach to eliminate the variation among the attenuation curves unless these curves are extremely close to one another with respect to both amplitude and phase.

To find the optimized structural attenuation curve which has a better robustness for various engine conditions, a cepstrum smoothing technique is used in this paper. Kim [60] introduced the cepstrum smoothing technique to reduce the transfer path variability among the engine structures of the same class. In this paper, this technique is applied to

reduce the variability of the attenuation curves among different engine conditions. Cepstrum is defined as the inverse Fourier transform of the logarithm of the spectrum of a time domain signal [93]. The cepstrum equivalent of the frequency domain, quefrency, is found by reversing the first four letters of frequency. Cepstrum can be presented as Equation 6.1:

$$C(\tau) = F^{-1}(\log\,(Y(\omega))) \tag{6.1}$$

Where $$\log\big(Y(\omega)\big) = \log(|Y(\omega)|) + j\ arg(Y(\omega)) \tag{6.2}$$

$Y(\omega)$ is the spectrum of signal $y(t)$. However, before applying logarithm computation, both magnitude and phase of $Y(\omega)$ need to be continuous. Magnitude is always continuous. The phase function is not continuous because the phase value $arg(Y(\omega))$ bounces between $-\pi$ and $+\pi$, and thus is discontinuous at $\pm\pi$. An unwrapping process is used to convert the phase function into a continuous function [60].

The cepstrum smoothing is implemented by applying a low pass filter in the quefrency domain (a window around the zero quefrency), which is called “liftering”. The magnitude and phase of the attenuation curve are smoothed by liftering both the in-cylinder pressure and the engine noise under a particular engine condition. A shorter window applied for liftering can provide a smoother result. However, when the curve becomes smoother, more local information will be lost and significant engine noise estimation error may result. More details about the effects of window length and shape on the smoothing results can be found in [60]. In this paper, the lifetering window used was rectangular in shape with a length of 100 points corresponding to the data length of 799. The schematic illustration of the smoothing process is given is Figure 6.4.

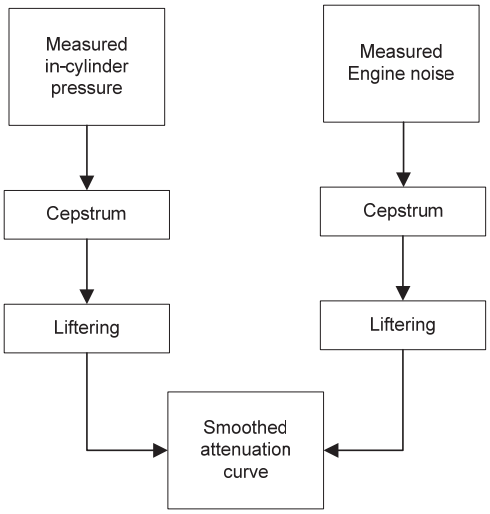

Figure 6.4: Attenuation curve smoothing process

After the in-cylinder pressure and the engine noise are liftered and transformed back to the frequency domain, the smoothed attenuation curve is estimated through the process illustrated in Figure 6.2. The attenuation curve computed from Test 12 was taken as the raw curve based on which the smoothing process was applied. Figure 6.5 shows the comparison of the attenuation curves studied in this chapter. The curves in Figure 6.5 follow a similar trend with the curves descending within the low frequency band. After the decline, an amplitude increase can be seen. For the AVL attenuation curve, the curve amplitude keeps a monotone increasing through to 10 kHz. For the other curves, an amplitude peak can be observed around 6500 Hz followed by a slight amplitude decrease up until 10 kHz. The AVL attenuation curve is the smoothest and is thus lacking many local details that are particular to each operating condition. The accuracy will be severely reduced when the curve becomes too smooth. Therefore, although the smoothed curve may have better adaptability, a good balance needs to be achieved between the robustness and the estimation accuracy. Also, as the AVL attenuation curve has an opposite trend for the frequency band higher than 6.5 kHz, significant errors can be observed in the engine noise estimation result in Figure 6.1.

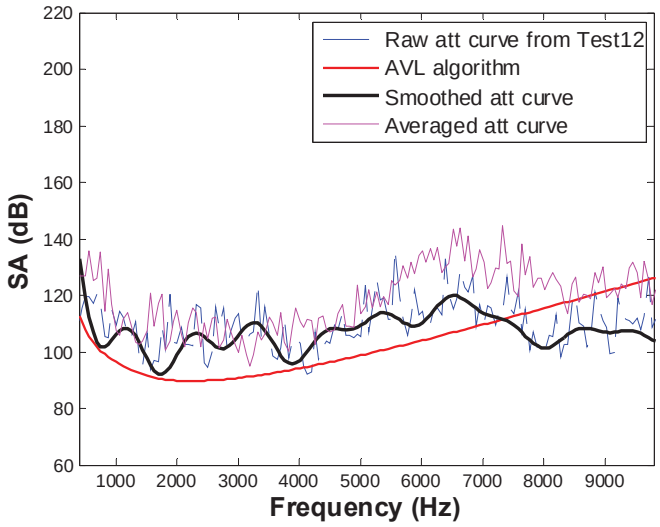

Figure 6.5: Comparison of the attenuation curves studied in this chapter

The smoothed attenuation curve in Figure 6.5 captures the trend of the raw curve without including some oscillations that vary with engine conditions. In comparison to the AVL curve, the smoothed curve performs better in extracting the shape characteristics of the raw curve. The smoothed curve may not lead to a highly accurate estimation result for any particular engine condition since it loses some local details. However, when it is applied to multiple engine conditions, the improved overall engine noise estimation performance demonstrates the improved robustness of the smoothed attenuation curve. Figure 6.6 shows the engine noise estimation results based on the smoothed attenuation curve with the raw curve computed from Test 12. The mean error is reduced to 1.8 dBA with the decreased RMSE at 1.6 dBA. The highest estimation error occurs for Test 1 and Test 2. However, the improvement of the estimation results is obvious when comparing to the results based on the AVL attenuation curve and the averaged attenuation curve (Figures 6.1 and 6.3).

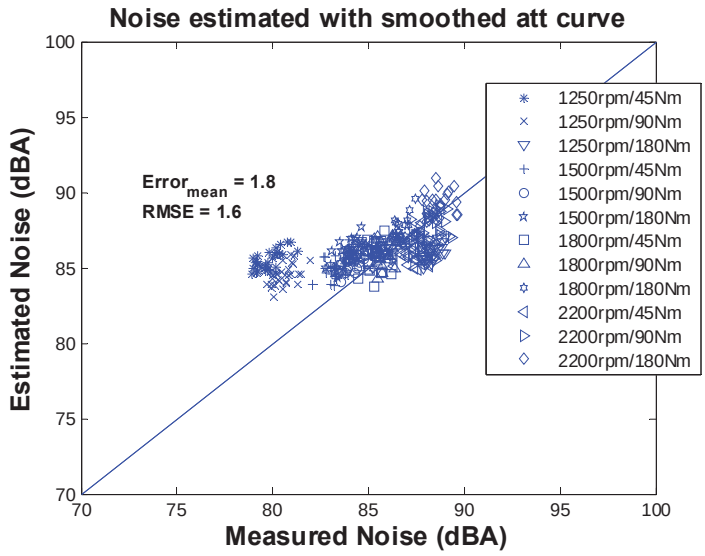

Figure 6.6: Engine noise level estimation based on the averaged attenuation curve (the raw attenuation curve is computed from Test12)

The raw attenuation curve does not have to be computed based on Test 12. Figure 6.7 shows the results when the cepstrum smoothing process is applied to the attenuation curves obtained from Test 5 (1500rpm/90Nm), Test 6 (1500rpm/180Nm), Test 7 (1800rpm/45Nm), and Test 10 (2200rpm/45Nm). The averaged estimation errors are all near 2 dBA with the RMSE near 1.5dBA. No significant difference can be seen when the condition that is used to compute the raw attenuation curve changes. This implies that it can be concluded that the smoothed attenuation curve determination does not depend on any specific engine condition. This implies that a large effort does not need to be made to identify the ideal engine conditions to estimate an optimal smoothed attenuation curve.

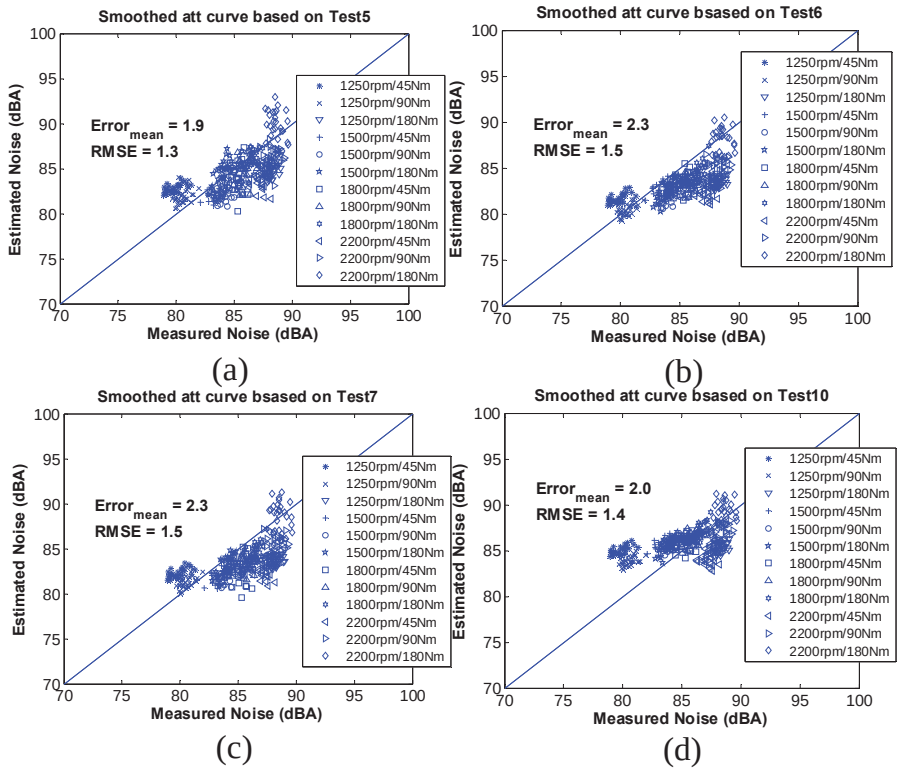

Figure 6.7: Engine noise level estimation based on the smoothed attenuation curve, the raw attenuation curve is computed from: (a) Test5; (b) Test6; (c) Test7; (d) Test10.

In summary, the AVL attenuation curve introduces the maximum error to the engine noise estimation for the 1.9L TDI engine among the three attenuation curves studied in this chapter. The averaged attenuation curve improves the estimation performance. However, the best estimation results are introduced by the cepstrum smoothed attenuation curve. More than the improved estimation accuracy, the smoothed attenuation curve computation neither relies on any specific engine operational condition nor, on the averaged attenuation curve that depends on multiple engine conditions which must include different speeds and loads. The smoothed attenuation curve computation is characterized by a high efficiency as well.

6.3 A linear model for engine noise estimation

The attenuation curves which can be used to estimate the engine noise level were presented in the above section. The optimized curve provided an estimation result with an approximate averaged error of 2dBA. Another approach that can provide a more accurate estimation result is proposed below.

In Tousignant's work [75], engine speed was taken as a deterministic factor for the total engine noise level and was considered as one excitation source in their model. However, how the engine speed contributes to the total engine noise was not presented. To validate that the engine speed is related to the engine noise level, Figure 6.8 plots the engine noise versus the engine speed to reveal the relation between the two.

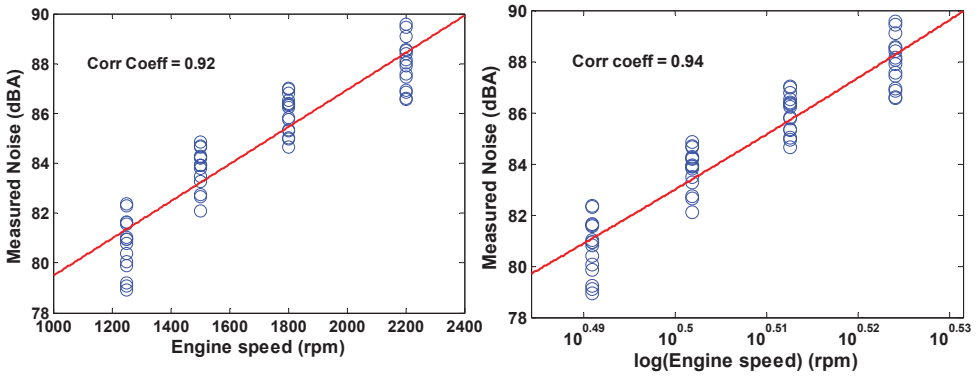

Figure 6.8: Engine noise variations with changes of engine speed

An obvious linear dependency can be seen between the measured engine noise level and the engine speed. Along with the engine speed increase, the engine noise increases proportionally. The linear correlation coefficient is as high as 92.9% when the raw engine speed is evaluated, Figure 6.8 (b). The evaluation of linear dependency between the engine noise and the logarithmic engine speed is also made in Figure 6.8 (a) since the engine noise in dBA is in logarithmic scale. The linear correlation coefficient increases to 94.2% and thus indicates a better linear correlation. Depending on these observations, a linear model can be created to estimate the engine noise level based on the logarithmic engine speed.

In this chapter, all the tests in Table 6.2 can be distinguished by the main injection durations. This implies that other combustion-related components that can reflect the injection parameter variations should be incorporated into the linear model to improve the engine noise level estimation accuracy. Torregrosa et al. [75] reached the same conclusion and developed two more combustion-related components based on the decomposed in-cylinder pressure. In Torregarosa's work, the in-cylinder pressure trace was decomposed into pseudo-motored, combustion, and resonance pressure signals. Only the combustion and resonance signals were considered to create two more components which were incorporated into a linear model to estimate the engine noise. The pseudo-motored pressure was used to normalize the two components to turn them into dimensionless quantities. However, when combustion occurs in the cylinder chamber, not only the combustion and resonance pressures but the pseudo-motor pressure forces operate on the chamber wall and introduce forces through the mechanical systems to the engine block. In this chapter, the non-decomposed in-cylinder pressure is used to derive a combustion related component for the linear model. This component is defined as:

$$C_1 = \int p^2 dt \tag{6.3}$$

Where p is the measured in-cylinder pressure in 10^9Pa. C_1, in a physical sense, can be considered as the energy propagation of the in-cylinder pressure which will cause the engine block vibration and thus introduce the engine noise.

Together with the engine speed component:

$$C_2 = \log(n) \tag{6.4}$$

Where n is the engine speed in rpm.

A multiple regression with the two components, C_1 and C_2, is created to output the estimated engine noise (*EN*):

$$EN = k_0 + k_1 C_1 + k_2 C_2 \tag{6.5}$$

The coefficient k_0, k_1, and k_2, are estimated and presented in Table 6.3:

Table 6.3: Coefficients for the linear model with two components

k_0(dBA)	k_1(dBA/10^{18}Pa)	k_2(dBA/rpm)
-19.55	32.00	0.49

By applying this linear model to the tests given in Table 6.2, the noise radiated from the 1.9L diesel engine is estimated. Figure 6.9 shows the estimation results. For each test condition, 30 cycles are examined (the same as Figures 6.1, 6.3, 6.6, and 6.7). The averaged estimation error decreases to 0.5 dBA with a reduced RMSE of 0.3 dBA. A significant estimation improvement can be observed in comparison to the estimation results based on the optimized attenuation curves.

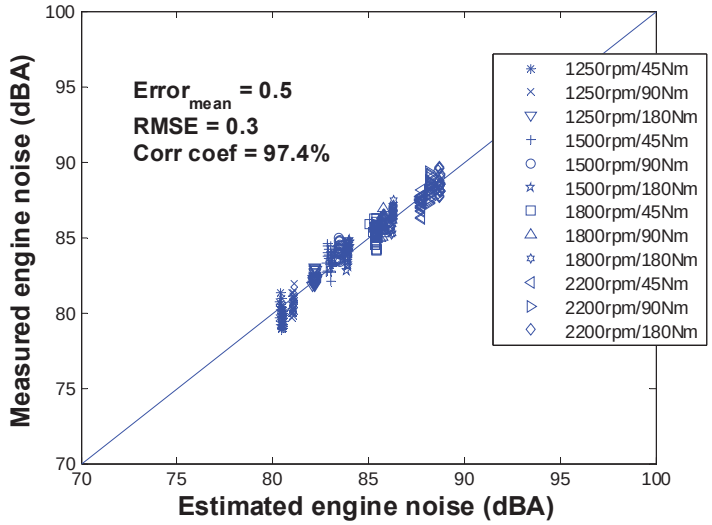

Figure 6.9: Engine noise estimation based on the linear model

6.4 Conclusion

The established engine noise estimation approach based on the structural attenuation curve was evaluated on a 1.9L TDI diesel engine. The attenuation curve from a commercial combustion noise meter was first investigated. The result showed a significant difference between the estimated and the measured engine noise with a mean difference of 9.6 dBA and an RMSE of 2.2 dBA. To find the "personalized" attenuation

curve that can characterize the transfer path between the in-cylinder pressure signal and the overall engine noise level on the 1.9L TDI engine, the attenuation curve was computed based on the measurement of in-cylinder pressure and engine noise.

After estimating the specific attenuation curve for this engine, optimization was pursued by two methods, averaging the attenuation curves from different engine operating conditions and cepstrum smoothing the attenuation curve. Results show that the cepstrum smoothed attenuation curve provides a more accurate estimation with the mean error of 1.8dBA (RSME of 1.6dBA), in comparison to the averaged attenuation curve with the mean error of 5.3dBA (RSME of 1.8 dBA). Moreover, the cepstrum smoothed attenuation curve can be obtained based on only one engine operating condition. No significant difference on the estimation result was observed when an alternative engine operating condition was used. So less work about data acquisition and signal processing is needed to achieve the cepstrum smoothed curve.

Even with the optimized attenuation curve, the high dispersion of the results with respect to different engine conditions evidenced its limited robustness (especially for Test 1 and Test 2). To pursue higher estimation accuracy, a model based on a concept different from the attenuation curve was developed. A linear model was developed based on two components, C_1, representative of the in-cylinder pressure energy propagation, and C_2, associated with the engine speed. Through the multiple regression analysis, the coefficients of the two components were estimated. With the new model, results show that the averaged estimation error is reduced to 0.5dBA with a decreased RMSE of 0.3dBA. Obvious improvement can be seen based on this linear model. Furthermore, this linear model has a good adaptive potential and can be optimized by incorporating other components which are related to the engine noise if higher estimation accuracy is required.

Chapter 7

Summary, conclusions and recommendations for future study[1]

7.1 Summary and Conclusions

7.1.1 Combustion metrics estimation based on the vibration signature

The vibration signatures acquired through block-mounted accelerometers were used to reconstruct the in-cylinder pressure waveform and the apparent heat release rate waveform. Combustion metrics including PPCL, CA50, SOC, PACL, PPA, and PAA were derived from the reconstructed in-cylinder pressure waveform or the apparent heat release rate waveforms. Success of estimation of the combustion metrics depends on the development of a robust transfer path.

The study in this dissertation started from the evaluation of the single-input single-output frequency response function based on the optimal accelerometer. The optimal single accelerometer channel used to provide the vibration signal was selected based on the coherence analysis between the in-cylinder pressure signal and the accelerometer signals. The accelerometer channel that is characterized with the highest coherence value which indicates the strongest correlation between the in-cylinder pressure and the accelerometer

[1]The material contained in this section is planned for submission as part of a journal article and/or conference paper in the future.

signal is considered as optimal. The application of FRF (computed through the optimal accelerometer channel based on one condition) to the engine operating conditions with varied SOIs and loads showed that the FRF computed from one operating condition needs to be adapted for its application for other engine conditions.

Then an adaptation process was explored to adapt the SISO FRF from one engine operating condition to engine operating conditions with varied SOIs and loads. This research found that adaptation of the lowest frequency band of FRF, the DC offset and the 121Hz harmonics, has more than 95% of the original PPA and MAPE errors decreased. The DC offset was compensated by a gain which is dependent upon engine load. This gain was premeasured and can be taken as calibration factor for use of compensation. The 121Hz harmonics was adapted through a computational optimization algorithm, particle swarm optimization, with the objective function created based on the ratio of specific heats of both the compression and expansion strokes. Results showed that this adaptation process can significantly improve the robustness of FRF over the SOI and loads variations. However, its applicability to the speed changes needs adaptation of more FRF harmonics which will cause the increase of computation time and storage cost and makes it an obstacle for online application.

Following the SISO methods, a multiple-input single-output model for the FRF application was investigated to further improve the robustness of FRF. First, the data from all the twenty one accelerometer channels were utilized to recover the in-cylinder pressure. Twenty one FRFs which correspond to the twenty one channels were computed and then utilized to output twenty one estimated in-cylinder pressure curves. Then the principal component analysis was applied to all the obtained pressure curves to extract the most representative information. After the PCA process, however, the offset of the extracted in-cylinder pressure needs to be further compensated. An iterative compensation process was then developed with the ratio of the specific heats at the compression stroke as the objective function. A significant improvement of estimation result for the conditions with varied SOIs and loads can be observed with the in-cylinder

pressure obtained based on MISO model and manipulated by PCA process followed by the offset compensation process. However, the usage of twenty one input channels make this method unrealistic for online combustion metrics reconstruction. As a result, a process that reduced the number of input channels was developed with the purpose of utilizing fewer numbers of accelerometers and providing accurate estimation results from the combustion metrics. Threshold values from three combustion metrics, PPA, PPCL, and SPA, which can extract the features of the in-cylinder pressure curve for the control of combustion process, were employed as the standard to select the qualified minimum-number of input channels. Finally, two channels were determined as the input channels for the MISO model based on which the estimation results were above the thresholds. This fixed MISO (two-input single-output) model was applied to additional conditions with variations of SOI, load, and speed. It showed that estimation results were improved based on the fixed MISO model in comparison to the SISO model.

Neural network as a nonlinear modeling method was developed and applied to estimate the apparent heat release rate waveform with the single channel accelerometer signal (selected based on the coherence analysis) as the input. Radial basis function network was selected since it is a forward neural network with the advantage of being trained with a more straightforward approach in comparison to the back-propagation algorithms. This dissertation focused on the selection of neural network structure and training method among the three proposed methods to provide a network with the best accuracy and efficiency for apparent heat release rate estimation. Results showed that the Modified Gram-Schmidt method and PCA method can introduce better estimations than the random selection method for the apparent heat release rate estimation. Moreover, Modified Gram-Schmidt method can complete the 100 weighing vectors selection with 1/100 of the computation time that is needed for the PCA method. So the Modified Gram-Schmidt method is determined to be the optimal method for selecting the weighting vector of the radial basis function neural network.

7.1.2 Engine noise level estimation based on the in-cylinder pressure signal

Engine noise level as a deterministic factor of acoustical emission on a vehicle requires significant attention from the engine manufacturers. The availability of on-board load cell in-cylinder pressure sensor on current TDI engine [28] makes it possible to estimate the engine noise level based on the in-cylinder pressure signal. Structural attenuation curve was applied to the 1.9L TDI diesel engine to estimate the engine noise level. Results showed that this attenuation curve built in a commercial combustion noise meter introduced a 9.6 dBA estimation error on the 1.9L TDI engine. So an optimization process of the attenuation curve was performed through two proposed algorithms, averaging and cepstral smoothing. Results show that the cepstral-smoothed attenuation curve was considered as the optimal transfer path between the in-cylinder pressure signal and the engine noise level.

Another simple linear model was established based on the multiple regression approach with the engine speed and the measured in-cylinder pressure signal as the components.

Conclusions from this work are:

- With the adaptation process added to the SISO FRF model, the PPCLE is improved as great as 1.3 degree, the improvements for PPAE are all above 90% (normalized by the PPAE value from raw SISO FRF model), and the averaged MAPE improvement is 75% (normalized by the MAPE value from raw SISO FRF model).

- Based on the MISO (two-input single-output) FRF model in comparison to the SISO FRF model, improvement was be obtained for 75% of the tests (Tables 3.2 and 4.3) with the evaluation based on PPCLE, 88% of the tests with the evaluation based on PPAE, and 94% of the tests with the evaluation based on MAPE. The improvements for PPAE and MAPE are as high as 98% (normalized

by the MAPE from SISO FRF model). The improvement for PPCLE is as great as 7.8 degree.

- Modified Gram-Schmidt method has been confirmed to be the optimal weightvector selecting method for the radial basis function network modeled between the accelerometer signal and the AHR. Combustion metrics were estimated with the SOC mean error at 0.5 degrees and RMSE at 0.8 degrees, CA50 mean error at 1.5 degrees and RMSE at 1.9 degrees, PACL mean error at 3.7 degrees and RMSE at 4.0 degrees, and PPA mean error at 9.5% and RMSE at 7.0%.
- It was found that the attenuation curve obtained by averaging the attenuation curves of different operating conditions can introduce a better estimation result (error of 5.3 dBA) than the results (error of 9.6 dBA) based on the attenuation curve in AVL combustion noise meter. Application of cepstrum smoothing technique on the computed attenuation curve further improved the estimation results (error of 2 dBA) in comparison to the averaged attenuation curve.Results showed that the proposed linear model can introduce more accurate engine level estimation results than the attenuation curve approach. The estimation error is as low as 0.5 dBA with the RMSE of 0.3 dBA.

7.2 Recommendations for future work

Based on the explorations in this dissertation, the following recommendations are given for future work:

- To adapt the SISO FRF for the engine operating conditions with speed variations, more FRF harmonics need to be manipulated. However, simultaneous adaptation of more than one harmonic increases the computational time. So the working efficiency of the particle swarm optimization adaptation algorithm should be improved or an algorithm other than the particle swarm optimization should be investigated.

- MISO model was confirmed to improve the performance of FRFs for combustion metrics estimation. The future signal processing work can focus on the FRF matrix to develop a robust FRF matrix that can output the estimated in-cylinder pressure without needing the assistance from PCA and offset compensation processes. Then shorter time would be needed for the online combustion metrics estimation.
- Radial basis function neural network led to the best combustion metrics estimation based on the results in this work. However, the training and application of the network were implemented only based on one engine. The results of applying the trained network based on one engine to another engine structure of the same type need to be evaluated. The vibration signal on another engine may vary due to the assembling variation even under the same engine operating condition. Therefore, adaptation process should be designed to assist the trained network to make it work for different engine structures.
- The accelerometers mounting on the engine block are measuring the vibration caused not only by in-cylinder pressure but other sources including piston slap, valve train dynamics, etc. So the pre-processing of the accelerometer signal to separate the component which originated from the source of the most interest (in-cylinder pressure signal in this dissertation) would be helpful in improving the robustness of FRF. Blind source separation as a method to separate the source signals from a set of mixed signals is recommended.
- The transfer path modeled in this dissertation only took the engine vibration signal as the input. It is possible that additional signals that related to the combustion events used as the inputs, more accurate the combustion metrics estimation results will be. So a hybrid of input signals, including the crank-shaft speed and vibration signal, ion current signal and vibration signal, etc., can be utilized as the input parameters to model the transfer path.

Reference

[1] Jia, Libin, et al. "Accelerometer-Based Combustion Metrics Reconstruction with Radial Basis Function Neural Network for a 9 L Diesel Engine." *Journal of Engineering for Gas Turbines and Power* 136.3 (2014): 031507.

[2] Charlton, S., "Developing Diesel engine to Meet Ultra-low Emission Standards," SAE Technical Paper 2005-01-3628, 2005, doi:10.4271/2005-01-3628.

[3] DOC/EE-0957, Fuel Economy Guide Model year 2014, 2014.

[4] Farshchi, Mohammed, Christie-Joy Brodrick, and H. A. Dwyer. "Dynamometer testing of a heavy duty diesel engine equipped with a urea-SCR system." SAE Technical Paper 2001-01-0516, 2001,doi:10.4271/2001-01-0516.

[5] Yanowitz J, Mccormick RL, Graboski MS. In-Use Emissions from Heavy-Duty Diesel Vehicles. *Environmental Science & Technology* 2000;34:729-740, 2000.

[6] Conway, Raymond, et al. "NOx and PM reduction using combined SCR and DPF technology in heavy-duty diesel applications." *Fuel* 2009 (2005): 32-0129.

[7] Schnorbus, T., Pischinger, S., Körfer, T., Lamping, M. et al., "Diesel Combustion Control with Closed-loop Control of the Injection Strategy," SAE Technical Paper 2008-01-0651, 2008, doi:10.4271/2008-01-0651.

[8] Lee, S., Lee, J., Lee, S., Kim, D. et al., "Study on Reduction of Diesel Engine Out Emission through Closed Loop Control based on theIn-Cylinder Pressure with EGR Model," SAE Technical Paper 2013-01-0322, 2013, doi:10.4271/2013-01-0322.

[9] Franz, J., Schwarz, F., Guenthner, M., Reissing, J. et al., “Closed Loop Control of an HCCI Multi-Cylinder Engine and Corresponding Adaptation Strategies," SAE Technical Paper 2009-24-0079, 2009, doi:10.4271/2009-24-0079.

[10] Yanowitz J, Mccormick RL, Graboski MS. In-Use Emissions from Heavy-Duty Diesel Vehicles. *Environmental Science & Technology* 2000;34:729-740, 2000.

[11] Amann, C., 1985, “Cylinder-Pressure Measurement and Its Use in Engine Research,” SAE Paper No. 852067.

[12] Powell, B. K., Lawson, G. P., and Hogh, G., 1987, “Advanced Real Time Powertrain System Analysis,” ASME Paper No. 87-ICE-46.

[13] Wildhaber, Shawn Nicholas. "Impact of combustion phasing on energy and availability distributions of an internal combustion engine." (2011).

[14] Heywood, J. B. (1988), Internal Combustion Engine Fundamentals, New York: McGraw-Hill.

[15] Aradl, A., & Ryan, T. (1995). Cetane Effect on Diesel Ignition Delay Times Measured in a Constant Volume Combustion Apparatus. SAE 952352 .

[16] Austen, A. and Priede, T., "Origins OF Diesel Engine Noise," SAE Technical Paper 590127, 1959, doi:10.4271/590127.

[17] Shahlari, A., Hocking, C., Kurtz, E., and Ghandhi, J., "Comparison of Compression Ignition Engine Noise Metrics in Low-Temperature Combustion Regimes," *SAE Int. J. Engines* 6(1):541-552, 2013, doi:10.4271/2013-01-1659.

[18] Torregrosa, A. J., et al. "Combustion noise level assessment in direct injection Diesel engines by means of in-cylinder pressure components." *Measurement Science and Technology* 18.7 (2007): 2131.

[19] Yoon, M., Lee, K., Sunwoo, M., and Oh, B., "Cylinder pressure Based Combustion Phasing Control of a CRDI Diesel Engine," SAE Technical Paper 2007-01-0772, 2007, doi:10.4271/2007-01-0772.

[20] Yang, Z., Stobart, R., and Winward, E., "Online Adjustment of Start of Injection and Fuel Rail Pressure Based on Combustion Process Parameters of Diesel Engine," SAE Technical Paper 2013-01-0315, 2013, doi:10.4271/2013-01-0315.

[21] Huang, Y., Yang, F., Ouyang, M., Chen, L. et al., "Optimal Feedback Control with in-Cylinder Pressure Sensor under Engine Start Conditions," SAE Technical Paper 2011-01-1422, 2011, doi:10.4271/2011-01-1422.

[22] Taglialatela, F., et al. "Determination of combustion parameters using engine crankshaft speed." *Mechanical Systems and Signal Processing* 38.2 (2013): 628-633.

[23] Polonowski, Christopher J., Vivek K. Mather, and Jeffrey D. Naer. "Accelerometer based sensing of combustion in a high speed HPCR diesel engine." *SAE Paper* (2007): 01-0972.

[24] Alt, N., Wiehagen, N., Steffens, C., and Heuer, S., "Comprehensive Combustion Noise Optimization," SAE Technical Paper 2001-01-1510, 2001, doi:10.4271/2001-01-1510.

[25] Gaikwad, A., Mahale, P., and Raju, S., "Noise Assessment of Diesel Engines," SAE Technical Paper 2007-26-038, 2007, doi:10.4271/2007-26-038.

[26] Wang, S., Chalu, C., and Gautier, F., “Optimization of Combustion Noise of Modern Diesel Engines for Passenger Cars," SAE Technical Paper 2007-01-2379, 2007, doi:10.4271/2007-01-2379.

[27] Lee, N., Park, W., Ruotolo, R., and Trombley, D., "NVH Development of EU5 2.0L and 2.2L Diesel Engine," SAE Technical Paper 2011-01-0932, 2011, doi:10.4271/2011-01-0932.

[28] Volkswagen of America, Inc. (2008). 2.0 Liter TDI Common Rail BIN5 ULEV Engine, self-study program 826803. Volkswagen Academy.

[29] Moro, D., N. Cavina, and F. Ponti. "In-cylinder pressure reconstruction based on instantaneous engine speed signal." *Journal of engineering for gas turbines and power* 124.1 (2002): 220-225.

[30] F.T. Connolly, A.E. Yaggle. “Modeling and identification of the combustion pressure process in internal combustion engines.” *Mechanical Systems and Signal Processing*, 8 (1) (1994), pp. 1–19.

[31] Shiao, Yaojung, and John J. Moskwa. "Cylinder pressure and combustion heat release estimation for SI engine diagnostics using nonlinear sliding observers."*Control Systems Technology, IEEE Transactions on* 3.1 (1995): 70-78.

[32] S. Saraswati, S. Chand, Reconstruction of cylinder pressure for SI engine using recurrent neural network, Neural Comput. Appl. 19 (2010) 935–944.

[33] F. Gu, P.J. Jacob, A.D. Ball, A RBF neural network model for cylinder pressure reconstruction in internal combustion engines, IEE Colloquium on Modelling and Signal Processing for Fault Diagnosis, Digest No: 1996/260, 1996.

[34] F. Liu, G.A.J. Amaratunga, N. Collings, A. Soliman, An Experimental Study on Engine Dynamics Model Based In-Cylinder Pressure Estimation, SAE Paper No. 2012-01-0896, 2012.

[35] Taraza, Dinu, Naeim A. Henein, and Walter Bryzik. "Determination of the Gas-Pressure Torque of a Multicylinder Engine from Measurements of the Crankshaft's Speed Variation." *SAE transactions* 107.3 (1998): 294-302.

[36] Rizzoni, Giorgio. "Estimate of indicated torque from crankshaft speed fluctuations: A model for the dynamics of the IC engine." *Vehicular Technology, IEEE Transactions on* 38.3 (1989): 168-179.

[37] Liu, F., Amaratunga, G., Collings, N., and Soliman, A., “An Experimental Study on Engine Dynamics Model Based In-Cylinder Pressure Estimation," SAE Technical Paper 2012-01-0896, 2012, doi:10.4271/2012-01-0896.

[38] Yoshiyama, S., Tomita, E., and Hamamoto, Y., "Fundamental Study on Combustion Diagnostics Using a Spark Plug an Ion Probe," SAE Technical Paper 2000-01-2828, 2000, doi:10.4271/2000-01-2828.

[39] Hellring, Magnus, and Ulf Holmberg. "An ion current based peak-finding algorithm for pressure peak position estimation." *SAE Technical Paper* (2000): 01-2829.

[40] Martychenko, A. A., et al. "A Study on the Possibility of Estimation of In-Cylinder Pressure by Means of Measurement of spark Gap Breakdown Voltage." *SAE paper* (1999): 01-1115.

[41] Hellring, Magnus, and Ulf Holmberg. "An ion current based peak-finding algorithm for pressure peak position estimation." *SAE Technical Paper* (2000): 01-2829.

[42] Kumar, Davinder, et al. "An Ionization Current based Cylinder Gas Pressure Estimation for Knock Detection and Control in a Single Cylinder SI Engine."*Internal Combustion Engines* 2013: 04-08.

[43] Yoshiyama, Sadami, Eiji Tomita, and Yoshisuke Hamamoto. "Fundamental study on combustion diagnostics using a spark plug as ion probe." *SAE transactions* 109.3 (2000): 1990-2002.

[44] Gazis, Andreas, et al. "Computationally inexpensive methods of ion current signal manipulation for predicting the characteristics of engine in-cylinder pressure." *International Journal of Engine Research* 7.3 (2006): 271-282.

[45] Danne, Nicholas M., et al. "Knock Detection for a Large Displacement Air-Cooled V-Twin Motorcycle Engine Using In-Cylinder Ionization Signals."*Training* 2014: 03-24.

[46] Zhu, G., Hung, D., and Winkelman, J., “Combustion Characteristics Detection for Low Pressure Direct Injection Engine Using Ionization Signal," SAE Technical Paper 2006-01-3317, 2006, doi:10.4271/2006-01-3317.

[47] Labuda, S., et al. "APPLICATION OF IONIZATION PROBES FOR DIAGNOSTICS OF KNOCKING COMBUSTION." *Chia Laguna, Cagliari, Sardinia, Italy, September 11-15, 2011*.

[48] Guoming G. Zhu, Chao F. Daniels and Jim Winkelman, "MBT Timing Detection and its Closedloop Control Using In-Cylinder Ionization Signal," SAE 2004-01-2976.

[49] Naber, Jeffrey D., et al. "Analysis of combustion knock metrics in spark-ignition engines." *SAE Paper No. 2006-01* 400 (2006).

[50] Guillemin, Fabrice, et al. "Combustion parameters estimation based on knock sensor for control purpose using dedicated signal processing platform." *Fuel* 2013 (2008): 08-08.

[51] Arnone, L., Manelli, S., Chiatti, G., and Chiavola, O., "In-Cylinder Pressure Analysis through Accelerometer Signal Processing for Diesel Engien Combustion Optimization," SAE Technical Paper 2009-01-2079, 2009, doi:10.4271/2009-01-2079.

[52] Chiavola, O., Chiatti, G., and Recco, E., "Accelerometer Measurements to Optimize the Injection Strategy," SAE Technical Paper 2012-01-1341, 2012, doi:10.4271/2012-01-1341.

[53] Taglialatela, F., Cesario, N., Porto, M., Merola, S. et al., "Use of Accelerometers for Spark Advance Control of SI Engine," *SAE Int. J. Engine* 2(1):971-981, 2009, doi:10.4271/2009-01-1019.

[54] Polonowski, Christopher J., Vivek K. Mather, and Jeffrey D. Naer. "Accelerometer based sensing of combustion in a high speed HPCR diesel engine." *SAE Paper* (2007): 01-0972.

[55] Polonowski, Christopher. Accelerometer based Measurements of Combustion in an Automotive Turbocharged Diesel Engine [PhD Dissertation]. Houghton (MI). Michigan Technological University. 2009.

[56] Gao, Y., and R. B. Randall. "Reconstruction of diesel engine cylinder pressure using a time domain smoothing technique." *Mechanical systems and signal processing* 13.5 (1999): 709-722.

[57] Morello, Andrew J., et al. "Signal Processing Parameters for Estimation of the Diesel Engine Combustion Signature." *SAE International Journal of Passenger Cars-Mechanical Systems* 4.2 (2011): 1201-1215.

[58] Morello, Andrew J., Remote Combustion Sensing of a 9-Liter Diesel [Master Dissertation]. Houghton (MI). Michigan Technological University. 2011.

[59] El-Ghamry, M., et al. "Indirect measurement of cylinder pressure from diesel engines using acoustic emission." *Mechanical systems and signal processing*19.4 (2005): 751-765.

[60] J.T.KIM (1987). Source and path recovery from vibration response monitoring. *PhD Dissertation.* Massachusetts Institute of Technology, USA.

[61] Kim, Jeung T., and Richard H. Lyon. "Cepstral analysis as a tool for robust processing, deverberation and detection of transients." *Mechanical systems and signal processing* 6.1 (1992): 1-15.

[62] Villarino, Ruben, and J. E. Bohme. "Fast in-cylinder pressure reconstruction from structure-borne sound using the EM algorithm." *Acoustics, Speech, and Signal Processing, 2003. Proceedings.(ICASSP'03). 2003 IEEE International Conference on*. Vol. 6. IEEE, 2003.

[63] Wagner, M., Böhme, J., and Förster, J., “In-cylinder Pressure Estimation from Structure-Borne Sound," SAE Technical Paper 2000-01-0930, 2000, doi:10.4271/2000-01-0930.

[64] Villarino, Ruben, and Johann F. Bohme. "Pressure reconstruction and misfire detection from multichannel structure-borne sound." *Acoustics, Speech, and Signal Processing, 2004. Proceedings.(ICASSP'04). IEEE International Conference on*. Vol. 2. IEEE, 2004.

[65] Villarino, Ruben, and Johann F. Böhme. "Pressure reconstruction and misfire detection from multichannel structure-borne sound." *Acoustics, Speech, and Signal Processing, 2004. Proceedings.(ICASSP'04). IEEE International Conference on*. Vol. 2. IEEE, 2004.

[66] Villarino, Ruben, and Johann F. Böhme. "Misfire detection in spark-ignition engines with the EM algorithm." *Signal Processing and Information Technology, 2003. ISSPIT 2003. Proceedings of the 3rd IEEE International Symposium on*. IEEE, 2003.

[67] Bizon, Katarzyna, et al. "Reconstruction of In-Cylinder Pressure in a Diesel Engine From Vibration Signal Using a RBF Neural Network Model." *Diesel Engine* 2010 (2011): 10-01.

[68] Johnsson, Roger. "Cylinder pressure reconstruction based on complex radial basis function networks from vibration and speed signals." *Mechanical Systems and Signal Processing* 20.8 (2006): 1923-1940.

[69] Desantes, Jose M., and Antonio J. Torregrosa. "Wavelet transform applied to combustion noise analysis in high-speed DI diesel engines." SAE Technical Paper 2001-01-1545, 2001, doi:10.4271/2001-01-1545.

[70] Sen, Asok K., et al. "Wavelet analysis of cycle-to-cycle pressure variations in an internal combustion engine." *Chaos, Solitons & Fractals* 38.3 (2008): 886-893.

[71] Kim, Seonguk, and Kyoungdoug Min. "Detection of combustion start in the controlled auto ignition engine by wavelet transform of the engine block vibration signal." *Measurement Science and Technology* 19.8 (2008): 085407.

[72] Hariyanto, A., Bagiasna, K., Asharimurti, I., Wijaya, A. et al., "Application of Wavelet Analysis to Determine the Start of Combustion of Diesel Engines," SAE Technical Paper 2007-01-3556, 2007, doi:10.4271/2007-01-3556.

[73] Borg, J., Saikalis, G., Oho, S., and Cheok, K., "Knock Signal Analysis Using the Discrete Wavelet Transform," SAE Technical Paper 2006-01-0226, 2006, doi:10.4271/2006-01-0226.

[74] Jung, I., Jin, J., So, H., Nam, C. et al., "An Advanced Method for Developing Combustion Noise through the Analysis of Diesel Combustion," *SAE Int. J. Engines* 6(2):1379-1385, 2013, doi:10.4271/2013-01-1901.

[75] Tousignant, T., Wellmann, T., Govindswamy, K., Heuer, S. et al., "Application of Combustion Sound Level (CSL) Analysis for Powertrain," SAE Technical Paper 2009-01-2168, 2009, doi:10.4271/2009-01-2168.

[76] Montgomery, D. and Reitz, R., "Effects of Multiple Injections and Flexible Control of Boost and EGR on Emissions and Fuel Consumption of a Heavy-Duty Diesel Engine," SAE Technical Paper 2001-01-0195, 2001, doi:10.4271/2001-01-0195.

[77] Lee, S., Gonzalez D., M., and Reitz, R., "Effects of Engine Operating Parameters on near Stoichiometric Diesel Combustion Characteristics," SAE Technical Paper 2007-01-0121, 2007.

[78] Y. Shi, R. C. Eberhart, Empirical Study of Particle Swarm Optimization, Proceedings of the 1999 Congress on Evolutionary Computation, pp. 1945-1950, Piscataway, 1999.

[79] X. Hu and R C. Eberhart, “Multiobjective optimization using dynamic neighborhood particle swarm optimization”, Proceedings of the IEEE Congress on Evolutionary Computation, Honolulu, Hawaii, USA. pp. 1677-1681, 2002.

[80] Marc Landry, Azeddine Kaddouri, Yassine Bouslimani, and Mohsen Ghribi, "Application of particle swarm optimization technique for an optical fiber alignment system", International Journal of Electronics and Electrical Engineering, 6, 2012.

[81] S. Selleri, M. Mussetta, P. Pirinoli, R. E. Zich, and L. Matekovits,“Some insight over new variations of the particle swarm optimization method,” IEEE Antennas Wireless Propag. Lett., vol. 5, pp. 235–238.

[82] Fassios, S. MIMO LMS-ARMAX indentification of vibrating structures-part 1: the method. *Mechanical systems and signal processing* (2001); 15(4): 723-735.

[83] Klerk, D. and Ossipov, A. Operational transfer path analysis: theory, guidelines and tire noise application. *Mechanical systems and signal processing* 24 (2010); 1950-1962.

[84] Abdi, H. and Williams, L. Princinpal component analysis, *WIREs computational statistics*; volume2, July/August 2010.

[85] O’Toole AJ, Abdi H, Deffenbacher KA and Valentin D. A low dimensional representation of faces in the higher dimensions of the space. *J Opt Soc Am [Ser A]* 1993; 10:405–411.

[86] Demuth, H., Beale, M., Neural Network Toolbox, user’s guide, version 4, The Mathworks.

[87] Chen, Sheng, C. F. N. Cowan, and P. M. Grant. "Orthogonal least squares learning algorithm for radial basis function networks." *Neural Networks, IEEE Transactions on* 2.2 (1991): 302-309.

[88] Mao, K.Z., Huang, G, 2005, “Neuron Selection for RBF Neural Network Classifier Based on Data Structure Preserving Criterion,” Volume: 16, Issue: 6, Neural Networks.

[89] Bosch, 1999, “Diesel-engine management,” SAE society of international of engineers, Robert Bosch GmbH, Postfach (2nd edition).

[90] Wu, Z. and Chen, L., 2008, “Method to efficiently implement automotive application algorithms using signal processing engine (SPE) of copperhead microcontroller,” SAE Technical Paper 2008-01-1222.

[91] AVL 450 Combustion Noise Meter Instruction Manual, August, 2000.

[92] Russell M F, “Automotive Diesel engine noise and its control,” *SAE Paper* 730243.

[93] B. P. Bogert, M. J. R. Healy, and J. W. Tukey: "The Quefrency Alanysis of Time Series for Echoes: Cepstrum, Pseudo Autocovariance, Cross-Cepstrum and Saphe Cracking". *Proceedings of the Symposium on Time Series Analysis* (M. Rosenblatt, Ed) Chapter 15, 209-243. New York: Wiley, 1963.

Appendix

Letters of permission

Permission for Figure 2.2

Order Completed

Thank you very much for your order.

This is a License Agreement between Libin Jia ("You") and Elsevier ("Elsevier"). The license consists of your order details, the terms and conditions provided by Elsevier, and the payment terms and conditions.

Get the printable license.

License Number	3327690989178
License date	Feb 14, 2014
Licensed content publisher	Elsevier
Licensed content publication	Mechanical Systems and Signal Processing
Licensed content title	Cylinder pressure reconstruction based on complex radial basis function networks from vibration and speed signals
Licensed content author	Roger Johnsson
Licensed content date	November 2006
Licensed content volume number	20
Licensed content issue number	8
Number of pages	18
Type of Use	reuse in a thesis/dissertation
Portion	figures/tables/illustrations
Number of figures/tables/illustrations	1
Format	both print and electronic
Are you the author of this Elsevier article?	No
Will you be translating?	No
Title of your thesis/dissertation	MODELING OF THE TRANSFER PATH BETWEEN THE DIESEL ENGINE COMBUSTION METRICS AND THE ENGINE VIBRATION AND NOISE

Expected completion date	Apr 2014
Estimated size (number of pages)	1
Elsevier VAT number	GB 494 6272 12
Permissions price	0.00 USD
VAT/Local Sales Tax	0.00 USD / 0.00 GBP
Total	0.00 USD

ORDER MORE... CLOSE WINDOW

Permission for Chapter 5

Beth Darchi <DarchiB@asme.org> Fri, Feb 14, 2014 at 2:14 PM

To: Libin Jia <libinj@mtu.edu>

Cc: AccountsReceivable <AccountsReceivable@asme.org>

Dear Mr. Jia,

It is our pleasure to grant you permission to publish the following ASME materials:

· Accelerometer-Based Combustion Metrics Reconstruction With Radial Basis Function Neural Network for a 9□L Diesel Engine," by Libin Jia; Jeffrey Naber;

Jason Blough; Seyed Alireza Zekavat , Journal of Engineering for Gas Turbines and Power, Volume 136(3) 2013

As author, ASME has waived any fees for the paper Accelerometer-Based Combustion Metrics Reconstruction with Radial Basis Function Neural Network for a 9□L Diesel Engine.

Many thanks for your interest in ASME publications.

Sincerely,

Beth Darchi

Publishing Administrator

ASME

2 Park Avenue, 6th Floor

New York, NY 10016-5990

Tel 1.212.591.7700

darchib@asme.org

Permission for Figure 2.3

May I have your permission for this figure?

Libin Jia <libinj@mtu.edu> Fri, Feb 14, 2014 at 10:55 AM

To: permissions@iop.org

To whom it may concern,

May I use the Figure 3 of "Kim, Seonguk, and Kyoungdoug Min. "Detection of combustion start in the controlled auto ignition engine by wavelet transform of the engine block vibration signal." Measurement Science and Technology 19.8 (2008): 085407." in my phd dissertation?

Thanks!

Libin

Permissions <permissions@iop.org> Mon, Feb 17, 2014 at 3:20 AM

To: Libin Jia <libinj@mtu.edu>

Dear Libin Jia,

Thank you for your request to reproduce IOP Publishing material.

We are happy to grant permission for the use you request on the terms set out below.

If you have any questions, please feel free to contact our Permissions team at permissions@iop.org.

I should be grateful if you would acknowledge receipt of this email.

Kind regards,

Sarah Ryder

Publishing Administrator

Email: permissions@iop.org